The Non-linear Quantum Dynamics of Superconducting Circuitry

Grace Frances Morley, MSci

Thesis submitted to the University of Nottingham for the degree of

Doctor of Philosophy

May 18, 2023

These then are some illustrations of things that are happening in modern times - the transistor, the laser, and now these junctions, whose ultimate practical applications are still not known. The quantum mechanics which was discovered in 1926 has had nearly 40 years of development, and rather suddenly it has begun to be exploited in many practical and real ways. We are really getting control of nature on a very delicate and beautiful level.

-Richard Feynman on the Josephson junction, The Feynman Lectures On Physics Vol III, 1963

Acknowledgements

Firstly, I would like to thank my supervisor Andrew Armour, whose patient guidance, direction, and unending support were key to allowing me to complete this work. It would also be remiss of me to not acknowledge the help of Ben Lang, whose ideas and counsel helped form a lot of the second half of this thesis.

I would also like to thank all my friends from C18 and C20 and in particular Matt, Maike, Gary, Ciaran, Neil, Jemma, Dom, Chris, and Joe for their endless encouragement, patience, and supply of mediocre coffee. Additionally, I would like to extend my gratitude to all the anonymous members of the Nottingham Nightline Association and in particular the members of the executive committee, without whom I suspect my life would look very different right now.

Many thanks need to be extended to my family for their love, support, and for listening to my deranged rants even when they didn't understand. Finally, I would like to extend special thanks to my friend Ellie Frampton. I doubt I this thesis could have been written in such trying times without her help.

Abstract

Over the last few decades, it has been established that the Josephson junction's (JJ) non-linear nature can be used to manufacture novel quantum Hamiltonians. The uneven spacing in the energy levels of circuits containing one or more Josephson junctions means that they can be thought of as forming something like an atom. These artificial atoms, when connected to one or more quantum harmonic oscillators formed by microwave cavities, can then be used to study the interaction of light and matter in a new field called circuit quantum electrodynamics (cQED).

A subset of these systems, which combine a voltage biased Josephson junction in series with a cavity, bring together charge dynamics with microwave photonics in an interesting way. In these devices, Cooper pairs can tunnel through the circuity only when the energy supplied by the voltage matches that of a transition within the microwave cavity. When this condition is met, the Cooper pair tunnelling evolves from incoherent to coherent tunnelling as the Josephson energy of the junction is increased.

In this thesis, we will explore the dynamics of a JJ-cavity system voltage biased such that each Cooper pair has energy equal to half that of the transition in one of the cavity modes, this being the simplest possible case of super harmonic driving. We find that the presence of the cavity mode promotes tunnelling of the Cooper pairs at the same time. We use a second order rotating wave approximation to derive an effective time-independent Hamiltonian that describes this behaviour and we use it to explore how the state of the cavity mode evolves as the Josephson energy of the junction is increased. We also explore the way in which charge is transported through the system, identifying regimes of both incoherent and coherent double Cooper pair tunnelling.

This thesis will also examine the dynamics of a Josephson junction cavity system where more then one mode can play an important role, know as the Josephson laser. We will start by examining

the behaviour of a system with a very large number of modes. We find that in this case the system exhibits a wide range of dynamical behaviour as a function of the strength of the applied drive. Surprisingly it can take an extremely long time for the system to reach a stable regime (beyond any transient behaviour). We also explore the behaviour in cases where a relatively small number of modes are included. Here the pattern is less complex, but still very interesting. We show how this system undergoes a discrete time symmetry breaking transition as the drive strength increases, and how this transition can occur in two different ways, continuous and discontinuous. We prove that the conditions that determine if the transition will be continuous or discontinuous are related to the destabilization of the zero amplitude solution, which in turn is dependent on the relationship between the number of modes present and the voltage.

Contents

Chapter 1

Introduction

The Josephson junction (JJ) as we know it today was first described by Brian Josephson back in the 1960s[1–3]. The unique physics of the superconducting device he described was found to generate strongly nonlinear behaviour within both classically and quantum mechanically described circuits. This has naturally led to a verity of novel quantum devices being engineered to exploit this behaviour[4]. A key element of this is the presence of energy levels within the circuits containing JJ's with non-equal spacings[5, 6], analogous to the energy levels of atoms. The JJ based super-conducting circuit is of interest for many areas of research including physics as analogues for other systems[7], as sensitive magnetometers for precision sensing[8, 9], and as a promising candidate for qubits in quantum processors[10–13].

One of the circuits that utilized the JJ is that of the voltage biased JJ-cavity superconducting circuit in which a dc voltage bias is applied across a series combination of a Josephson junction and a microwave cavity which can be thought of as a set of harmonic oscillators[14–20]. In this case, the Cooper pairs tunnelling through the junction can directly produce photons in the cavity and the photons can directly influence the state of the junction if they are present. This behaviour is analogous to that of absorption and emission of an atom interacting with light and is thus a form of circuit based quantum electrodynamics[21, 22] (cQED).

The voltage biased JJ-cavity system will play a central role in this thesis. Studies of this system first began in the mid 1990s with cavity systems constructed with weak drive and strong loss, such that the photons produced in the cavity had little or no effect on the Cooper pairs tunnelling

through the junction[14, 23–26]. However, in the last few years work on such systems has mainly focused on the regime of strong drive and weak loss where the presence of photons within the cavity can influence the dynamics of the system significantly[7, 27–29].

Studies of the JJ-cavity system have principally focused on the cases where the circuits exhibit subharmonic resonances, where one Cooper pair tunnels and produces one or more photons in the cavity[27, 29, 30], however very little work has been presented on the superharmonic case where two Cooper pairs together create a single photon. Additionally, experiments on Josephson junction based 'lasers' have probed regimes where excitation of the fundamental cavity mode is mediated by other modes, leading to results[31] which are only partially understood[32]. It is these two gaps in the research literature that we wish to address in this thesis.

In this thesis, new research concerning two different areas will therefore be presented. The first area involves constructing a theoretical framework to describe a voltage biased JJ-cavity system when tuned such that multiple Cooper pairs tunnel to create a single photon (super harmonic resonance)[33]. We will establish that the techniques used extensively in work on the subharmonic resonance cases, namely the Rotating Wave Approximation, cannot be applied to this system without substantial alteration. Instead, we use a more sophisticated second order rotating wave approximation to define a time independent effective Hamiltonian which can be used to describe the resonance. We will show that as the strength of the Josephson energy associated with the junction is increased, the system moves from a regime dominated by incoherent tunnelling of pairs of Cooper pairs, to one dominated by coherent tunnelling of pairs of Cooper pairs and photons with a sub-Poissonian (anti-bunched) distribution. Lastly we shall prove that, when the junction is driven such that two Cooper pairs generate a single photon, the cavity can become locked within just two energy levels of the system, thus blocking any chance of simultaneous photon production. This occurs in a parameter range significantly easier to access than other, similar, systems and within experimental capabilities.

The second half of the thesis will focus on expanding research on the recent theory of the Josephson junction laser developed by Simon and Cooper[32]. We will demonstrate that when the JJ couples to a very large number of modes within the cavity, it can demonstrate a number of different behaviours depending on the relative drive strength. These behaviours will be explored in detail. We also examine the threshold dynamics of a JJ laser system with access to only a few

modes within the cavity[34]. We show that these systems can undergo a discrete time translational symmetry breaking transition as the drive strength is increased. We shall show that this can accrue in two different ways, discontinuous and continuous, and appears to occur collectively across all the modes of the cavity. Finally, we explore the effect of moving to voltages that are no longer commensurate with the fundamental mode of the cavity, showing that in this case only a discontinuous discrete time symmetry breaking event occurs.

While these topics may appear to be somewhat disconnected, in actuality both represent complex dynamics that can arise from interesting resonances. Also, while this system has been studied extensively experimentally in the past there has recently been renewed interest in the area thanks in particular to the work done by groups in Paris[14, 35, 36] and Delft[31]. This work has lead to a need to re-examine and develop the underlying theory. The analysis in this thesis explores issues that have not been examined before[33, 34] and will hopefully prove relevant to ongoing work in the area.

1.1 Outline of the Thesis

In the following, we outline the contents of the thesis. Chapter 2 introduces the topic of superconducting circuits and their use as tools for the exploration of Quantum Electrodynamics through the field of cQED. It then moves on to discuss the key superconducting component that will be the main focus of the thesis, the Josephson junction, and the theory behind coupling a Josephson junction to a cavity. We then review the recent theoretical work on voltage biased JJ-cavity systems to provide context for the original research presented in the later chapters.

Chapter 3 describes original research explaining the behaviour of a JJ-cavity system in which a single mode is relevant. We consider a superharmonic resonance where two tunnelling Cooper pairs can generate one photon. We explore the behaviour of the system as the Josephson energy of the junction is tuned using a range of numerical and analytic techniques. We find that the dynamics of both the cavity mode and the charges (the Cooper pairs tunnelling though the circuit) exhibit several fascinating regimes of behaviour, including coherent and incoherent double Cooper pair tunnelling. We also describe why and how the system can act as a single photon source.

In chapter 4 we move on to analyse the theory behind the Josephson laser, specifically the dynamics in the limit where the laser incorporates many modes. We will begin by approximating

the system's dynamics in the low drive strength limit using perturbative methods, and show that the laser should tend to a sawtooth wave solution in this regime. We will then begin to detail the different regimes that the system goes through as the drive strength in the system is increased. We find that the dynamics always eventually results in the laser oscillating in a sawtooth wave with a period matching that of the voltage drive.

In chapter 5 we continue with the theory of the Josephson laser by examining its dynamics when only a few cavity modes are incorporated. We found that the system is predicted to undergo a discrete time symmetry breaking transition as the drive strength is increased. We show that this transition can occur in two ways, discontinuous and continuous, with the type dependent on the number of modes available. We demonstrate that this arises from fixed points destabilizing in different ways and show this analytically using a combination of RWA based analytical calculations and careful numerical calculations. The chapter also includes an exploration of the effect of different damping rate for specific modes, as well as the behaviour when the voltage drive is far from being an integer multiple of the fundamental mode frequency.

Lastly, in chapter 6 we will bring the different strands of the work together and discuss the commonalities between the two systems and draw conclusions about the wider implications this work has for the future study of JJ-cavity systems.

The work presented on the theory of double Cooper pair tunnelling in chapter 3 is based on original research undertaken in collaboration with researchers at the University of Konstanz and Prof Andrew Armour, published in [33]. The results on the Josephson junction laser presented in chapter 4 and 5 is also original research undertaken in collaboration with Prof Andrew Armour and Dr Ben Lang, these results have been published[34].

Chapter 2

Background Theory

2.1   Introduction

Before we can detail the new research that will be presented later on in this thesis, we must first establish a theoretical background that can be built upon. The purpose of this chapter is to review the key physics relating to superconductivity and superconducting circuits which is important for understanding the new results presented in later chapters.

We will begin by covering the background of superconducting quantum circuits, and quantum physics of superconductivity in general. We will then move on to discuss the physics of Josephson junctions, their construction and the nonlinear behaviour that they give rise to. We will discuss why this nonlinear behaviour means that these junctions can act as artificial atoms and are perfect for studying how light interacts with matter. The AC Josephson effect and its mathematics will be a key part of this discussion.

We will then move on to describe the development of voltage biased Josephson junction cavity systems, which will form the main focus of later chapters. We will explore the history of these circuits: from the original approach of only describing their dynamics in weak driving regimes, to the experiments that revolutionized the understanding of charge flow through the junction.

We will then discuss the inception of the coherent tunnelling description of Josephson junction cavity systems, and the need to analyse the far from equilibrium dynamics. We will include discussions of the Hamiltonian of the system and under what circumstances it can be simplified

using a simple Rotating Wave Approximation. We will also discuss the potential applications of these systems, including but not limited to their use in producing highly non-classical light states in an on-chip device. Lastly we will go into detail about how a Josephson junction cavity system can display laser-like behaviour, we will detail the two main papers that describe the experimental results and the theory that followed it.

This chapter will be broken down into the following sections. In section 2.2 we will detail the history of superconducting circuits and the voltage biased Josephson junction. In section 2.3 we will introduce voltage biased Josephson junction systems and inelastic Cooper pair tunnelling. In section 2.4 and section 2.5 we will present research on Josephson Junction cavity systems on which the thesis will be building directly, including the far from equilibrium dynamics of a Josephson junction cavity system and the Josephson junction laser.

2.2   Superconducting circuits

In a classical circuit the charge carriers, electrons, move through the conductor randomly but with a slight bias in one direction if an electric field present, such as when the circuit is connected to a voltage source[37, 38]. This movement is impeded by lattice vibrations and impurities in the metallic crystal, causing energy to be lost from the electrons. This is the macroscopic description of resistance in circuitry and implies that for a current to constantly pass through the circuit, the voltage must remain in place to replace the energy lost in interactions with the lattice. This is not the only possibility though, as many metals are cooled, they undergo a phase transition and become superconductors.

When metals undergo the phase transition to become superconductors, the electrons form pairs, known as Cooper pairs, bound to together by phonons[39, 40]. The Cooper pairs can move through the superconductor unimpeded by the crystal structure, meaning that the superconductor acts as a perfect conductor with no resistance. Because of this zero resistance state, an indefinite current can flow through the conductor even if the voltage is removed, as the Cooper pairs don't lose energy to interactions with the lattice.

Another consequence of the Cooper pairs forming is that the charge carriers in the material go from being Fermions to being composite Bosons, with integer (normally zero) spin. Because the charge carriers are composite Bosons they are able to occupy the same quantum state simultaneously

and the vast majority of the Cooper pairs will occupy the lowest possible energy state. Because of this, while it is possible to describe the wavefunction of each Cooper pair individually, it is much more practical to simply write the collective wavefunction of all the Cooper pairs which has form,

$$\Psi(r) = \sqrt{n(r)}e^{-i\phi(r)} \tag{2.1}$$

where $n(r)$ is the Cooper pair density at the position r and $\phi(r)$ is the phase of the superconductor as position r[40].

These Cooper pairs are weakly bonded, their binding energy is denoted by pair as $|2\Delta|$, and can be broken apart if too much energy is inputted in to the system for example from thermal fluctuations in the surrounding circuit. This means there are maximum thresholds at which the superconducting behaviour can be sustained, these are known as the critical temperature, T_c, and the critical current, I_c. If the superconducter exceeds either of these thresholds, it will undergo a phase transition back to a normal conducting state with all the Cooper pairs split up.

The ability to utilise electrical components with no electrical resistance, albeit at low temperatures $T < T_c$, leads to some interesting opportunities when it comes to engineering novel quantum systems. For example, consider a simple inductor-capacitor (LC) oscillator in a non-superconducting circuit. Because these components have some intrinsic resistance within them, the system actually forms an inductor-capacitor-resister (LCR) oscillator which is analogous to a damped harmonic oscillator[37]. Thus, if an LCR oscillator is given a voltage impulse, the resulting current dynamics would exhibit an oscillation which decays over time as energy is gradually lost to the environment. In contrast, if these circuits are constructed using a superconducting material, the lack of resistance would cause the current to oscillate indefinitely with no loss. From a Quantum Mechanical point of view, this means an LC oscillator constructed using superconducting material can act as a quantum harmonic oscillator[41], apparently protected from decoherence due to internal resistance, i.e. it would be a perfectly coherent quantum harmonic oscillator.

Another key superconducting circuit element is the Josephson junction (JJ). A Josephson junction consists of two superconducting electrodes separated by some kind of barrier, either a section of non-superconducting metal or an insulating oxide normally. In a JJ, the only way for a current to flow is for the Cooper pairs to tunnel through the junction via the overlapping/hybridizing superconducting wavefunctions on either side of the junction[4]. In the mid 1960s Brian Josephson[1]

was the first to study these systems theoretically and discovered that the current generated by tunnelling across the junction was directly proportional to the sine of the difference in superconducting phase across the junction, φ.

While the existence of macroscopic quantum states such as the collective one found in superconductors was not particularly controversial, the idea that these states could exist within a superposition of different superconducting phases was[42]. This idea was first proposed by Windom[21] in 1979 and then expanded upon by Leggett[43, 44], who suggested that not only these superpositions exist, but they should be experimentally observable within a laboratory. This was controversial at the time, as it was thought that any such superposition within a macroscopic state would quickly undergo decoherence due to interactions with the thermal environment.

The first experiment that suggested that these superpositions were indeed observable was performed by the Clark group[45], however their results were not conclusive on the matter. While many other experiments would also observe similar phenomena[46–48] the matter wasn't conclusively proven until 1999 when Nakamura et al.[49] observed the superposition of quantum macroscopic states.

Modern derivations of the nonlinear Hamiltonians that arise for superconducting quantum circuits are largely based on the work by Devoret[50] whose work was a generalisation of the work performed by Yurke and Denker[51].

Because of this highly nonlinear nature, a great deal of effort has been put into using Josephson junctions to engineer systems with novel Hamiltonians and energy level structures[4]. For example, a single junction with access to many Cooper pairs, subject to a current bias, will exhibit a tilted 'washboard' potential. This is often known as a phase qubit[4]. Other novel systems such as the flux qubit[52] and the Cooper pair box (charge qubit)[53] can also be constructed with unusual energy potentials and have been the been studied extensively.

One key advantage of this nonlinear nature is the fact that in all of these systems, the energy levels produced by these novel Hamiltonians have unequal spacing. This means that Josephson junction circuits can act as an analogous system to an atom[5, 6]. These 'artificial atoms' have several advantages over their natural counterparts. Notably, they can be made to strongly interact with the atom's environment, in contrast with natural atoms which tend to only interact weakly. Additionally, the properties of the Josephson junction depend on the specifics of its construction.

Because of this, artificial atoms can be engineered to have any number of different properties, as well as being tuneable after the fact by using external factors. For example, the properties of a flux qubit can be altered after construction by the application of a magnetic field to the centre of the superconducting loop[54].

Because of the unequal nature of the energy level spacings of circuits containing JJs, systems can be manufactured and exited in such a way that only some energy levels are ever excited. Most importantly, if the system is driven by energies that match the $|0\rangle \rightarrow |1\rangle$ transition, no other transition will be resonantly driven. When $|0\rangle$ and $|1\rangle$ are also the two lowest energy levels, this means that the system will be locked to these two energy levels only and effectively becomes a two level system, i.e. a qubit, that can be directly fabricated on chip[5]. This has been explored extensively in the field of quantum computing, as Josephson junctions make for a very appealing candidate for the qubits used in a quantum processor. Recent developments have yielded quantum computers in the ranges of tens of qubits[55], and work continues on problems such as controlling the interactions they have with the environment to minimize qubit decoherence.

The fact that superconducting circuits can act as artificial atoms also lends itself to the study of how atoms interface with light. This is done by constructing a Josephson junction connected to a microwave resonator, which acts as a coherent quantum harmonic oscillator[56]. This allows for controlled, tuneable, interactions between the light present in the cavity and the artificial atom. This new form of Quantum Electrodynamics, known as circuit Quantum Electrodynamics (cQED)[21, 22], can be used to study a range of phenomena including the ultra-strong coupling regime and the between light and matter[57, 58].

2.3 Josephson Photonics and Inelastic Cooper Pair Tunnelling

2.3.1 AC Josephson effect

When a Josephson junction is placed in a circuit, the voltage across and current flowing through it are governed by the Josephson phase, $\varphi = \phi_A - \phi_B$, which is the difference between the superconducting wavefunction phase in the first, ϕ_A, and the second electrode, ϕ_B. The current relation is

given by,

$$I = I_c \sin(\varphi) \tag{2.2}$$

where I_c is the critical current. The voltage relationship is given as,

$$\frac{\partial \varphi}{\partial t} = \frac{2\pi}{\Phi_0} V(t), \tag{2.3}$$

where $\Phi_0 = \frac{2\pi\hbar}{2e}$ is the magnetic flux quantum[1, 4].

In the case of fixed voltage, $V(t) = V$, equation (2.3) becomes a simple integration leading to constantly, linearly increasing, Josephson phase, $\varphi \propto Vt$. It is a logical follow on from this that the current through the junction is just a sinusoid, oscillating from I_c to $-I_c$ and back. Thus, there is no net current flow throughout the circuit and no net energy change. This is known as the AC Josephson effect.

The key to allowing current to follow through the junction while maintaining the constant voltage is to allow for energy exchange between the tunnelling Cooper pair and some external component, allowing the Cooper pair to convert its excess energy to another form so that it can integrate into the wavefuntion of the second electrode and flow away. A common way of facilitating this energy exchange is to allow the junction to interact with a microwave frequency cavity[56, 59]. When this is done, the excess energy of the Cooper pairs can be converted into photons. For a current to flow at a given voltage V the energy of the Cooper pair $2eV$ needs to match the energy of one of the modes present in the cavity, $\hbar\omega_i$, this constraint is known as a resonance condition and must be satisfied in some way for a current to flow[1]. For Cooper pairs that have undergone this type of inelastic tunnelling, it is then highly unlikely for them to re-tunnel through the junction as this would require the absorption of a photon to overcome the energy barrier.

An example circuit that is capable of showing this behaviour is shown in Fig 2.1. A Josephson junction, represented by a square box with a diagonal cross, is placed in series with a microwave cavity. The modes of this cavity each act as independent quantum harmonic oscillators which are modelled as a string of LC oscillators all in series. Each of the oscillators has frequency $\omega_n = 1/\sqrt{L_n C_n}$, and thus the separation of their energy levels is $E_n = \hbar\omega_n$. In the example given

---

[1] While matching the energy of a single Cooper pair to a single mode is the simplest possible case, in reality we can meet this condition by matching this energy to a combination of modes, thus having a combination of photons produced by one Cooper pair [27, 28, 30, 60], or multiple Cooper pairs produce one photon which will be explored in chapter 3 of this thesis.
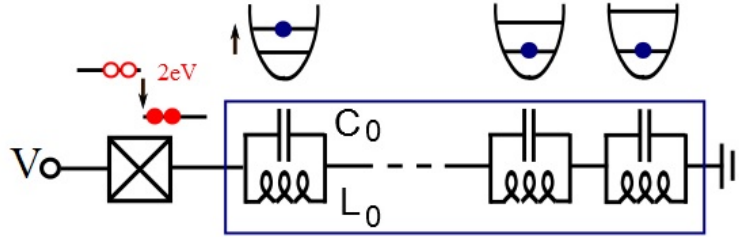
Figure 2.1: The circuit diagram of a voltage biased Josephson junction in series with a cavity with multiple modes, modelled as a string of LC oscillators. The presence of the oscillators allows for a current to flow as long as the energies of the Cooper pairs, $2eV$, matches the energy of one of the oscillator, i.e. $2eV = \hbar\omega_n$. The example energy exchange where is $2eV = \hbar\omega_0$ is shown above.

in Fig 2.1, a net current could only flow if the voltage bias across the junction was set such that $2eV = E_n$ where E_n is the energy of any one of the oscillators.

While the Josephson effect relations are able to describe the dynamics of the system when Cooper pairs can only tunnel back and forth, the inclusion of a cavity requires us to begin thinking past the basic theory proposed by Josephson. We need a theory that can describe the non-equilibrium dynamics that arise when energy is allowed to leave the system, for this we turn to $P(E)$ theory, and the theory of open quantum systems.

2.3.2 Early experiments and Perturbation Theory

An early experiment which revealed important new aspects of the behaviour of a voltage biased Josephson junction connected to a microwave cavity was performed by Holst et al. in 1994[23]. They constructed an ultra-small tunnel junction embedded in a coplanar wave guide that acts as a microwave resonator. A voltage was then placed across the junction and the tunnel current through the junction was measured as this voltage was varied. The main results are shown in Fig 2.2. They observed spikes in the tunnel current through the junction when the energy of the tunnelling Cooper pairs matched that of the modes present within the cavity, implying that when these energies matched, Cooper pairs could shed their extra energy in the form of photons and then tunnel through the junction and allow a current to flow.

In many of these early experiments[24], including that of Holst et al.[23], a key factor was a relatively low quality factor, Q^2. This, along with a weak strength of interaction between the

_____

[2]In this case a relatively low Q was usually defined as $\ll 100$[14], the key aspect was that the cavity was almost
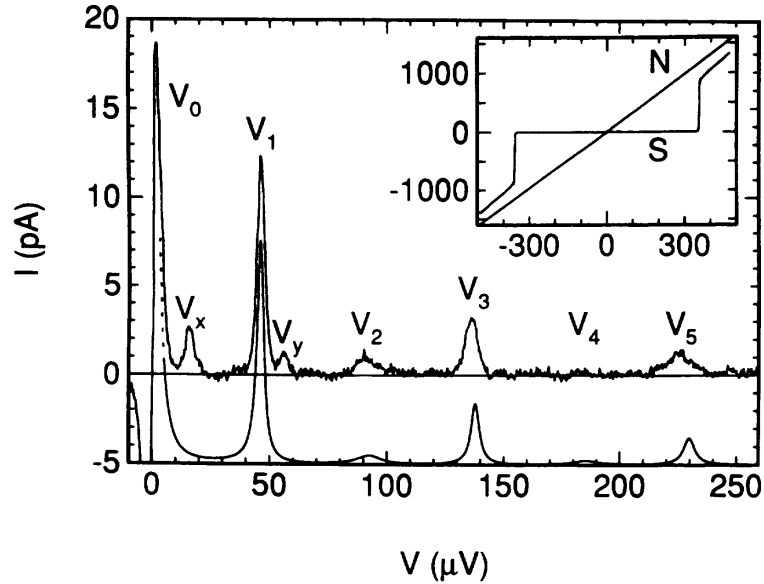
Figure 2.2: The current passing though the tunnel junction at $22mK$ with the theoretical prediction (smooth continuous line) offset by $5pA$. The theory predicts a series of current resonances (peaks) based on matching between the voltage and harmonic modes in the cavity. In fact more modes exist than were expected, leading to extra peaks in the data. Inset: the large scale current dynamics in both the superconducting, S, and normal, N, regimes. Reprinted Figure 2 with permission from T. Holst, D. Esteve, C. Urbina, and M. H. Devoret, Effect of a Transmission Line Resonator on a Small Capacitance Tunnel Junction [23], Copyright 2021, the American Physical Society.

junction and the cavity governed by the Josephson energy, E_J, ensured that the rate that photons leave theQ cavity, $1/Q$, is much larger than the tunnel rate at which the photons are generated, which is equal to the rate at which Cooper pairs pass through the junction, Γ_{CP}. This ensures that the cavity is effectively at thermal equilibrium with an average occupation $\ll 1$. Since the photons generated by Cooper pair tunnelling decay away very quickly in this regime, their effects on subsequent tunnelling process is negligible, leading to uncorrelated, or incoherent, tunneling.

In a regime where all tunnelling events are incoherent and the cavity is in a perpetual thermal state, the Cooper pair tunnelling probability, and therefore the charge dynamics of the junction, can be considered to be small perturbations from the equilibrium. So to calculate the charge dynamics we can turn to perturbation theory[25, 26]. This specific application of perturbation theory, referred to as $P(E)$ theory, uses Fermi's golden rule and a transition Hamiltonian to calculate the rate of particle transfer from an excited quantum state on one side of the junction to a reservoir state on the other side, Γ_{CP}. This theory predicts that in the case of Cooper pairs with energy $2eV$, there

always in the ground state
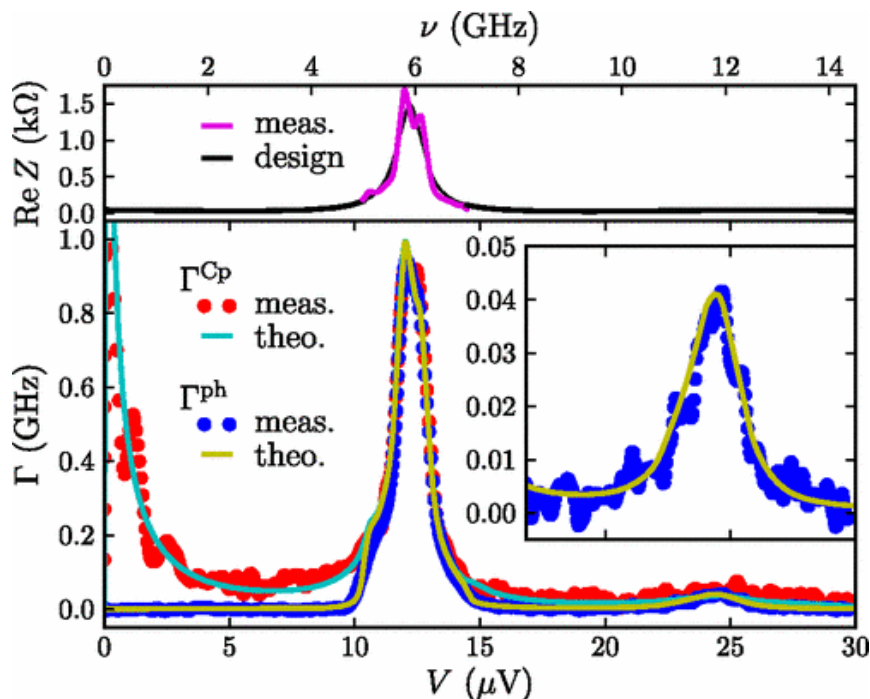
Figure 2.3: Top: The theoretical and measured impedance of the circuit, showing a spike associated with the fundamental cavity mode. Main: The theoretical and measured rates of Cooper pair tunnelling events and the rate of photons leaving the cavity. The simultaneous peak in photon and Cooper pair current when the $2eV = \hbar\omega$ indicates that there is a one to one energy conversion of tunnelling Cooper pairs to photons being produced in the cavity. The inset shows the higher order resonance where $2e \approx 2\hbar\omega$ .Reprinted figure with permission from M. Hofheinz, F. Portier, Q. Baudouin, P. Joyez, D. Vion, P. Bertet, P. Roche, and D. Esteve, Bright Side of the Coulomb Blockade, Phys. Rev. Lett. 106, 217005, 2011. Copyright 2021 by the American Physical Society

is a significant increase in the tunnel probability when this energy matches a multiple of the mode energy, $2eV = n\hbar\omega$, corresponding to one Cooper pair tunnelling and creating n photons in a mode of the cavity.

2.3.3 Simultaneous Cooper pair and photon current monitoring

In early experiments like that of Holst et al., the Cooper pair tunnel current was the only degree of freedom monitored. However, this leaves half the story unobserved. Being able to monitor the photonic dynamics of these systems is necessary to both confirm the previous assumption about photon generation and study any more exotic photon dynamics that may emerge when we leave the low Q regime. The idea of simultaneous monitoring for Cooper pair and photon current was first experimentally explored by Hofheinz et al. in 2011[14].

In their main experiment, Hofheinz et al. constructed a Josephson junction cavity system in such a way that they could simultaneously monitor the current running through the junction, $2e\Gamma_{CP}$, and the rate at which photons leak out of the cavity, the photonic current Γ_{Ph}. They then measured these two quantities as the voltage was varied across the junction, thus adjusting the energy that each of the Cooper pairs possesses. Their main result, Fig 2.3, clearly shows simultaneous spikes in Γ_{CP} and Γ_{Ph} when the energy of the Cooper pairs, $2eV$, matched that of a mode present in the cavity. It is clear from Fig 2.3 that these rates are almost identical, and thus it was concluded that this was indeed a case of one Cooper pair tunnelling through the junction and creating one photon of equal energy that almost instantaneously left the cavity.

While Hofheinz et al. did confirm beyond all reasonable doubt the idea that connecting the junction to a cavity and matching energies could allow for a current to flow through the process of energy exchange and inelastic tunnelling, the foundation of this experiment was still rooted in the low Q, weak E_J, regime. However, it is clear that these dynamics were not the entire story and that a much wider range of quantum behaviours could be accesses if these constraints were shed.

2.4 Theory of Josephson Junction Cavity Systems

We have discussed extensively the early development of Josephson junction photonics, but our discussion has been limited to that of the close to equilibrium case where the drive is weak, and the loss is strong. In this case, the nonequilibrium photon population is so small that its effect can be neglected, allowing the simple perturbation approach (P(E) theory) to be applied. However, this is an incredibly narrow case of the system's dynamics and fails to show a lot of the interesting quantum phenomena that the system is capable of when a larger nonequilibrium photon population is allowed to exist[7].

The main new innovation in the theoretical description came from a switch in focus. $P(E)$ theory focuses on the probability of Cooper pairs tunnelling through a junction, with the probability being defined by the fluctuations in the superconducting phase across the junction. The focus here is the junction and the current running through it, with the cavity simply being assumed to be in thermal equilibrium. However, this is not sufficient when the nonequilibrium photons in the cavity begin to have a significant effect on the tunnelling probability, and they can no longer be described as a perturbation. In this case, we turn to a photonic description of the system, focusing on the

dynamics of the cavity with the junction forming a drive term in the Hamiltonian. This new approach will then use the principles of open quantum systems to calculate the dynamics of the photon statistics within the cavity.

This new theoretical regime was first explored by Armour et al.[27] who considered a Josephson junction embedded into a microwave frequency resonator. The junction was embedded at an anti-node of the resonator and provides a connection between the central conductor of the resonator and the ground plate that surrounds the resonator. A voltage, V, can then be placed across the junction, and it would act as a driving force for the resonator.

When constructing a Hamiltonian for the system, Armour et al. modelled the cavity as multiple LC oscillators in series with each other as well as a single Josephson junction, like the circuit shown in Fig 2.1. Each LC oscillator represented a single accessible mode of the cavity and displayed a natural frequency of $\omega_i = 1/\sqrt{L_i C_i}$ for the ith oscillator in the chain. A classical Hamiltonian for the system can be derived by applying the Kirchhoff's laws[38] to the circuit and using the classical Josephson relations (equations 2.2 and 2.3). This Hamiltonian can then be quantized using canonical quantization rules to find the corresponding quantum Hamiltonian. Performing this procedure, Armour et al. concluded that the full Hamiltonian for the system's quantum dynamics was of the form,

$$H = \sum_i \hbar\omega_i a_i^\dagger a_i - E_J \cos(\omega_J t + \sum_i \Delta_i(a_i + a_i^\dagger)), \qquad (2.4)$$

where a_i and $a_i^\dagger$ are the photonic creation and annihilation operators for the ith cavity mode, $\Delta_i = (2e^2\sqrt{L_i/C_i}/\hbar)^{1/2}$ is the strength of the zero point flux fluctuations of the mode, E_J is the Josephson energy, and $\omega_J = 2eV/\hbar$ is the Josephson frequency which is solely derived from the voltage between the ground plate and the central conductor across the junction.

Equation (2.4) can be split up into two distinct parts. The first term, $\sum_i \hbar\omega_i a_i^\dagger a_i$, describes a set of quantum harmonic oscillators. The second term, $E_J \cos(\omega_J t + \sum_i \Delta_i(a_i + a_i^\dagger))$, describes the effect that the junction has on the coherent evolution of the cavity modes. The value inside the cosine term is known as the superconducting phase and consists of two parts, the first, $\omega_J t$, is the term from the AC Josephson effect, and $\Delta_i(a_i + a_i^\dagger)$ is dependent on the canonical position operator, $x_i = a_i + a_i^\dagger$ for each of the modes, and describes how the cavity affects the Cooper pairs tunnelling through the junction.

Equation (2.4) is complicated because of its explicit time dependence and its strongly non-linear character. However, provided the system is close to a specific resonance, a rotating wave approximation (RWA) can be used to remove the time dependence.

The RWA is rooted in the idea that in an oscillating dynamical system only one frequency will dominate the solution and only processes that also oscillate at these frequencies will contribute to this solution. As such, all other frequencies that are present within a problem can be stripped away without losing any important information about the dynamical solution. This idea, when applied in combination with a transformation to a rotating frame, effectively turns an equation with an infinite number of terms all oscillating at their own frequency to a time independent one.

To apply the RWA to equation (2.4), Armour et al. first had to make a choice about what resonance they wished to study. The obvious choice would be to choose a voltage such that $\omega_J \approx p\omega_0$ for a case where only one oscillator is likely to be excited. This indicates a case where one Cooper pair tunnelling through the junction has equal energy to p photons within the oscillator with frequency ω_0. This is known as a p photon resonance. In this case, the dominant frequency of the system will still be the natural frequency of the cavity mode, ω_0, and thus they chose to move the system in a frame rotating at ω_J/p. In quantum mechanics, this is the equivalent to applying the unitary transformation $e^{i(\omega_J/p)a^\dagger a t}$. Applying the Baker-Hausdorff formula to write the cosine as a product of exponentials, all terms that are not stationary can then be dropped from the equation, leading to the explicitly time independent form of the Hamiltonian,

$$H^{(p)} = \hbar\delta^{(p)}a^\dagger a - \frac{(-i)^p}{2} : [(a^\dagger)^{(p)} + (-1)^p a^p]\frac{J_p(2\Delta_0\sqrt{a^\dagger a})}{(a^\dagger a)^{(p/2)}} :, \tag{2.5}$$

where $\delta^{(p)} = \omega_0 - (\omega_J/p)$, $\tilde{E}_J = E_J e^{-\Delta_0^2/2}$, and $J_p(z)$ is the pth Bessel function of the first kind. The : ... : symbol here indicates that the term in between should be considered to have normal operator ordering. We can justify neglecting the other modes here as they are assumed to be far from resonance, and thus have a negligible effect on the overall dynamics of the system.

While the Hamiltonian describes the coherent dynamics of quantum systems, these dynamics are not produced directly in experiment. The reason for this is simple. In reality, quantum circuits are in contact with the outside world in some way, which means that energy will be exchanged between the two. This exchange leads to decoherence occurring with the system and, if the system is not driven, a gradual move away from quantum dynamics to classical dynamics. The study of

the interaction of quantum systems with the environment is known as the study of open quantum systems.

In the study of open quantum systems, the interaction between the environment and the system can be quantified and the effects on the dynamics of the system understood. For a microwave cavity system this interaction is simple, photons can be lost from the system to the environment, and photons from the environment can be injected into the system[61]. Each of these processes are defined to happen at a constant rate, thus the number of photons that are actually exchanged is dependent on the photon population in the cavity and the temperature of its surroundings. A common assumption when working with quantum systems is that the environment is at zero temperature, $T = 0^3$, and thus any photons that are lost to the environment are moved away from the system fast enough that they will have no effect on future dynamics. The consequence of these assumptions is that the system is not able to gain any energy from the environment, and thus we must only worry about loss from the cavity.

To model the open quantum dynamics, we turn to the Lindblad quantum master equation[61], which describes the time evolution of the system's density operator, ρ, and is of form,

$$\dot{\rho} = -\frac{i}{\hbar}[H, \rho] - \frac{\gamma}{2}\{a^\dagger a\rho + \rho a^\dagger a - 2a\rho a^\dagger\}, \tag{2.6}$$

where γ is the damping rate of the cavity mode [61]. This equation can be separated out into two distinct terms. The first term is the commutator between the system's Hamiltonian and the density operator and provides the coherent dynamics of the system. The second term is the incoherent dynamics of the system, describing the process of photons leaving the cavity into the environment. This term is derived from the Lindblad jump operator, which for a microwave cavity is of the form $L = \sqrt{\gamma}a$ where γ is the rate at which photons leak from the resonator.

It is worth taking a moment to question the validity of using the Lindblad master equation in this class of problems. The Lindblad approach is simple to use, which makes it attractive for calculations. The basic justification for its use is that we assume that the cavity frequency is much larger than the other frequency scales in the system (including the damping rate and the Josephson Energy scaled by $\hbar$)[62]. This approach has been found to yield good results when compared to experiments using JJ-cavity systems[35, 36].

---

[3]Typical frequencies used in experiments are around $5GHz$ at typical experimental temperatures of about 20mK they have thermal occupation numbers much less than unity, which makes this a good approximation to adopt
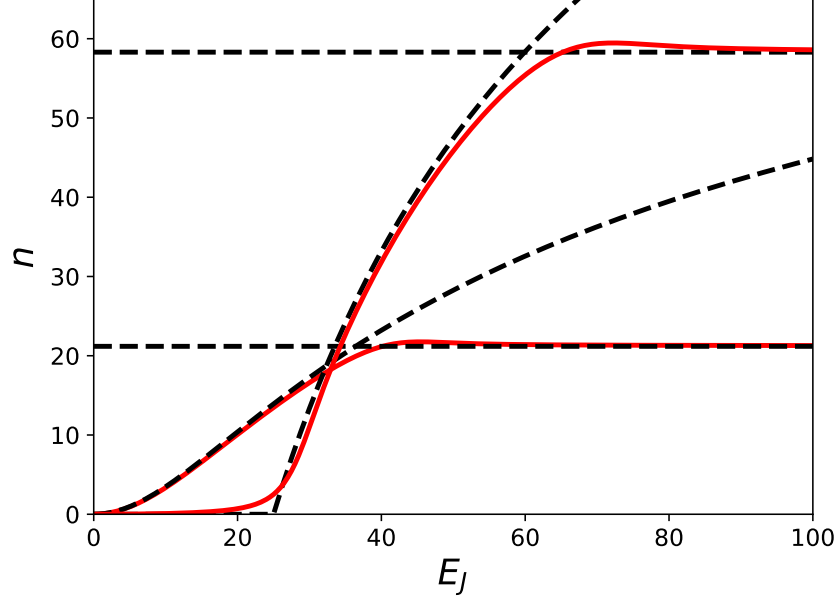
Figure 2.4: The numerically calculated average steady-state photon population, $\langle n \rangle$, of a cavity driven at the $p = 1$ (red lower) and $p = 2$ (red upper) photonic resonances and the theoretical values predicted by the semiclassical RWA method (black dotted), plotted against the Josephson energy of the junction. In these simulations 200 quantum states were available, $N = 200$, $\Delta = 0.2$, units were adopted such $\hbar\gamma = 1$ and the RWA Hamiltonian was used.

A second approximation that can be applied to this system is the semiclassical approximation. In this case, the average dynamics are considered to be described accurately by the expectation value of a, $\langle a \rangle = \alpha$ together with small quantum fluctuations, δa. Thus, a semiclassical dynamical equation can be found by substituting equation (2.5) into (2.6) and then applying the approximation $a = \alpha + \delta a$ and ignoring the higher than quadratic terms in δa and $\delta a^{\dagger}$. These equations could then be further broken down by using the fact that α is a complex number and can be written as $\alpha = Ae^{-i\psi}$, to write separate equations for $\dot{A}$ and $\dot{\psi}$. If these equations are solved, the photonic dynamics can then be deduced. Where fluctuations play an important role, we can use the most basic relationship $\langle n \rangle = \langle a^{\dagger}a \rangle = Ae^{i\psi}Ae^{-i\psi} = A^2$ to evaluate the average photon population in the steady state of the cavity.

This formulation was tested upon two different cases in Armour et al.'s original paper[27], $p = 1$ and $p = 2$ corresponding to the one and two photon resonances, both shown in Fig 2.4. For the $p = 1$ case, the system was shown to demonstrate two stable possible fixed point solutions, one in which A increased with E_J and $\psi = 0$ was fixed (type 1 fixed point shown in the initial rise in Fig

2.4), and another where ψ moved with E_J and $J_p'(2\Delta_0 A) = 0$ was fixed (type 2 fixed point shown in the flat plateau in Fig 2.4). At the crossover point between these two solutions, a bifurcation occurs in the solution for ψ. For $p = 2$, The type 1 and type 2 fixed points are still present, however there is an additional fixed point present at $A = 0$. Thus, for very low E_J the system will display no oscillations until the $A = 0$ solution destabilises and the type 1 fixed point becomes the only stable solution. In this case, the system is required to reach a threshold in terms of E_J to move away from this $A = 0$ fixed point. This is a commonality for all case with $p > 1$.

While the photon population of the cavity is an interesting quantity, it does not tell us much about the underling quantum state, and in fact could be predicted by classical approximations. Studies into the quantum properties must turn to measuring more fundamentally quantum quantities.

One such quality is the the photon Fano factor. The the photon Fano factor is a measure of the quantum fluctuations, and thus the shape of the number distribution in the steady state, and can be written to be of the form,

$$F_n = \frac{\langle n \rangle^2 - \langle n^2 \rangle}{\langle n \rangle}. \tag{2.7}$$

where $n = a^\dagger a$ is the number operator of the cavity. $F_n = 1$ indicates that the system is in a coherent state (with a perfectly Poissonian distribution of photons), however if $F_n < 1$ then the system is undergoing number squeezing (leading to a non-classical state) and the photon distribution is now sub-Poissionian, i.e. the distribution of Fock states that make up the system's steady state are biased towards the central spike. When $F_n < 1$[63], this indicates that the photons leaking out of the cavity are undergoing anti-bunching, i.e. if one photon leaves at a time t the chances of another photon leaving at the same time is reduced (see also the discussion around (2.10)). It is also possible to obtain an expression for the average Cooper-pair current using a current operator formulated in terms of a and $a^\dagger$ [28].

$$I_{CP} = \frac{eE_J}{\hbar} : \frac{J(2\Delta_0\sqrt{a^\dagger a})}{\sqrt{a^\dagger a}}(a + a^\dagger) :, \tag{2.8}$$

for $p = 1$, with fluctuations measured by,

$$F_{CP} = \frac{1}{2e\langle I_{CP}\rangle}2Re\int_0^\infty d\tau[\langle I_{CP}(t+\tau)I_{CP}(t)\rangle - \langle I_{CP}\rangle^2] \tag{2.9}$$
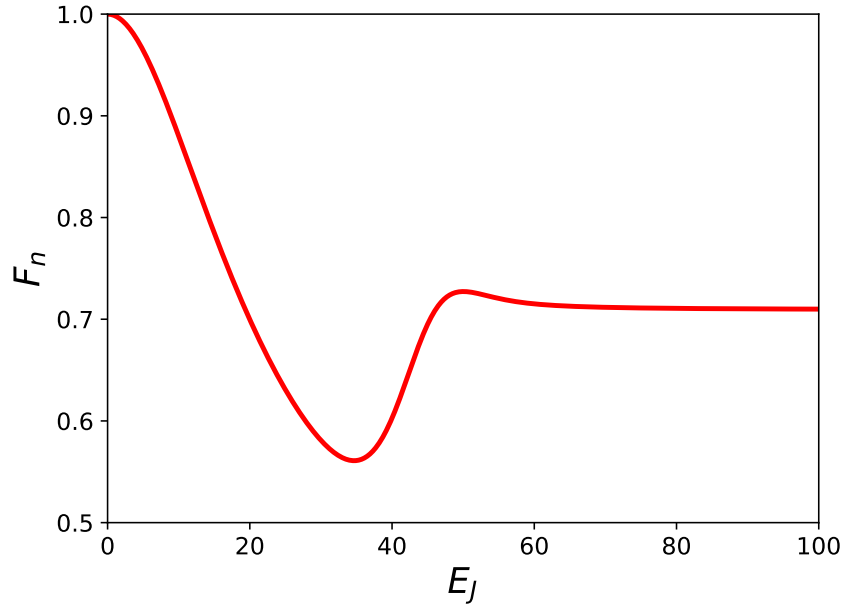
Figure 2.5: The numerically calculated Photonic Fano factor for the $p = 1$ resonance, plotted against the Josephson energy of the junction, showing the transition from incoherent tunnelling in the low energy limit to coherent tunnelling indicated by a sub-Poissionian photon emotion distribution. In these simulations 200 quantum states were available, $N = 200$, $\gamma\hbar = 1$, $\Delta = 0.2$ and the RWA Hamiltonian was used.

where the long time limit $(t \rightarrow \infty)$ is assumed. Note that F_n and F_{CP} are both relative measurements of fluctuations in the cavity occupation and current respectively.

Armour et al. observed a transition from a state with $F_n = 1$, Fig 2.5, in the limit of weak driving, to a state where $F_n < 1$ in the case of $p = 1$. This behaviour is associated with the transition from a coherent state present in the cavity with a random photon emission from the cavity and incoherent tunnelling of Cooper pars through the junction, to an anti-bunched emission of photons and coherent tunnelling of Cooper pairs through the junction[4]. This is a consequence of the increasing population of the cavity, as more photons are present in the cavity they begin to have back-action onto the junction, promoting stimulated emission of photons and thus the coherent tunnelling of Cooper pairs through the junction. This effect has recently been observed experimentally by Ménard et al. [35]. A very similar phenomenon was also theorized by Gramich et al. but with a much greater emphasis on the tunnelling of the Cooper pairs rather than the photon population[29]. Similar results have also been shown in a related JJ-cavity system[64]

---

[4]An equivalent drop in F_{CP} would also be observed to indicate this.

While this non-classical emission is interesting, for practical use as an on-demand photon source the system must be shown to display complete photon anti-bunching. In this case, the presence of a photon in the cavity affects the state so much that it blocks any further tunnelling of Cooper pairs through the junction, i.e. making the matrix element that governs the probability of transition from one photon in the cavity to two photons become zero, $\langle 1| H^{(1)} |2\rangle = 0$. This is known as a photon blockade. The position of this point in parameter space was described by Rolland et al. and it was found to occur at $\Delta_0 = \sqrt{2}$[36] independent of all other parameters. To relate this to measurements made in the lab, theorists turn to the zero-time, normalized, second order correlation function $g^{(2)}(0)$, which takes the form

$$g^{(2)}(0) = \frac{\langle a^\dagger a^\dagger a a\rangle}{\langle a^\dagger a\rangle^2} = \frac{\langle n^2\rangle - \langle n\rangle}{\langle n^2\rangle}. \tag{2.10}$$

This is again a measure of photon emission randomness[5], with $g^{(2)}(0) = 1$ indicating a perfectly random photon emission according to a Poissian distribution, $g^{(2)}(0) < 1$ indicates a system that is undergoing anti-bunching, and $g^{(2)}(0) = 0$ is a system with no possibility of simultaneous photon emission. The predicted $g^{(2)}(0)$ value for the $p = 1$ resonance can be seen in Fig 2.6 as a function of Δ_0 and it is clear that this value becomes vanishingly small at $\Delta_0 = \sqrt{2}$ within the constraints of the RWA approximation. In the case where the RWA is not used, it is expected that $g^{(2)}(0)$ would be small but not vanishing due to higher order corrections which are present in the original time dependent Hamiltonian but are neglected by the RWA. In experiments Δ_0 is a very hard thing to try and manufacture and Rolland et al. only managed to produce a resonator with $\Delta_0 = 0.97$, however this still showed a significant reduction in $g^{(2)}(0)$ and matched theory well. This implies that if a cavity could be engineered to have $\Delta_0 = \sqrt{2}$, these systems could be used as a source for single photons.

2.5   The Josephson Junction Laser

So far, we have analysed situations in which only one cavity mode is excited. However, recent experiments[31] and theoretical work[32] has explored cases where multiple modes play an important role. This work has concentrated on cases where the fundamental mode can become redexcited even

---

[5] $g^{(2)}(0)$ and F_n are closely related quantities, but useful within different regimes. $g^{(2)}(0)$ tends to show interesting features better in the weak driving regime whereas F_n performs better in stronger driving regimes[65]
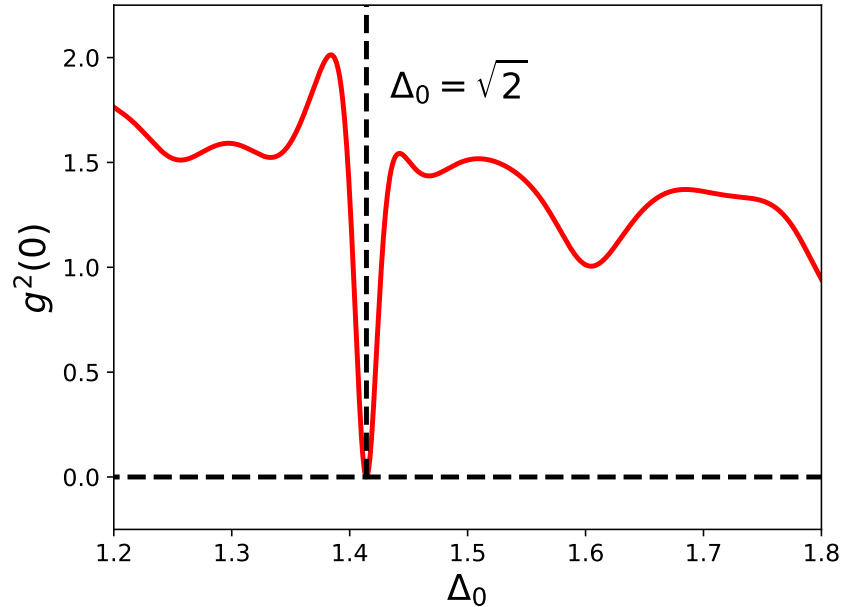
Figure 2.6: The numerically calculated $g^{(2)}(0)$ function for the $p = 1$ photonic resonance, showing the vanishing point at $\Delta_0 = \sqrt{2}$ when the $\langle 1| H |2\rangle$ matrix element vanishes, thus forbidding more than one photon to be present in the cavity. Simulation was performed at with ten accessible quantum states, $N = 10$, $E_J = 100$, and units such that $\hbar\gamma = 1$, using the RWA Hamiltonian.

when the applied voltage matches a much higher harmonic. The resulting state has been dubbed the 'Josephson junction laser' as the cavity displayed coherent emission[31].

The use of superconducting resonators to produce coherent light has been studied before[7, 19, 66, 67]. However, the first attempt to build a single Josephson junction cavity embedded laser was by Cassidy et al. in 2017[31]. They constructed a redhalf coplanar waveguide with a voltage biased DC superconducting quantum interference device (DC-SQUID) embedded at one of the anti-nodes which acted as a tunable Josephson junction driving a cavity with multiple modes. Cassidy et al. showed that this set up could demonstrate the hallmarks of being a laser light source such as the system demonstrating a lasing threshold, emission spectra narrowing to less than 1Hz width, and injection locking. Because of this, it is thought that this system could be used as a quantum limited amplifier for photonic systems, though it is not the only Josephson system to display this behaviour[68].

The use of the term laser here may seem somewhat overly prescriptive as, when we discuss the system in this thesis, we will only describe phenomena associated with coherent light sources, rather than lasers specifically. However in their experimental exploration of the system, Cassidy

et al. did demonstrate several key behaviours of lasing. As such, we will choose to preserve the language used by Cassidy et al. for the remainder of this thesis for the sake of consistency.

While Cassidy et al. managed to demonstrate this laser in practice, theoretical evaluation of the system's properties has proven to be far more difficult. Photon emission in the cavity-junction system is an inherently quantum mechanical process, relying on the idea of discrete energy levels to allow the photons to interact with the Cooper pairs. Thus, when formulating a theoretical model of this system it would be sensible to start with the multi-mode Hamiltonian for the junction cavity system, (3.1), and solve for the dynamics using the Lindblad master equation, equation 2.6. This is very similar to how the theoretical framework was considered for the single mode case. However, we immediately run into a problem of scales. While the actual equations for the quantum case are not all that complex, the numerical solution to them prove much more difficult because of the potentially enormous state space involved.

With this in mind, Cassidy et al. chose to turn to a classical description of the system. To do this they modelled the system as a series of N connected harmonic oscillators driven by a Josephson junction with a phase (difference) determined by the sum of the amplitude of all the modes, similar to that shown in Fig 2.1. This gave an equation of motion for the nth mode's amplitude, ψ_n, of form,

$$C_n \ddot{\psi}_n = i^2 \mathrm{L}^{-1} \psi_n - \gamma \dot{\psi}_n + \Phi_0^{-2} \alpha_n \sin(\omega_J t + \sum_i^N \alpha_i \psi_i) \tag{2.11}$$

where α_n is a geometric factor depending on the shape of the cavity, C_n is the mode capacitance, L_n is the mode inductance, γ is the loss to a transmission line adjacent to the cavity, and Φ_0 is the magnetic flux quantum. From this, Cassidy et al. found that for relatively small $N \approx 20$ and high $Q = \omega_1/\gamma \approx 10^5$ that the system would move from emission into the fundamental mode, ω_0, that only occurred for values of ω_J that were small integer multiples of ω_0 at low drives (i.e. low E_J values), to strong emission across a very wide range of ω_J at sufficiently strong drive. Additionally, increasing the total number of modes lead to a narrowing of the system's emission spectra. Despite its change in form, this Hamiltonian is actually only a slight extension of (2.4) and those studied in the wider literature[27, 29, 60]

However, this theoretical exploration was hardly exhaustive and still required a significant amount of computation power to solve [6] for large N. A new approach was proposed by Simon

---

[6]See Appendix C for a detailed discussion of how to solve these systems numerically and the issues that this raises.

and Cooper[32]. They began by writing Cassidy et. al's dynamical equations in the more compact form,

$$\ddot{\psi}_n = -\omega_n^2 \psi_n - 2\gamma\dot{\psi}_n + \alpha_n \lambda \sin(Vt + \sum_k \alpha_k \psi_k). \tag{2.12}$$

Here ω_n is the natural frequency of the nth mode, the drive strength is $\lambda = \frac{E_J}{C}(\frac{2e}{\hbar})^2$ with E_J the Josephson energy, C is the total capacitance of the cavity, and $\frac{\hbar}{2e}$ is the flux quantum. Also, V is now the voltage bias placed across the junction scaled by one over the flux quantum(i.e. ω_J) and γ is the loss in each mode which is assumed to be the same for all modes.

As Cassidy et al. found, it is not possible to analytically solve this set of equations in all but the simplest cases. However, Simon and Cooper[32] proposed a solution to this, instead of calculating the dynamics of each individual mode they chose to calculate the collective dynamics of the system, trading specificity for calculation speed. This is actually following logically from (2.12) as it is clear that the superconducting phase, and therefore the interaction between the modes, only depends on the collective amplitude $\sum_n \alpha_n \psi_n$ and as such there is no need to calculate each mode individually.

To proceed they defined a new collective amplitude of all modes $\Psi = \sum_n \alpha_n \psi_n$, however, this still left them with the issue of finding a generic expression for a solution of Ψ from (2.12). For this, they turned to Green's functions[69]. Consider a generic inhomogeneous differential equation of form,

$$\mathcal{D}y(x) = f(x), \tag{2.13}$$

where $\mathcal{D}$ is some unspecified Hermitian differential operator. If this problem is bounded between the values a and b we can consider the solution to be of form,

$$y(x) = \int_a^b dz G(x, z) f(z) \tag{2.14}$$

where $G(x, z)$ is the Green's function of the operator $\mathcal{D}$. This approach works particularly well in our case, as the Green's function is completely independent of the equation's inhomogeneity. Hence, we can consider the Green's function of any individual mode to be that of a damped harmonic oscillator,

$$G_n(t) = \Theta(t)e^{-\gamma t}\frac{\sin(\sqrt{\omega_n^2 - \gamma^2}t)}{\sqrt{\omega_n^2 - \gamma^2}}, \tag{2.15}$$

where $\Theta(t)$ is a Heaviside step function which moves from 0 to 1 at $t = 0$. Since the inhomogeneity

and limits are the same for every mode it can be quickly shown that the collective dynamics of the cavity is described by,

$$\Psi(t) = \lambda \int_{-\infty}^{t} dt' K(t - t') \sin(Vt' + \Psi(t')) \tag{2.16}$$

where $K(t)$ is known as the kernel of the system and is defined as,

$$K(t) = e^{-\gamma t} \sum_{n} \alpha_n^2 \Theta(t) \frac{\sin(\sqrt{\omega_n^2 - \gamma^2}t)}{\sqrt{\omega_n^2 - \gamma^2}}. \tag{2.17}$$

In this collective description the dynamics can be obtained from equation(2.16), which is known as a nonlinear Volterra equation of the second kind [70]. This is a significantly less taxing equation to solve than solving each of the individual mode equations when N is very large. Given the implicit character of the integral equation, with the solution at $\Psi(t)$ depending on Ψ at earlier times, we can adopt a Marching Method to solve it numerically[7][70]. In the limit of weak dissipation, defined as $\gamma \ll \omega_1$, the kernel can be replaced by the much simpler form,

$$K(t) \approx e^{-\gamma t} \sum_{n} \alpha_n^2 \Theta(t) \frac{\sin(\omega_n t)}{\omega_n} = e^{-\gamma t} K_0(t). \tag{2.18}$$

In the case of $\alpha_n = 1$ for all n, and $\omega_n = n\omega_0$, where all frequencies are sequential integer multiples of the natural frequency of the cavity, this sum when taken to a large number of modes, leads to a sawtooth waveform. In the limit of an infinite number of modes and no damping, this leads to a kernel of form[32],

$$K_0(t) = \frac{1}{2}[T/2 - t(\text{ mod } T))], \tag{2.19}$$

where T is the period of the fundamental mode, $2\pi/\omega_0$. In this equation, the $t(\text{ mod } T)$ term linearly increases from 0 to T before discontinuously resetting to 0, thus forming a sawtooth wave with period T.

While (2.16) is an improvement on (2.12) in both memory use and speed (of solution) it is still a challenging endeavour to solve it. To calculate the ith point in the numerical integration all previous points, $0, ..., i-1$, in the integration must be summed. This means any numerical program that calculated this must slow done as the integration time increases. Furthermore, the limit of $-\infty$ in the integration in equation (2.16) is inconvenient.

---

[7]Again, a much more detailed discussion of this method can be found in Appendix C along with possible alternative methods that could be utilized.

To solve these issues as well as allow more analytical information to be discerned, Simon and Cooper chose to further simply the system[32]. To do this, we split the integration in equation (2.16) into two parts,

$$\Psi(t) = e^{-\gamma T} \lambda \int_{-\infty}^{t-T} dt' e^{-\gamma(t-T-t')} K_0(t-T-t') \sin(Vt' + \Psi(t'))$$

$$+ \lambda \int_{t-T}^{t} dt' e^{-\gamma(t-t')} K_0(t-t') \sin(Vt' + \Psi(t')), \tag{2.20}$$

where we have used the periodic nature of K_0 such that $K_0(t-T-t') = K_0(t-t')$. Hence, we can reformulate Equation (2.20) to be,

$$\Psi(t) = e^{-\gamma T} \Psi(t-T) + \lambda \int_{t-T}^{t} dt' e^{-\gamma(t-t')} K_0(t-t') \sin(Vt' + \Psi(t')), \tag{2.21}$$

which is still a Volterra equation of the second kind [70] and we will refer to it as the Truncated Volterra equation. Because the value of the nth step in the solution, now only relies on the value of the integration one period ago and however many integration points are chosen over a period T, it is clear that solutions to this equation should only scale linearly in time.

Another key advantage to Equation (2.21) is it can yield a analytical approximation in specific cases. In the case of $\gamma = 0$ and a voltage set such that $V = V_m = 2\pi m/T$ where m is an integer, equation (2.21) can be solved by looking for a periodic solution, $\Psi(t) = \Psi(t+T)$ which corresponds to finding a solution where the sin term is constant. This is because the integral over the period will then be zero as K_0 will be perfectly periodic over T. From this, a solution for Ψ is found to be,

$$\Psi(t) \ (\text{mod } 2\pi) = -V_m t + \beta \tag{2.22}$$

where β is some constant. This is a constantly decreasing function, with the modulo inserting m phase slips of 2π per period. These phase slips must occur at the same points in each period in order to satisfy the periodic requirement. Thus, the system will form a sawtooth wave oscillation. This result can be considered the main result in Simon and Cooper's paper, and it is corroborated by the numerical calculations that they performed where, for weak drive and integer V, the system did form a sawtooth wave with m 2π phase slips per period of fundamental mode.

However, a number of important questions about the system's dynamics remain unanswered by

Simon and Cooper's analysis. Although they identify a sawtooth solution for Ψ with the period of the fundamental mode, T, it is not clear when this becomes the stable solution. For weak drives (i.e. low λ) perturbation theory leads instead to a periodicity for Ψ set by the drive, $\frac{2\pi}{V}$. Furthermore, it is not clear what role the number of modes played in the dynamics. We will return to explore these questions in Chapters 4 and 5.

Chapter 3

Double Cooper-pair Tunnelling

3.1　Introduction

In chapter 2 we reviewed recent research on a voltage biased Josephson junction connected to a single cavity mode. In this system, the dynamics of the photon population and the Cooper pair tunnelling rate are largely determined by the ratio of the Josephson frequency to the cavity frequencies, $p = \omega_J/\omega_0$. Historically, the case where this ratio is a positive integer, i.e. where one Cooper pair tunnels has sufficient energy to produce one or more photons in the cavity, has been extensively explored. This is because in experiment these integer resonances tend to be the easiest to observe[14, 23] due to the strong resonance produced compared to non-resonant processes. Additionally, theoretical dynamics can be quite easily calculated using either $P(E)$ theory[25, 26], in the case of weak driving (i.e. close to equilibrium) and lend themselves to a RWA description for the far from equilibrium case that is relevant for strong drives[27, 29, 65]. Extensive theoretical exploration has occurred for the $p = 1$ and $p = 2$ cases[27, 29, 65], as well as higher order resonances[29, 30], and systems which involve multiple cavities all at integer resonances[65, 71]. This family of resonances are known as subharmonic resonances.

Very little study has been directed towards superharmonic resonances, i.e. the case where the ratio ω_0/ω_J forms an integer larger than one. In this case, multiple simultaneous Cooper pair tunneling events are required to produce a photon in the cavity and thus allow a current to flow through the junction. While these types of resonance have been discussed theoretically[60] in a
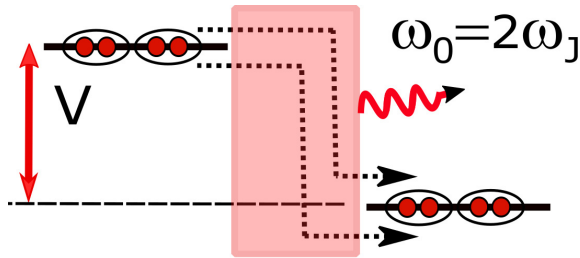
Figure 3.1: The energy level diagram showing the difference in energy between the two sides of a JJ and the resonance condition for the two Cooper pair tunnelling and single photon production to occur. Here the junction frequency is $\omega_J = 2eV/\hbar$ and the cavity mode has frequency ω_0.

classical JJ-cavity system, no attempt at a full description in either the classical or quantum regime has been attempted, though some work with SQUID circuits have alluded to it though symmetry arguments[72].

In this chapter, we provide a detailed analysis of the case where $\omega_0/\omega_J = 2$, i.e. where two Cooper pairs must simultaneously tunnel to produce a single photon. This tunneling process is shown in Fig 3.2. We will examine the Hamiltonian for the JJ-cavity system with a voltage bias tuned to the two Cooper pair resonance condition. It will be shown that this model can be reduced to a simpler, analytically solvable form in the low energy limit when, either the system is moved to a rotating frame and a second order rotating wave approximation[73] is performed, or a semi-classical approximation is taken. We will show that the cavity photon population can, under intermediate drive, be described accurately by the effective Hamiltonian derived using the (second order) rotating wave approximation; however, in the limit of very weak driving this approach fails, and the system can only be described by the semi-classical description.

This approach will be explained by the charge dynamics of the system undergoing a transition from a regime of very low driving, dominated by single Cooper pair tunnelling processes, to one where two Cooper Pair tunnelling processes dominate for stronger drives. This is accompanied by a transition from incoherent to coherent (double) Cooper pair tunnelling, and the photons emitted from the cavity become anti-bunched. Finally, we will show that for certain specific parameters, an interference effect can be set up in the cavity wave function such that the system becomes trapped in the first two Fock states. This allows the system to become a source of single photons on-chip.

This chapter will begin with a brief description of the system set up and the mathematics behind the Hamiltonian in section 3.2. In section 3.3 we will discuss the difficulties faced in solving the

system's dynamics and introduce the second order rotating wave approximation as a method for facilitating its solution. Section 3.4 will expand on this, giving a description of two low energy approximations: An approximation of the rotating wave Hamiltonian and a classical equation of motion for the expectation value of the cavity raising operator. Photonic properties will be explored in section 3.5, and the charge dynamics and noise will be examined in section 3.6. In section 3.7 we will examine the system in the strongly non-linear regime and find a parameter regime in which the system acts as an on-chip single photon source. Finally, in section 3.8 we will conclude our examination and look to possible future work.

Details of the work presented in this chapter were published in Phys. Rev B **100** 054515 (2019)[33].

3.2 Model System

Consider a circuit of design shown in Fig 3.2, where the junction is connected to a single harmonic oscillator. The oscillator has a natural frequency of $\omega_0 = 1/\sqrt{LC}$, and when the system is biased by an external voltage source, V, the JJ has a characteristic frequency of $\omega_J = 2\frac{eV}{\hbar}$.

As was described in chapter 2, the Hamiltonian for the system can be derived from Kirchhoff's laws[27, 60] and the canonical quantization relations and is of form,

$$H(t) = \hbar\omega_0 a^\dagger a - E_J \cos(\omega_J t - \varphi + \Delta_0(a + a^\dagger)), \tag{3.1}$$

where a is the annihilation operator of the quantum harmonic oscillator, E_J is the Josephson energy,
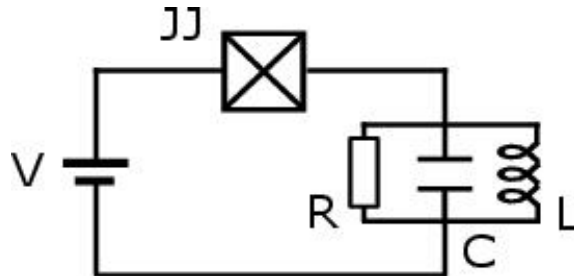

Figure 3.2: The circuit used to explore the dynamics of double charge tunnelling processes. This consists of a voltage source, V, which biases a Josephson junction, JJ, in series with a harmonic, LC, oscillator. The resistor, R, models losses from the cavity into an adjacent transmission line otherwise referred to as the environment.

$\Delta_0 = (2e^2/\hbar)^{1/2}(L/C)^{1/4}$ is the zero point flux fluctuations in the oscillator, and φ is the JJ phase operator which is also the conjugate of the JJ Cooper pair number operator, N, with commutation relation $[\varphi, N] = i$. Note that this constitutes a small extension of the circuit model discussed in chapter 2. In that case, φ was treated as a constant and set to zero, an approach which is valid when low frequency voltage fluctuations can be neglected[29]. However, for us retaining φ is useful even when voltage fluctuations are neglected as it indicates the charge transfer processes that are relevant.

Since we are interested in the case of superharmonic resonances, the ratio of ω_0/ω_J must be, or must be close to, an integer, n. For simplicity, we will only consider the $n = 2$ case here.

The dynamics of the system can be explored fully using the Lindblad equation, equation (2.6) extended to included dephasing of N due to low frequency voltage fluctuations[29]. Thus, we have a master equation of form:

$$\dot{\rho} = -\frac{i}{\hbar}[H, \rho] + \frac{\gamma}{2}\mathcal{D}[a](\rho) + \frac{\gamma_\varphi}{2}\mathcal{D}[N](\rho), \tag{3.2}$$

where ρ is the system's density matrix and $\mathcal{D}[x](\rho) = 2x\rho x^\dagger - x^\dagger x\rho - \rho x^\dagger x$. While included here for completeness, the dephasing is very weak compared to the cavity loss terms, $\gamma_\varphi \ll \gamma$, and can often be neglected[29, 65, 74, 75][1].

Due to the explicit time dependence of equation (3.1), there is no steady state solution. There will instead be a solution, $\rho(t)$, that oscillates at frequencies that are one or more combinations of ω_0 and ω_J. Thus, outside direct numerical integration with a quantum toolbox [76], solutions to equation (3.2) are not possible without approximation.

3.3   The Rotating Wave Approximation

The difficulty with equation(3.2) is the explicit time dependence of the Hamiltonian that excludes the existence of steady state solutions for ρ. Thus, to be able to find a general solution in the limit of long time, we must find a time averaging procedure that can be used to extract an effective time averaged Hamiltonian that facilitates analytic calculations.

---

[1]This is a very common approximation in Josephson dynamical systems, when simulation is compared to experiment it is found that $\gamma_\varphi/\gamma \approx 0.04$[29], validating this assumption unless the process being studied is only a function of γ_φ.

To find this effective Hamiltonian, we must move the system into a rotating frame of reference that matches the frequency of the dominant dynamical processes and then only consider the time independent terms after an average. To do this, we can exploit the fact that the system's behaviour is analogous to that of a classical non-linear oscillator when choosing the frequency of the rotating frame. When a linear oscillator is driven by a frequency different to its natural frequency, the oscillator will eventually conform to the drive frequency. However, for a driven non-linear oscillator, the system will have a tendency to respond at the natural frequency of the oscillator[77]. Thus, if the system is moved into a frame rotating at $2\omega_J \approx \omega_0$ this would capture the system's resonant response to the drive.

Consider a unitary transformation operator, $X(t) = e^{2i\omega_J a^\dagger a t}$, which will move an operator into a frame rotating at $2\omega_J$[27]. Applying this to (3.1) and rearranging the resulting equation, we can see that the transformed Hamiltonian takes the form,

$$\tilde{H}(t) = \hbar\delta a^\dagger a - \frac{\tilde{E}_J}{2} \sum_{q=0}^{\infty} [O_q e^{i(2q+1)\omega_J t} + O_q^\dagger e^{-i(2q+1)\omega_J t}] \tag{3.3}$$

where $\tilde{E}_J = E_J e^{-\Delta_0^2/2}$, $\delta = \omega_0 - 2\omega_J$, and O_q is a operator defined as,

$$O_q =: i^q (a^\dagger)^q e^{-i\varphi} \frac{J_q(2\Delta_0\sqrt{n})}{n^{q/2}} + (-i)^{q+1}(a^\dagger)^{q+1} e^{i\varphi} \frac{J_{q+1}(2\Delta_0\sqrt{n})}{n^{(q+1)/2}} :, \tag{3.4}$$

where n is the cavity number operator, J_q is the qth Bessel function of the first kind, and the operators have been normally ordered, indicated by : ... :. Equation (3.3) cannot simply be time averaged, as all terms are zero when perfectly on resonance or periodic in time. Therefore, we must take a more sophisticated approach when performing a Rotating Wave Approximation. An effective time-averaged Hamiltonian can be defined through the relation[73],

$$H_{eff} = \{\overline{H(t)U(t,t_0)}\}\{\overline{U(t,t_0)}\}^{-1}, \tag{3.5}$$

where $U(t, t_0) = \mathcal{T} \exp(\frac{-i}{\hbar} \int_{t_0}^t H(t')dt')$ is the unitary time evolution operator from a initial time t_0 to t, the bar indicates a time averaged quantity, and $\mathcal{T}$ is the time-ordering operator[2]. The first

---

[2]Note that while $U(t, t_0)$ is unitary and Hermitian as is required for a time evolution operator, the time averaged version of the operator $\overline{U(t,t_0)}$ is neither. This is why (3.5) has the unusual inclusion of $\{\overline{U(t,t_0)}\}^{-1}$ rather than the Hermitian conjugate. Despite this fact, the approximate Hamiltonian we derive for the second order RWA is still clearly Hermitian. See the original derivation[73] for more details.

order expansion of this is simply $H_{eff} = \overline{H(t)}$, which is the standard RWA. However, $\overline{H(t)} = 0$ using equation (3.3) (with $\delta = 0$) and thus the RWA must be expanded past first order[3]. Working to second order it can be shown that the resulting effective Hamiltonian can be written as,

$$H_{eff} = \overline{H(t)} - \frac{i}{\hbar}\overline{(H(t) - \overline{H(t)})\int_{t_0}^{t}(H(t') - \overline{H(t')})dt'}. \qquad (3.6)$$

Using $\overline{H(t)} = 0$ it is trivial to show that the new Hamiltonian is defined by,

$$H_{eff} = \frac{-i}{\hbar}\overline{H(t)\int_{t_0}^{t}H(t')dt'}, \qquad (3.7)$$

which does have non-zero stationary components when applied to (3.3). This is commonly called the 2nd Order Rotating Wave Approximation and has been used before with other cQED based Hamiltonians[78, 79].

Explicitly calculating equation (3.7) with equation (3.3) gives,

$$H_{\text{eff}} = \hbar\delta a^{\dagger}a + \frac{\tilde{E}_J^2}{4\hbar\omega_J}\sum_{q=0}^{\infty}\frac{[O_q, O_q^{\dagger}]}{(2q+1)} = \left(\hbar\delta + \frac{\tilde{E}_J^2\hat{\mathcal{G}}}{4\hbar\omega_J}\right)n - i\frac{\tilde{E}_J^2}{4\hbar\omega_J}\left[\hat{\mathcal{F}}a^{\dagger}e^{2i\varphi} - \text{h.c.}\right] \qquad (3.8)$$

where $\mathcal{G}$ and $\mathcal{F}$ are operators defined as,

$$\mathcal{G}(\Delta_0, n)n = \sum_{p=1}^{\infty}\frac{4p}{4p^2-1}\left[a^{\dagger p} : \frac{J_p(2\Delta_0\sqrt{n})}{n^{p/2}} :, a^p : \frac{J_p(2\Delta_0\sqrt{n})}{n^{p/2}} :\right], \qquad (3.9)$$

$$a\mathcal{F}(\Delta_0, n) = \sum_{p=0}^{\infty}\frac{(-1)^p}{2p+1}\left[a^{\dagger p} : \frac{J_p(2\Delta_0\sqrt{n})}{n^{p/2}} :, a^{p+1} : \frac{J_{p+1}(2\Delta_0\sqrt{n})}{n^{(p+1)/2}} :\right]. \qquad (3.10)$$

Two interesting things arise from (3.8) signalled by the coefficients of $\mathcal{G}$ and $\mathcal{F}$ respectively. Firstly, the n coefficient to the $\mathcal{G}$ operator indicates that it is causing the system to undergo resonance bending, i.e. shifting the resonant frequency based on the drive strength. This shift is similar to behaviours shown by other nonlinear oscillator systems, such as the Duffing oscillator[77], and behaviour that have been observed in the classical super-harmonic regime of the system[60]. Secondly, the coefficient of the $\mathcal{F}$ operator gives insight into the charge and photon dynamics. The factor of

---

[3]This is an issue that is shared with lots of methodologies that mathematically remove time dependence, not only the RWA. For example, a Floquet Hamiltonian, i.e. a Hamiltonian defined by $H_F |u_\alpha(t)\rangle = [H(t) - i\hbar\delta t]|u_\alpha(t)\rangle$ can be derived but, when the required transitions are calculated in the relevant modes, the Fourier components are found to average to zero, giving the same null result as the first order RWA. We chose to use the second order RWA, but we expect that similar results could be derived using the Floquet formalism.

$a^\dagger e^{2i\varphi}$ adjacent to $\mathcal{F}$ indicates that the system is driven by a process that creates a single photon in the cavity, signalled by the presence of a single raising operator, and transfers two Cooper pairs across the junction, which is represented by the $2i\varphi$ in the exponential.

At first sight, equation (3.8) appears to have the same structure as the RWA Hamiltonian, equation (2.5), with two components. One involving just the number operator, n, and a second involving single photon creation (annihilation) operators multiplied by an n-dependent function. The main difference appears to be twofold. Firstly, unlike the one Cooper pair to one photon Hamiltonian, this one-photon and double-Cooper pair Hamiltonian displays a frequency shift away from δ which appears to be a phenomenon unique to the super harmonic regime. Secondly, the coefficients of these components appear to be significantly more complex in the one-photon and double-Cooper pair case. This is likely due to the more complex frequency combinations that are required to derive equation (3.8).

While (3.8) is time independent, $\mathcal{G}$ and $\mathcal{F}$ pose a significant mathematical challenge to work with due to their complexity. While there are methods for finding generalised solutions of commutation relations for functions of creation and annihilation operators, they are cumbersome and yield results that don't necessarily help in solving for the system dynamics. Instead, a more fruitful approach is to consider the system in the limit of weak driving, and thus low energy.

3.4 Low Energy Approximations

3.4.1 Low Energy Rotating Wave Approximation

As we have discussed, (3.8) does not lend itself to analytical solution due to the complexity of the commutation relations, so it is necessary to ask when and how it can be approximated. Since the nonlinear nature of this equation is the reason why analytical work is difficult, we can choose to work in the regime where the nonlinear nature is suppressed, $\Delta_0 \ll 1$. We also can choose to work in the limit of small cavity population, $\Delta_0^2 \langle n \rangle \ll 1$ which is determined by small $\tilde{E}_J$, which suppresses the higher order cavity operators.

Following these conditions, (3.8) can be approximated[4] by,

$$H_{\text{eff}}^{(0)} \approx \hbar\delta'n + i\frac{\tilde{E}_J^2\Delta_0^3}{3\hbar\omega_J}\left[ae^{-2i\varphi} - a^\dagger e^{2i\varphi}\right],$$ (3.11)

up to $\mathcal{O}(\Delta_0^3)$. Here, $\delta' = \delta + 8\tilde{E}_J^2\Delta_0^4/(15\hbar^2\omega_J)$ describes the frequency shift, and it is clear that the two Cooper pair tunnelling terms are preserved from (3.8). A more detailed description about how (3.11) is derived can be found in appendix A.

3.4.2 Low Energy Semi-classical Approximation

One aspect that we have so far neglected to question is the assumption that the system in this regime only oscillates with one frequency. This assumption, however, is not strictly true. From the structure of (3.1) it is clear that the system should exhibit a mix of frequencies composed of integer multiples and fractions of ω_J. Whilst the non-linearity (and a high Q) will allow oscillations at $2\omega_J \approx \omega_0$, at low E_J the nonlinearities are weak and we expect oscillations at ω_J to dominate. To try and capture these dynamics, we must move past the RWA and try and work directly with (3.1) in the low energy limit. The simplest way to do this is to use a semi-classical approximation of the master equation in the form of an approximate equation of motion for a specific operator expectation value.

Consider the definition of the equation of motion for the cavity raising operator expectation value, $\langle\dot{a}\rangle = Tr[a\dot{\rho}]$. Using (3.1) and (3.2) and assuming that $\gamma_\varphi \ll \gamma$ such that charge dephasing can be ignored, it can be shown that,

$$\langle\dot{a}\rangle \approx -\frac{i}{\hbar}\left\langle\frac{\partial H}{\partial a^\dagger}\right\rangle - \frac{\gamma}{2}\langle a\rangle,$$ (3.12)

and by performing a semi-classical approximation in which the system is assumed to be in the coherent state, $|\alpha(t)\rangle$, we can write $\langle f(a, a^\dagger)\rangle = f(\langle a\rangle, \langle a^\dagger\rangle) = f(\alpha, \alpha^*)$ provided that f is normally ordered. The equation of motion for α then becomes,

$$\dot{\alpha} = -\left(\frac{i\omega_0}{\hbar} + \frac{\gamma}{2}\right)\alpha - \frac{i\tilde{E}_J\Delta_0}{\hbar}\sin(\omega_J t + \Delta_0(\alpha^* + \alpha)).$$ (3.13)

---

[4]The derivation of this is included in appendix A

Exact solutions to (3.13) are not possible due to the fact that it is still a non-linear equation. However, we adopt an approximate ansatz based on what we know of the system[5]. Considering the important frequencies in the system when it is constrained by $2\omega_J \approx \omega_0$ and is weakly driven gives an ansatz of form,

$$\alpha = \alpha_0 e^{-2i\omega_J t} + \alpha_- e^{-i\omega_J t} + \alpha_+ e^{i\omega_J t}, \tag{3.14}$$

where α_0 and $\alpha_\pm$ are constants to be found. The latter two terms comprise the solution to a linearly driven harmonic oscillator, while the first term comes from frequency up conversion from ω_J to $2\omega_J$ due to the non-linearity.

Substituting this into (3.13) and performing a harmonic balance on the resulting equation leads to,

$$\alpha_0 = -\frac{i\tilde{E}_J \Delta_0^2}{2\hbar} \frac{(\alpha_- + \alpha_+)}{i(\omega_0 - 2\omega_J) + \gamma/2}, \tag{3.15}$$

$$\alpha_- = \frac{\tilde{E}_J \Delta_0}{2\hbar} \frac{(1 - i\Delta_0 \alpha_0)}{i(\omega_0 - \omega_J) + \gamma/2}, \tag{3.16}$$

$$\alpha_+ = -\frac{\tilde{E}_J \Delta_0}{2\hbar} \frac{(1 + i\Delta_0 \alpha_0)}{i(\omega_0 + \omega_J) + \gamma/2}. \tag{3.17}$$

These show that α_0 is completely dependent on α_+ and α_-, suggesting that the process that governs the $2\omega_J$ component is very closely tied to the dynamics of the off resonant terms. Closed form expressions for α that are valid for low $\tilde{E}_J$ and Δ_0 can also be derived.

3.5 Photonic Properties

A sensible starting point for studying the dynamics of the system is to look at the photonic properties of the cavity in the low energy regime. Two key quantities we wish to study are the cavity photon population, $\langle n \rangle = \langle a^\dagger a \rangle$, which will give us information about the rate at which photons are produced in (and leave) the cavity and the first order correlation function, $G^{(1)}(\tau) = \langle a^\dagger(t)a(t+\tau) \rangle$, which contains information about the photon dynamics in the cavity.

Before we can progress with our discussion of the photonic properties, or the properties of any generic operator, we need to consider how to calculate operator expectation values. For the RWA

---

[5]This ansatz can also be calculated using approximate methods such as the method of scales[77] however as the structure of this ansatz stems from fairly obvious physical processes we consider it to be relatively easy to simply guess its structure as long as the problem is only considered within the low energy limit, i.e. $\Delta_0^2 \langle n \rangle \ll 1$.

Hamiltonian, the standard procedure of finding the equation of the operator's expectation value, $\langle \dot{O} \rangle = \text{Tr}[O\dot{\rho}][41]$, can be used. This will give a first order differential equation that may or may not depend on the expectation values of other, possibly composite, operators. Relations for these secondary equations can also be derived in the same way as the principal expectation value equation and then solved sequentially. Once solved, this will give a time dependent relationship and, since we are interested in the steady state relationship the final expression, is taken in the limit $t \to \infty$ which will remove any dependency on initial conditions.

For the semi-classical approach, due to the construction of our solutions, we are limited to finding only the expectation values of operators that can be fully constructed out of the creation and annihilation operators of the cavity after the semi-classical approximation has been applied. Thus, we find that $\langle n \rangle = \langle a^\dagger a \rangle$ is calculable however $G^{(1)}(\tau)$ is not as, as we shall show later.

Using these methods, the expectation values for the cavity occupation can easily be derived. Solving the set of simultaneous differential equations for $H_{\text{eff}}^{(0)}$ gives,

$$\langle \hat{n} \rangle_{RWA} = \left(\frac{\tilde{E}_J^2 \Delta_0^3}{3\hbar^2 \omega_J} \right)^2 \frac{1 + 4\gamma_\varphi/\gamma}{(\gamma/2)^2 \left(1 + 4\gamma_\varphi/\gamma\right)^2 + (\delta')^2}. \tag{3.18}$$

In the case of the semi-classical solution for α, the photon population is found by taking the modulus square of (3.14) and then time averaging the result. This leaves us simply with the stationary components which is just the modulus square of each of α_0, α_-, and α_+ which (working to 4th order in $\tilde{E}_J$ and 6th order in Δ_0 whilst also assuming $\gamma/2 \ll \omega_J$) explicitly gives,

$$|\alpha|^2 = \frac{\tilde{E}_J^2 \Delta_0^2}{2\hbar^2} \left[\frac{\omega_0^2 + \omega_J^2}{(\omega_0 - \omega_J)^2} \right] \left[1 + \frac{\tilde{E}_J^2 \Delta_0^4}{2\hbar^2} \frac{\omega_0^2}{[\omega_0^2 + \omega_J^2][(\omega_0 - 2\omega_J)^2 + \gamma^2/4]} \right]. \tag{3.19}$$

Note that using $2\omega_J \approx \omega_0$ and in the limit of $\gamma_\varphi \ll \gamma$, the second term of (3.19) reduces to (3.18).

Comparison of (3.19) and (3.18) with numerical simulations of (3.2), Fig 3a, shows that we can split the behaviour of the photon population into three distinct regimes. In the first regime, at very low Josephson energies, the occupation grows with $\tilde{E}_J^2$. In this regime the dynamics are dominated by processes at ω_J and the RWA fails to capture the dynamics. In the second regime, the occupation number begins to grow with $\tilde{E}_J^4$ and the RWA becomes a good description of the system. In this case, the system's dynamics are dominated by processes oscillating at $2\omega_J$. Past this regime, the occupation number starts to saturate. Fig 3.3 a. also shows a numerical solution

using (3.8) which, like the low energy RWA (3.11), fails in the limit of low energy. However, (3.8) does accurately describe the system into the saturation regime.

The spectrum of the radiation leaving the cavity may also provide some insight into the contrast between the two Cooper Pair resonance and the single Cooper pair tunnelling case. To get information about this we study the first order correlation function, $G^{(1)}(\tau) = \langle a^\dagger(t)a(t+\tau)\rangle$, which is found using the same equations of motion that define (3.18) and then using the regression theorem[61] to replace them with the corresponding two time correlation functions. Doing this, it can be shown that the solution in the long time limit,

$$\langle a^\dagger a(\tau)\rangle = \langle n\rangle e^{-2\gamma_\varphi \tau},\tag{3.20}$$

which is interesting as it indicates a line width four times greater then that of the single Cooper-pair resonance[29]. This is due to the fact that it is necessary to use the junction phase commutation relationship twice to fully simplify the master equation when calculating the original equation of motion before application of the regression theorem. Note that, despite $G^{(1)}(\tau)$ being constructed
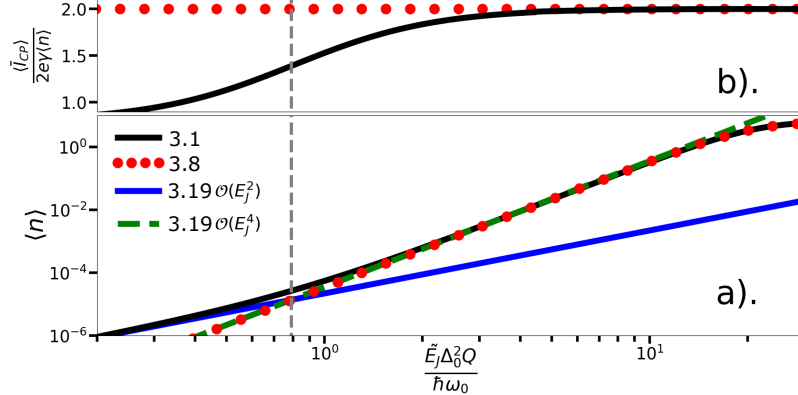
Figure 3.3: a). Comparisons of the cavity population predictions for the RWA, $\langle n\rangle_{RWA}$ using the RWA Hamiltonian (3.8), the $\mathcal{O}(\tilde{E}_J^2)$ and $\mathcal{O}(\tilde{E}_J^4)$ components of the semi-classical approximation, $|\alpha|^2$, and a time averaged numerical integration of the full Hamiltonian (3.1). Both of the Hamiltonians were propagated using the master equation, (3.2)
. The dashed grey line shows the point of cross over of dominance from single Cooper pair tunnelling processes to two Cooper pair tunnelling processes. b). Comparisons of the current-photon population ratio calculated from the RWA Hamiltonian (red dots) and the full Hamiltonian (black line). For the data shown, the specific parameters used were $\Delta_0 = 0.15$, $Q = 1500$, $\gamma_\varphi = 0$, and $\omega_J/\omega_0 = 0.5$.

entirely of functions of α, the semi-classical approximation doesn't allow us to calculate its dynamics because γ_φ is neglected in this approach.

3.6 Charge Transport Properties

Due to the relations assumed in the initial formulation of the RWA Hamiltonian (equation (3.8)), we expect there to be a very close relationship between the charge dynamics flowing through the junction and the photonic population of the cavity (i.e. two Cooper pairs tunnel for each photon produced) in this picture. However, as we have shown that the system is not dominated by a single frequency in all regimes, it is important to ask what charge transport mechanism dominates in regimes where the RWA doesn't hold.

For this, we chose to study two different measures of charge dynamics. Firstly, the average current flowing through the junction, expressed in terms of the cavity operators, which tells us about the relationship between the Cooper pairs tunnelling and the photons produced. Secondly, we will examine the noise in the current and photon transport, which will tell us about the coherence of the tunnelling process and the distribution of the cavity photons.

3.6.1 Current Dynamics

The current flowing through the junction can be defined simply as the amount of charge moving through the junction per unit time, $\langle I_{CP} \rangle = 2e\langle \dot{N} \rangle$[6]. Because dissipative processes in the master equation cannot contribute to charge transfer, we can identify the current operator from the coherent dynamics of the charge operator,

$$I_{CP} = \frac{2ei}{\hbar}[H(t), N] = \frac{2eE_J}{\hbar}\sin(\omega_J t - \varphi + \Delta_0(a^\dagger + a)),$$ (3.21)

and using the effective Hamiltonian leads to an approximate expression for the average current,

$$\overline{I_{CP}}/2e = \frac{i}{\hbar}[H_{eff}, N] = \frac{2i}{\hbar}[H_{eff}, n].$$ (3.22)

---

[6]This expression of the current relationship is quite different to ones used in other superconducting circuitry literature, particularly those that focus on similar circuits that use SQUIDS as the nonlinear elements. The main reason for this difference is in circuit makeup. Most SQUID circuits have multiple junctions and are controlled by an applied flux, as apposed to our single embedded junction controlled by an applied voltage. This particular current expression has been used extensively in the literature surrounding voltage biased JJ circuits[28].

A semi-classical expression for the current can be derived by considering (3.21) in the semi-classical limit. Doing this and substituting in our ansatz solution will give the full time dependent solution in the low energy limit. Only considering time independent terms gives,

$$\overline{I_{CP}}/2e = \frac{E_J}{\hbar}\overline{\sin(\omega_J t + \Delta_0(\alpha^* + \alpha))}, \tag{3.23}$$

which describes the time averaged behaviour of the current flow and can be compared to (3.22). Again, working to order $\tilde{E}_J^{\ 4}$ (and Δ_0^6) leads to the simple relationship $\overline{I_{CP}}/2e = \gamma(|\alpha_0|^2 + |\alpha_+|^2 - |\alpha_-|^2)$.

The value of the average current itself is not overly enlightening, however, the ratio of the rate at which Cooper pairs tunneling, $\Gamma_{CP} = \langle\overline{I_{CP}}\rangle/2e$, and the average rate at which photons leave the cavity, $\Gamma_{Ph} = \gamma\langle n \rangle$ can give more insight. The RWA predicts that $\Gamma_{CP}/\Gamma_{Ph} = 2$ which implies that two Cooper pairs tunnel for each photon produced, as in the approximations made to define H_{eff} all other frequencies apart from $2\omega_J$ are neglected.

Comparisons to numerical time averaged integration's using (3.2) and (3.21), Fig 3.3b, show that, for values of $\tilde{E}_J$ which are not too small, where the RWA has been shown to be a good fit, the ratio does tend very close to 2. This is in line with the dominant semi-classical component being that associated with the $2\omega_J$ frequency, and suggests that almost all charge transport is pairs of Cooper pairs tunnelling together.

The semi-classical approach can be used to explore what happens off resonance or as the drive approaches zero. In this case the ratio begins to drop dramatically, approaching the limit $\lim_{E_J\to 0}(\Gamma_{CP}/\Gamma_{Ph}) = 0.8$. This behaviour is explained by considering the semi-classical ratio in the vanishing $\tilde{E}_J$ limit where α_0 (and hence double Cooper pair tunneling) can be disregarded. In this limit the ratio becomes,

$$\Gamma_{CP}/\Gamma_{Ph} = \frac{|\alpha_+|^2 - |\alpha_-|^2}{|\alpha_+|^2 + |\alpha_-|^2} = 0.8|_{\omega_J/\omega_0=0.5}, \tag{3.24}$$

which is independent of all parameters apart from the system frequency. The behaviour of this ratio across a range of frequencies is shown in Fig 3.4. This implies that all double Cooper pair tunneling is restricted to a sharp resonance around $\omega_J = \frac{\omega_0}{2}$ as expected.

3.6.2 Current and Photon Noise

Next, we chose to examine the noise that is present in the dynamics of the system. We will use dimensionless measures, known as Fano factors, to quantify the noise in the current, F_{CP}, and the cavity occupation, F_n.

First, let's consider the current Fano factor. We define the current Fano factor as,

$$F_{CP} = \frac{\overline{S_{CP}}}{(2e\langle I_{CP}\rangle)}, \tag{3.25}$$

where $\overline{S_{CP}}$ is the un-normalised time averaged current noise. $S_{CP}(t)$ is the time dependent current noise which we define as,

$$S_{CP} = 2Re \int_0^\infty d\tau [\langle I_{CP}(t+\tau)I_{CP}(t)\rangle - \langle I_{CP}(t+\tau)\rangle\langle I_{CP}(t)\rangle], \tag{3.26}$$

and the time averaged noise is given by averaging over a full period $T \ll 1/\omega_J$,

$$\bar{S}_{CP} = \frac{1}{T} \int_{t_0}^{t_0+T} S_{CP}(t)dt, \tag{3.27}$$

where t_0 is a time much longer than the system's characteristic time scales. The actual interpreta-
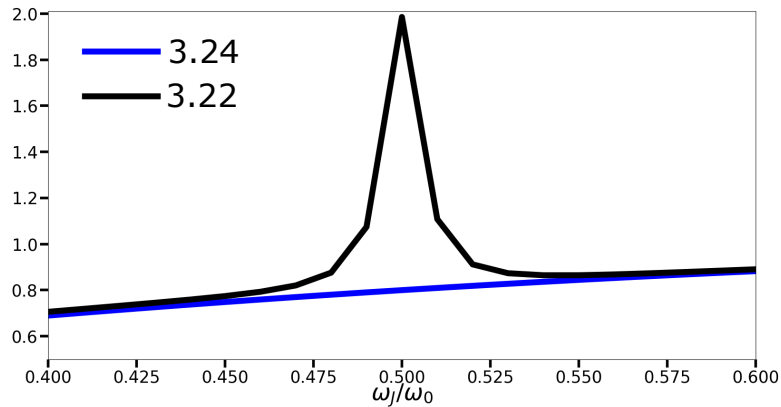

Figure 3.4: Comparison of the predictions for the current-photon ratio by direct numerical integration of the master equation (3.22) and the contribution of the single Cooper pair tunnelling processes as (3.24) the system is brought off resonance. For the data shown the specific parameters used were $\Delta_0 = 0.15$, $Q = 1500$, $\gamma_\varphi = 0$, and $\tilde{E}_J/\hbar\omega_0 = 0.8$.
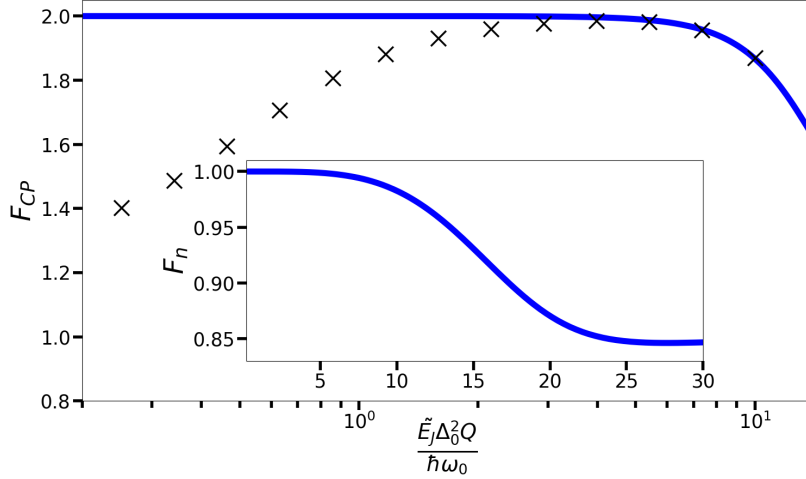
Figure 3.5: Comparisons of the Cooper pair current Fano factor, F_{CP} when calculated using the RWA Hamiltonian, blue line, and by direct integration of the master equation, black crosses, as a function of $\tilde{E}_J$. For the data shown the specific parameters used were $\Delta_0 = 0.15$, $Q = 1500$, $\gamma_\varphi = 0$, and $\omega_J/\omega_0 = 0.5$.

tion of these correlation functions is not trivial, but they can be shown to be defined as[61],

$$\langle I_{CP}(t+\tau)I_{CP}(t)\rangle = Tr[I_{CP}(t+\tau)e^{\mathcal{L}\tau}I_{CP}(t)\rho_{ss}(t)], \tag{3.28}$$

where $\rho_{ss}(t)$ is a steady state density matrix of the system (i.e. in the limit of long times) and $\mathcal{L}$ is the Liouvillian super-operator for the system.

We can also consider the photon population Fano factor, equation 2.7. Recall that, a photonic Fano factor with value $F_n < 1$ indicates that the number state distribution in the cavity mode is in a number squeezed state, a sub-Poissonian number state distribution.

Comparisons of numerical calculations of F_{CP}, Fig 3.5, for $H(t)$ and H_{eff} show that the noise dynamics can be separated into distinct driving regimes. In the very low driving regime, the RWA calculation simply predicts that $F_{CP}^{RWA} = 2$, which describes incoherent tunnelling of two Cooper pairs (i.e. charge $4e$)[80]. However, when we examine the non-RWA F_{CP} in this regime we find it is significantly below 2. This is due to the fact that at small energy scales, incoherent tunnelling of single Cooper pairs becomes a much larger contributor to the overall dynamics of the Cooper pair current flow. This means that the average number of Cooper pairs that tunnel per photon created in the cavity begins to drop as shown in Fig 3.5. The RWA is incapable of displaying this behaviour, as we have assumed that only double Cooper pair processes are included in the

approximate Hamiltonian, hence the discrepancy in F_{CP} measurements at low energy. As $\tilde{E}_J$ is increased, we find the non-RWA calculation unifies with the RWA calculation at $F_{CP} \approx 2$ due to the increasing domination of the two Cooper pair process.

At larger values of $\tilde{E}_J$, F_{CP} begins to drop below 2, despite the two Cooper pair process still dominating in this regime. This is explained by the process behind the tunnelling changing as the photon population of the cavity increases. As $\langle n \rangle$ approaches much higher values the system begins to experience back-action into the junction from the cavity, this in turn promotes coherent current flow through the junction at the largest values of $\tilde{E}_J$ shown in Fig 3.5. Note that the cavity's state effects the junction in our model due to the inclusion of the cavity position operator $a^\dagger + a$ in the drive term.

This is supported by the calculation of F_n which also drops below unity in this regime, showing that the photons are anti-bunched. This also shows that the system has moved to a sub-Poissonian distribution which is associated with the cavity state now being a squeezed state rather than a coherent state which is what occurs in the regime of weak driving (i.e. under (3.11)).

3.7 Use as a Single Photon Source

So far we have focused on the description of the system's dynamics and the processes that drive them. Now we turn to the potential application of the system. As was shown in the previous sections, the system undergoes photon anti-bunching due to the effects of the non-linearity in the Hamiltonian. In the following, we show that, under the right conditions, the anti-bunching can become so strong that the system could function as a single photon source.

For this to occur, there must be a point in parameter space where it is impossible for the system to produce two photons in the cavity at once. When this occurs, the system will be trapped in the lowest two Fock states, making it into an effective two-level system. For this to occur, interference effects in the cavity must force the matrix element $h_{12} = \frac{\hbar\omega_0}{\tilde{E}_J^2} \langle 1| H |2 \rangle = 0$. Note that the damping in the system can always decrease the number of photons in the cavity, however, our initial assumption of zero temperature doesn't allow thermal excitation from the environment.

Analytically it is not possible to show that $h_{12} = \frac{\hbar\omega_0}{\tilde{E}_J^2} \langle 1| H |2 \rangle = 0$ using (3.1) however, we can use H_{eff} as a starting point to determine where this effect should occur in parameter space. Once this has been determined, its validity can be checked against the full numerical integration.

We begin by writing (3.8) in the Fock basis. This gives,

$$
H_{eff} = \sum_{m=0}^{\infty} \hbar\delta'm\,|m\rangle\langle m| + \frac{\tilde{E_J}^2}{4\hbar\omega_J} \sum_{q=0}^{\infty}\sum_{m=0}^{\infty} \frac{1}{(2q+1)}(|f(q,m)|^2
$$

$$
+|g(q,m)|^2)(|m+q\rangle\langle m+q| - |m\rangle\langle m|)
$$

$$
+\frac{\tilde{E_J}^2}{4\hbar\omega_J}\sum_{q=0}^{\infty}\sum_{m=0}^{\infty}\frac{1}{(2q+1)}(f(q,m)g^*(q,m)\,|m+q\rangle\langle m+q+1|
$$

$$
-f(q,m+1)g^*(q,m)\,|m\rangle\langle m+1|)
$$

$$
+\frac{\tilde{E_J}^2}{4\hbar\omega_J}\sum_{q=0}^{\infty}\sum_{m=0}^{\infty}\frac{1}{(2q+1)}(f^*(q,m)g(q,m)\,|m+q+1\rangle\langle m+q|
$$

$$
-f^*(q,m+1)g(q,m)\,|m+1\rangle\langle m|), \tag{3.29}
$$

where,

$$
f(q,m) = i^q \frac{\sqrt{m!}}{\sqrt{m+q!}}\Delta_0^q L_m^q(\Delta_0^2),
$$

$$
g(q,m) = (-i)^{q+1} \frac{\sqrt{m!}}{\sqrt{m+q+1!}}\Delta_0^{q+1} L_m^{q+1}(\Delta_0^2),
$$

in which L_m^q is an associated Laguerre polynomial[69]. From this it is possible to simply pick out

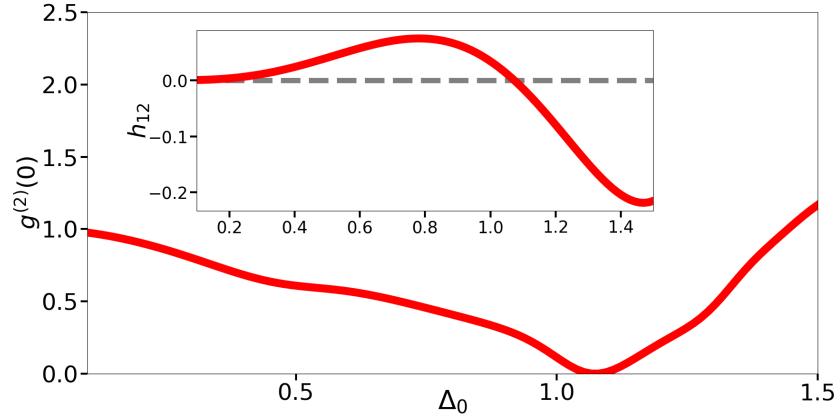
Figure 3.6: The second order photon correlation function for the RWA Hamiltonian as a function of Δ_0. Inset: The h_{12} element for the RWA Hamiltonian, it vanishes at the same point as the the second order photon correlation function. For the data shown the specific parameters used were $Q = 500$, $\gamma_\varphi = 0$, $\omega_J/\omega_0 = 0.5$, and $\tilde{E_J}/\hbar\omega_0 = 0.1$

the appropriate matrix element and normalise it to give,

$$h_{12} = \frac{1}{4} \left(\left(\frac{\Delta_0}{\sqrt{2}} L_1^0(\Delta_0^2) L_1^1(\Delta_0^2) \right) - \left(\frac{\Delta_0^3}{3\sqrt{2}} L_0^1(\Delta_0^2) L_0^2(\Delta_0^2) \right) + \sum_{q=0}^{\infty} \frac{(-1)^q \sqrt{2} \Delta_0^{2q+1}}{(2q+1)(q+2)!} L_1^{q+1}(\Delta_0^2) L_2^q(\Delta_0^2) \right).$$

(3.30)

This can be solved numerically which reveals that the matrix element disappears at $\Delta_0 = 1.07474$.

To measure the extent to which the system acts as a single photon source, we define the normalised second order correlation function $g^{(2)}(0)$ introduced in chapter 2. Recall that this take the form,

$$g^{(2)}(0) = \frac{\langle a^\dagger a^\dagger a a \rangle}{\langle a^\dagger a \rangle^2}.$$

(3.31)

$g^{(2)}(0) = 1$ indicates a photon number distribution within the cavity which has a Possonian distribution and $g^{(2)}(0) < 1$ indicates a system with anti-bunched emission. $g^{(2)}(0) = 0$ would indicate a system with no possibility of simultaneous photon emission[81].

Numerical calculations of $g^{(2)}(0)$, Fig 3.6, show that it does indeed vanish at $\Delta_0 = 1.07474$ when using H_{eff}, indicating that the system does enter a two-state regime. This value of Δ_0 is considerably lower than previously predicted for similar systems, with the single Cooper pair resonances predicting a similar effect at $\Delta_0 = \sqrt{2}$[14] and is very close to experimentally realisable values[36].

The vanishing of $g^{(2)}(0)$ is notably harder to see in a non-RWA calculation without careful selection of parameters. This is due to the fact that the strong photon anti-bunching effect is derived from interference effects, causing the h_{12} element to vanish. However, this is an effect that only involves the two Cooper pair tunnelling processes, and introduction of the single Cooper pair process destroys this interference pattern. Thus, to see this strong suppression of $g^{(2)}(0)$ with the non-RWA Hamiltonian one needs to choose a parameter other than Δ_0 to push the system into a regime of suppressed single Cooper pair tunnelling[7].

The semi-classical dynamics gives clues about how to do this. By examining the ratio of α_0 to $\alpha_+ + \alpha_-$, there are two possible ways to suppress α_+ and α_-; by increasing Q or increasing $\tilde{E}_J$. Increasing $\tilde{E}_J$ is not desirable as for large $\tilde{E}_J$ the RWA eventually breaks down. Increasing Q, however, is effective. As long as the system is at an appropriate $\tilde{E}_J$ for which H_{eff}^0 (equation

---

[7]Note that equation (3.31) is not inherently a time averaged quantity when calculated using the results from numerical interrogations of equation (3.1). Because of this, time averaging similar to that used when calculating $\langle n \rangle$, i.e. allowing the integration to reach the long time limit and then taking an average over a large number of whole periods, needs to be employed to get an accurate result.
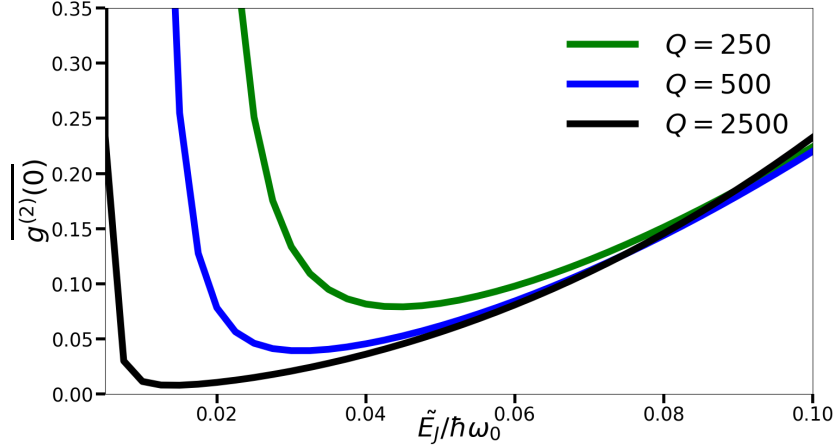
Figure 3.7: The second order time averaged photon correlation function as a function of $\tilde{E}_J$ showing that the minima tends towards zero as Q is increased and the single Cooper pair process is suppressed. For the data shown the specific parameters used were $\gamma_\varphi = 0$, $\omega_J/\omega_0 = 0.5$, and $\Delta_0 = 1.07474$. This was calculated by applying equation (3.31) to a time averaged integration of equation (3.1).

(3.11)) is a valid approximation, a very low, but non-zero $g^{(2)}(0)$ can be achieved. Fig 3.7 shows that lower $g^{(2)}(0)$ can be achieved by increasing Q.

What is notable about this system, and other similar systems[14] is that they are able to display these highly quantum behaviours independent of the initial quantum state that the system is started in. This is due to the dissipation present in the system causing the cavity to always approach its steady state independent of the initial conditions. Similar results to those presented here have been shown in other JJ-Cavity systems, in the form of DC SQUIDS, by Everitt et. al.[82] however in a significantly different context. The system studied by Everitt et. al. deviated from ours several ways: it is a tripartide system with two cavity modes that have cross interaction terms, and the evolution of the system is fully coherent with no dissipation. Because of the lack of dissipation, it was found that one of the cavities could be locked into a subset of Fock states consisting of $|0\rangle$ and $|1\rangle$, and thus have a $g^{(2)}(0) = 0$, if the system was initially prepared in a very specific quantum state. It is interesting to contrast these two systems as, while very different in set up and mechanics, both display long time behaviours locked to the same subset of quantum states.

3.8 Conclusions

In conclusion, we have considered a JJ-cavity system, tuned so that when two Cooper pairs tunnel through the junction a single photon is produced. We described a method for moving the time dependent Hamiltonian into a rotating frame and then performing a second order rotating wave approximation, resulting in a simpler time independent effective Hamiltonian. We then demonstrated two methods for solving for the system dynamics in the low energy regime, the low energy effective (RWA) Hamiltonian and the semi-classical approximation.

We derived expressions for the cavity photon population and showed that the behaviour of the system could be separated into three distinct regimes: The very weak driving regime where the RWA fails due to the frame rotating at the wrong frequency and the semi-classical description proves accurate, the intermediate driving regime where the system oscillates at $2\omega_J$ and the RWA is valid, and a large driving where the photon occupation number of the system saturates.

The charge dynamics showed that in the regimes where the RWA was valid, our assumption that $2\omega_J \approx \omega_0$ corresponded to a regime dominated by two Cooper pair process was indeed correct, however at very low E_J processes involving only single Cooper pairs began to dominate. It was also shown that the double Cooper pair tunnelling process could become coherent and that the system underwent photon anti-bunching.

Finally, we examined the system as a source of single photons. The conditions under which this could occur were derived and then explored numerically and analytically. It was shown that this point in parameter space, not only occurred at a much smaller value of Δ_0 than previously found for similar systems, but very close to experimentally realised values.

The work presented above has left many unanswered questions that we have not yet had the opportunity to explore. While the RWA has been presented here in full, we have neglected to explore the breakdown of this approximation that occurs in the regime of larger $\tilde{E}_J$. Additionally, we neglected to try and explain the behaviour of the current noise as the system approached zero drive.

Chapter 4

Dynamics of a Josephson Junction Laser in the Many Mode Limit

4.1 Introduction

In Chapter 2 we have detailed the uses of JJ driven cavity systems extensively, particularly those engineered with multiple coexisting modes. One such use for these systems is the Josephson junction laser, where a JJ driven cavity is able to produce highly coherent light for use in on chip devices. Demonstration of such a device was first done by Cassidy et al.[31] who constructed a JJ laser which not only demonstrated a strong lasing behaviour, but was also shown to be a potential quantum limited amplifier. The theory relevant to this experiment was largely developed by Simon and Cooper[32] who moved from Cassidy et al.'s description of the system via a set of coupled differential equations to a more collective description of the system. Simon and Cooper used a perturbative approach to analyse the periodic behaviour at the drive frequency (set by the voltage) whilst also showing that at solution with period set by the fundamental mode can also exist (see Chapter 2). However, they did not examine the transition between these two regimes.

In this chapter, we wish to further expand on Simon and Cooper's and Cassidy et al.'s descriptions of the JJ laser system and describe the system's dynamics as a function of the drive strength. From this we hope to give a detailed description of how the system moves from low energy approximations derived by Simon and Cooper to their general description of the sawtooth solution with

period set by the fundamental mode. We focus on cases where a very large number of modes is involved and find the drive almost always appears to set the periods of the oscillation for a long time. Note that we will consider the case of small N in Chapter 5.

The rest of this chapter is organised as follows. In section 4.2 we discuss the system's many parameters and describe the simplifications we will make that allow us to concentrate on the most important aspects of the problem. In section 4.3 we detail the perturbation approximation to the Volterra equation of motion for the system (introduced in Chapter 2) and show that for weak drives, the system is locked to the drive frequency. In section 4.4 we will detail strongly nonlinear transient dynamics that emerges as the strength of the drive is increased. In section 4.5 we detail the emergence of sudden, aperiodic resets in this transient behaviour that we call phase glides, and explore how these develop as the drive is further increased. In section 4.6 we look briefly at a regime of extremely strong driving where aperiodic behaviour seems to emerge. Section 4.7 provides a summary of our findings and contrasts them with Simon and Cooper's results to try and determine if they are compatible or not. Finally, in Section 4.8 we will discuss the conclusions we have drawn from our analysis.

4.2   Dynamics as a Function of the System Parameters

The Josephson laser is described by equation (2.12), which we reproduce here for convenience,

$$\ddot{\psi}_n = -\omega_n^2 \psi_n - 2\gamma\dot{\psi}_n + \alpha_n\lambda\sin(Vt + \sum_k \alpha_k\psi_k).$$

In the following sections we will explore the dynamics of the system specifically as the drive strength λ is varied, however there are many other parameters in (2.12) that warrant a brief discussion about how we will treat them.

Firstly, let's consider α_n. As mentioned in Chapter 2, α_n is a geometric factor that determines how each mode couples to all the others. The main effect of changing α_n is a change in the shape of the kernel $K(t)$ (see equation (2.18))[1]. We will focus on the simplest case where the system is fully symmetric and thus $\alpha_n = 1$ for all n.

Secondly, we must consider the voltage across the junction, V. Like Simon and Cooper, we are

---

[1]The changes in the shape of this function and its relative effect on the system is described in detail in the Supplemental Material of Simon and Cooper[32], but for the most part it has very little effect.

principally interested in the case where this voltage is an integer multiple of the system's lowest natural frequency. This is so that we have resonantly driven modes. As for the specific choice of V, we choose $V = 2\omega_1$ as this is the lowest value of integer V that doesn't directly excite all the modes (including the fundamental). That is not to say that we expect very different results for other integer values of the voltage, only that we haven't explicitly explored them.

Thirdly, the number of modes N. As we discussed previously, in this chapter we are explicitly interested in the case of many modes[2], which in this case is defined as the limit where adding more modes to the system has no appreciable effects on the dynamics. For the integrations we present here, this was determined to be $N = 300$ or more, any fewer, and it was found to change the system's dynamics dramatically.

Fourthly, the choice of ω_n, or more specifically the spacing of the ω_n sequence. For this, we chose simply for all higher order frequencies to be an integer multiple of the lowest cavity mode, $\omega_n = \omega_1 n$. This is in line with the work done by Simon and Cooper[32] and will allow for every other mode to be resonantly driven for the chosen voltage of $V = 2\omega_1$.

Finally, we should address the loss in the system, described by the rate γ. For the most part, decreasing the loss that the modes experience only had two effects. Firstly, it increases the time the system takes to settle into its long time limit behaviour. Secondly, it tends to reduce the values of λ at which aspects of the dynamics begin to change. However, the order in which these changes occur remains the same as long as the condition that the system is under damped $\gamma \ll 1$ is preserved.

We note that we explore a much wider range of parameters in the next chapter using a much smaller value of N, as in this regime the calculations are much faster.

4.3 The Dynamics Under Weak Drive

We start by considering the dynamics of the system under weak drive. In this case, analytic solutions can be developed using a perturbation method developed in terms of λ[32].

---

[2]For the case of few modes please see Chapter 5.

4.3.1 First order perturbation theory

The lowest order approximation to $\Psi(t)$ is first order in λ. In this case, we can drop the non-linear element in the right-hand side of (2.16) and find,

$$\Psi(t) = \lambda \int_{-\infty}^{t} dt' K(t - t') \sin(Vt'). \tag{4.1}$$

This equation is exactly solvable. Solving it via integration by parts[3] and recalling that T is the period of the fundamental mode, leads to an expression for the lowest order approximation,

$$\Psi(t) = \frac{\lambda T}{4(\gamma^2 + V^2)} \left(1 + 2\frac{e^{-\gamma T}}{1 - e^{-\gamma T}}\right)(\gamma \sin(Vt) - V \cos(Vt))$$

$$+ \frac{\lambda}{2(\gamma^2 + V^2)^2 + 8v^2\gamma^2} \left((\gamma^2 + V^2)\sin(Vt) + 2\gamma V \cos(Vt)\right), \tag{4.2}$$

which is periodic, with period $2\pi/V$. This is the linear limit: the only oscillations that develop are at the same frequency as the drive, V.

While equation (4.2) is a full equation that will work as long as any of the original approximation conditions are met, we can make it much more useful by imposing an additional limit, that of weak loss $\gamma \ll V$. In this limit we ignore terms that are proportional to γ and (4.2) can reduce to,

$$\Psi^{(0)}_{\gamma \ll 1}(t) = -\frac{\lambda T}{4V}\left(1 + 2\frac{e^{-\gamma T}}{1 - e^{-\gamma T}}\right)\cos(Vt) + \frac{\lambda}{2V^2}\sin(Vt). \tag{4.3}$$

In this case we can see that the second term will be much smaller than the first, being an order of magnitude smaller, and can be ignored giving a compact equation of the form,

$$\Psi^{(0)}_{\gamma \ll 1}(t) = -A\cos(Vt) \tag{4.4}$$

where $A = \frac{\lambda T}{4V}\left(1 + 2\frac{e^{-\gamma T}}{1 - e^{-\gamma T}}\right)$. We will assume the condition $\gamma \ll V$ that will apply to all further calculations.

---

[3]See Appendix 3 for the full method

4.3.2 Second Order Perturbation Theory

The lowest order result only tells us about the response at the drive frequency. To see which other harmonics occur, we need to go further.

Let us consider the first order solution to be the form of equation (4.4). We have dropped the sine term from the original solution, as it is far smaller than the other terms. To generate higher order corrections we substitute equation (4.4) into (2.16) and find,

$$\Psi(t) = \lambda \int_{-\infty}^{t} dt' K(t - t') \sin(Vt' - A\cos(Vt')). \tag{4.5}$$

Again this can be solved by integration by parts, but the calculation is significantly more involved[4]. This gives a final expression for the second order approximation as,

$$\Psi(t) = \Psi^{(1)}(t) - \frac{A\lambda\pi^2}{12\omega_0^2} + \frac{\lambda AT}{16V}\left(1 - 2\frac{e^{-\gamma nT}}{1 - e^{-\gamma nT}}\right)\sin(2Vt) - \frac{A\lambda}{16V}\cos(2Vt). \tag{4.6}$$

Here, again, the cosine term can be neglected due to the fact that it is a far smaller than all other relevant terms.

This is the full second order perturbative approximation in the limit of weak drive. It contains first and second order terms at the drive frequency (V), as well as second order terms at twice the frequency ($2V$). This implies that as the drive increases in strength, the mode with frequency $2V$ will begin to become resonantly excited. As more modes get resonantly excited by the drive, the 'Fourier mixer' generated by the system's nonlinearity gets increasingly complex.

To see how valid these approximations are, we compare them to the numerical integration of (2.12) with many available modes. Allowing the system to have access to many modes even when we do not expect them to make any contribution to the overall dynamics ensures that the truncation of the system does not interfere with the calculation.

Three cases of this integration are shown in Fig 4.1: a low drive, a borderline strength drive, and a drive beyond the scope of the approximation in its current form. In Fig 4.1 (a) the system is well within the weak drive limit, $\lambda = 0.05$, and the system's response is sinusoidal, implying that only one mode, that of the drive frequency, is excited. This is corroborated by the close agreement of the first and second order approximations (whose other components are vanishing

---

[4]Again this full method is detailed in Appendix 3
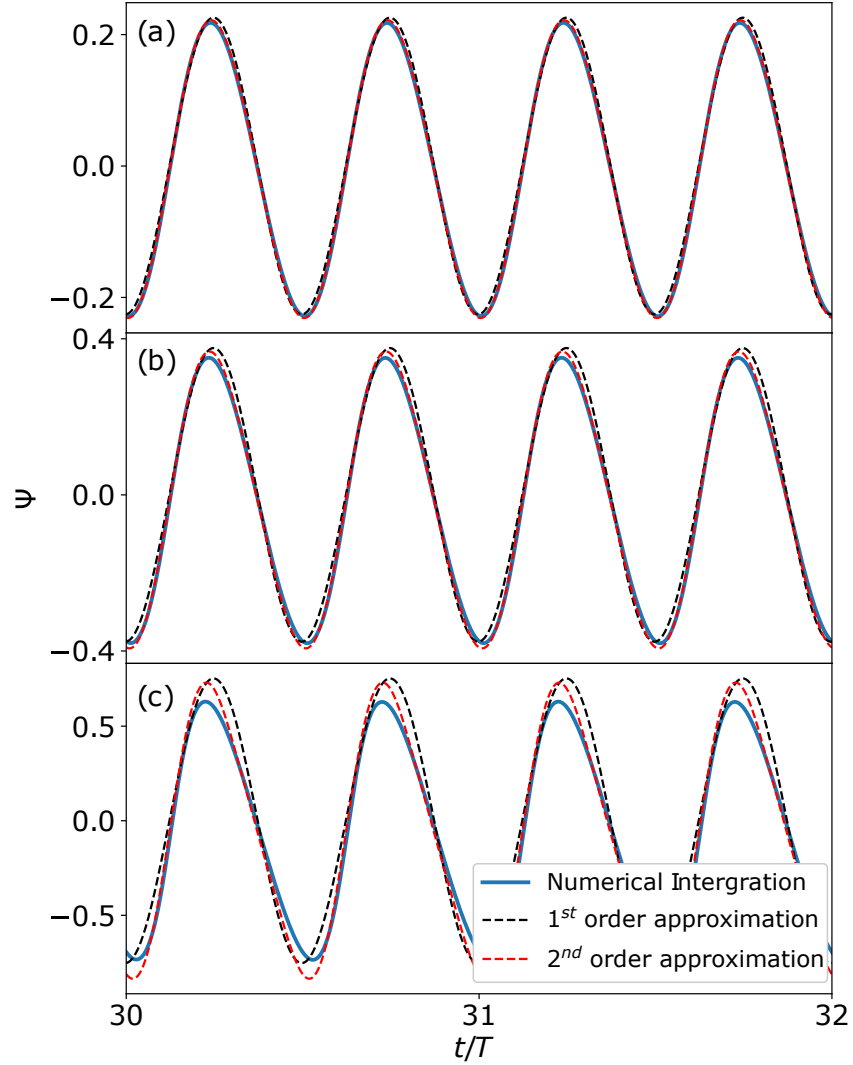
Figure 4.1: Numerical integrations of equation (4.3) compared with first and second order approximate calculations (equations (D.12) and (D.37)), with $\lambda = 0.03$ (a), $\lambda = 0.05$ (b), and $\lambda = 0.1$ (c). In (a) the perturbative approach works well, in (b) the second order equation works performs best, and in (c) both have broken down. In all calculations $\gamma = 1/30$, $V = 2$, and $N = 300$. Note that we adopt units such that $\omega_0 = 1$ unless otherwise stated in this chapter.

small in this parameter range). In Fig 4.1 (b) we have moved from the regime where the system
is only exhibiting one frequency and is now beginning to involve other frequencies. In this case,
we see that the first order approximation has begun to move away from the true value, indicating
that the approximation is breaking down. But the second order approximation is still quite close to
the true line, indicating that the higher order approximation is still working relatively well in this
regime. In Fig 4.1 (c) we have moved past the regime where the second order approximation is a
good fit. The system is exhibiting more and more frequencies which will turn out to be an integer
multiple of the drive.

As the drive is increased progressively, the system slowly begins to move toward solutions that
resonantly excite more and more modes. While our second order approximation does begin to break
down in the parameter regime depicted in Fig 4.1 (c), that is not to say that this approximation
method is invalid. In fact, we could carry on, working to higher and higher order perturbations and
it is clear from the general form of the equations that these solutions can only contain frequencies
of an integer multiple of the drive frequency. In fact, we believe that there should be a predictable
pattern to these that could lead to an infinite sum, however beyond the second order this calculation
becomes increasingly difficult and we chose not to pursue this further. We call the range of λ values
where the second order analytical perturbative approximation proves accurate the analytical regime.

4.4   Total and Relative phase glides

In this section, we explore the complex behaviour that emerges at stronger coupling. After the
analytical regime, we move to one that we will call the no slip regime. In the no slip regime, the
drive strength is strong enough such that the nonlinearity begins to have a strong influence on the
system and analytical descriptions break down. This regime shows a strong sawtooth behaviour,
but the system is still locked to the drive frequency. This regime is principally defined by the
fact that the sawtooth behaviour is so well established. In the analytical regime, the system is
very much still just a sum of a few sinusoids and looks as such. However, in the no slip regime
that follows a large number of components with frequencies nV are generated (n being an integer)
leading to a sawtooth with period $2\pi/V$, though it can take a very long time to reach this state.

To understand what happens as the drive is increased, it is helpful to consider the spacing
between vertical jumps in a sawtooth in terms of a phase, $\Delta\phi$. The phase separation of the sawtooth

is defined using the time between two adjacent jumps in the solution relative to the period of the
lowest mode,

$$\Delta\phi = 2\pi \frac{t_{\text{jump 1}} - t_{\text{jump 2}}}{T}. \tag{4.7}$$

This measure gives us information about the frequencies present in the system. If the system is
locked to a drive frequency $V = 2\omega_0$ (which we will assume from now on) then $\Delta\phi = \pi$, i.e. we
have two jumps per period, equidistant apart, and the jumps are spaced by $T/2$ (see Fig 4.3 (b)).
If the system has $\Delta\phi \neq \pi$ then the system has a periodicity of T and the dominant frequencies are
no longer just even but are all integer multiples of the natural frequency (see Fig 4.3 (a)).

The transition between period $T\frac{\omega_0}{V}$ and period T behaviour that occurs as λ is increased is
complex, leading to very slow dynamical effects when N is large. We find that the system can
exhibit a long interval of period T oscillations followed by a transitional period and then stable
oscillations locked at the drive frequency. This behaviour is shown in detail in Fig 4.2 with the
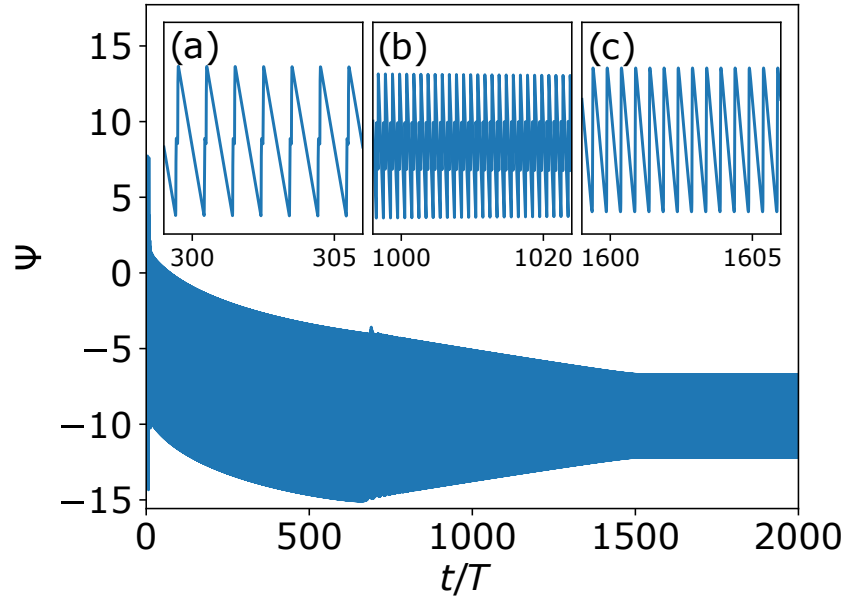
Figure 4.2: Main Figure: An example integration of Ψ with a drive strong enough to exhibit the
phase glide dynamics, $\lambda = 5.8$. (a), The Ψ integration while the system is undergoing a total phase
glide, the wave has a phase separation $\Delta\phi \neq \pi$ which only slowly moves relative to each other.
However, this is a lot of movement relative to the phase of the drive leading to a downward trending
average position. (b) The Ψ integration while the system is undergoing a relative phase glide, with
the relative phase separation tending towards $\Delta\phi = \pi$. (c), The Ψ integration while the system
which is now locked to the drive frequency with a constant phase separation of $\Delta\phi = \pi$. For these
integrations $\gamma = 1/30$, $V = 2$, and $N = 300$.

insets showing the behaviour of the sawtooth jumps in each stage of the dynamics. The very long

settling period (up to $t/T \approx 650$ in Fig 4.3) is characterised by three main features: The dominance

of a double sawtooth with $\Delta\phi \neq \pi$ a constant off set that appears to be continuously decreasing,

and a sensitivity to initial conditions that determines $\Delta\phi$ in a complex way. The transitional period

(up to $650 \leq t/T \leq 1500$ in Fig 4.3)is characterised by having an offset that is now constant but

a phase separation that is now moving, approaching $\Delta\phi = \pi$. When the system reaches $\Delta\phi = \pi$,

any further evolution ceases and the system settles into its long time limit behaviour.

The moving offset in the double sawtooth behaviour can be attributed to a total phase glide

within each period. As the system evolves in time, the phase positions of the two sawtooth jumps

moves forward in the period. Their relative position to each other remains fairly consistent, but in

each period they happen slightly later. This is shown in detail in the first sections of Fig 4.3(a) and

(b). In this case, we have taken a time window consisting of integer multiples of the drive period of

the integration and extracted the average amplitude of the component oscillating at ω_1, $|c_1|^2$. If c_1

is non-zero then the system is locked to the natural frequency and all available modes are excited.
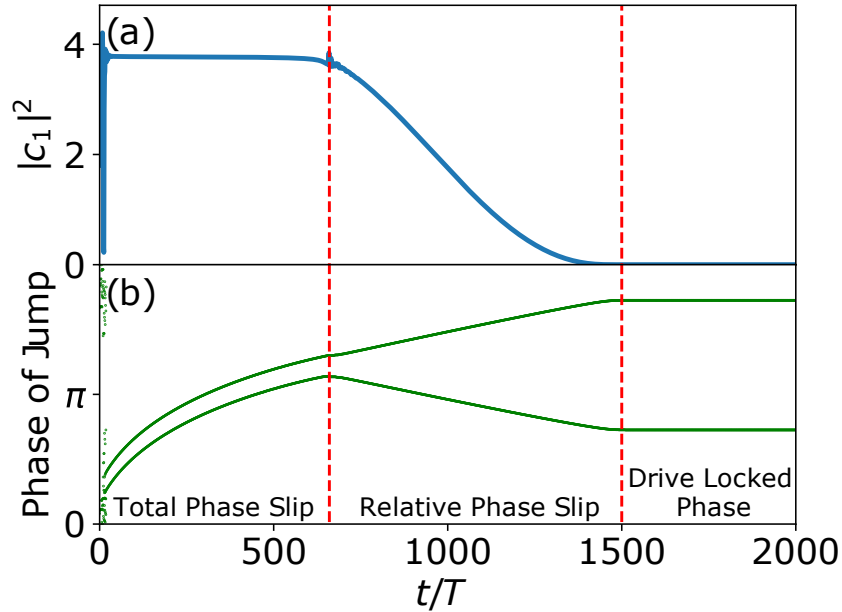
Figure 4.3: (a), The average $|c_1|^2$ component extracted from a Ψ integration with a drive strong
enough to exhibit the phase glide dynamics, $\lambda = 5.8$. (b), The relative phase position of each saw
tooth discontinuity moving from the total phase glide regime, to the relative phase glide regime, to
finally settle into the drive frequency regime with phase separation $\Delta\phi = \pi$. For these integrations
$\gamma = 1/30$, $V = 2$ and $N = 300$.

If c_1 is zero in a particular time window, then the system is drive frequency locked at that time. We found that the average of the c_1 component can remain constant over several hundred (or even thousand) periods, but with the positions of the two jumps are moving later and later in the period. As each of the jumps happens later in the period than in the previous periods the system has to linearly descend slightly further than in the previous period, this manifests as a moving constant off set as the next period begins with a slightly lower starting position than the previous one (See 4.2 at times $50 < t/T < 600$). Because the jumps are moving relative to the drive phase but not relative to each other, we call this behaviour total phase glide.

After a total phase glide, the system undergoes a transitionary period in which $\Delta\phi$ moves from period to period linearly towards $\Delta\phi = \pi$. This transitionary period ends when $\Delta\phi$ becomes π and the oscillations are locked to the drive frequency again. This transition is clear in the later periods of Fig 4.2 and in the second section of Fig 4.3 where we can clearly see the positions of the two jumps moving away from each other towards a separation of π. This behaviour also sees a rapid decrease in the system's c_1 component, showing that the system is moving from a regime where all integer multiples of the natural frequency can exist to one where it will be locked to the drive frequency. Because this behaviour is entirely defined by the fact that the jumps are moving relative to each other, we dub this behaviour the relative phase glide. While a total phase glide leads to a downward movement of the centre of oscillation, for the relative phase glide the movement appears to be symmetric and thus there is no change in constant offset.

Finally, the system settles into a drive locked behaviour. When the system arrives here $\Delta\phi = \pi$ and the system only exhibits frequencies locked to integer multiples of the drive frequencies. This is then the behaviour of the system in the limit of long time. Again, this behaviour is shown explicitly in the last section of Fig 4.3.

This leaves us with a question: how do these dynamical behaviours evolve as the drive (λ) is increased, and from that can we determine anything about how they emerge from the no slip and analytical regimes? This emergence is shown in Fig 4.4 where we have chosen to examine the evolution of c_1 with time for a range of λ values. As λ is increased, the length of time the system has a non-zero c_1 component also increases, indicating that the time spent in the phase glide period is also increasing. Interestingly, this appears not to be a linear relationship, with the amount of time the system spends in the total phase glide growing faster than linear when λ is increased,
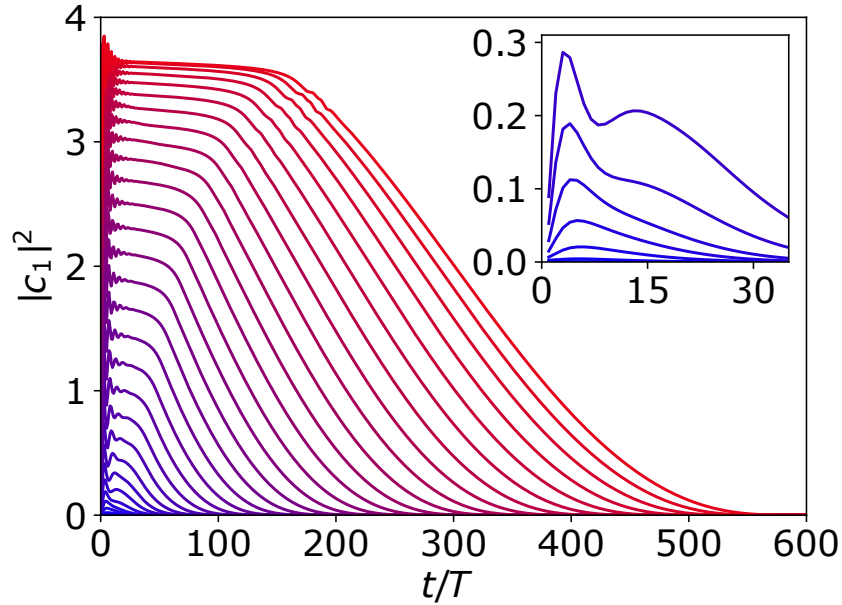
Figure 4.4: Main Figure: The $|c_1|^2$ component of integrations moving from $\lambda = 0$ (blue) to $\lambda = 3.0$ (red) in steps of $\Delta\lambda = 0.1$, showing how the system undergoes longer periods of total phase glide before moving to a relative phase glide. The inset shows the very low energy integrations (up to $\lambda = 0.8$) where any period of total phase glide is lost in the settling down period of the system. for these integrations $\gamma = 1/30$, $V = 2$, and $N = 300$.

however we have not managed to determine any obvious mathematical form that determines this length. When c_1 begins to decrease (at larger t/T for larger λ) we have entered the relative phase glide regime and when it has decayed to zero we have $\Delta\phi = \pi$. Again the length of time in the decay also increases with λ but this appears to be more tied to the value of the c_1 component than the drive strength itself. It should also be noted that the decay in c_1 is not exponential or linear but a more complex relationship and, while it does change with λ, it would appear to be more a function of the starting value of c_1 before the relative phase glide begins.

From the inset in Fig 4.4 it is also very clear that the no slip and analytic regimes are low energy cases of the phase glide dynamics. In these cases, a relative phase glide kicks in so early in the time evolution that a total phase glide is never observed. In fact, these dynamics can occur so early that anything other than a drive locked regime is covered by the initial aperiodic oscillations that appear at the beginning of the integration in these types of problems.

It is also worth discussing the fact that while it may appear from Fig 4.4 that the stable value of c_1 during the total phase glide will always increase as the drive is increased, this is in fact not the

case. What we observe is that after this initial neat increase, the system can take on different values of c_1 during the total phase glide without apparent pattern. What we mean by this is that as λ is increased, c_1 will initially increase, but after a point it will begin to jump about in a non-smooth way. The transition towards this new regime can be seen in the top most values of λ 4.4 which are much closer together than the other values.

It is worth briefly touching on the role that the initial conditions play in this regime of the system. In the analytic regime, the initial conditions have had no influence on the long time dynamics of the system. However, with the highly nonlinear behaviour of the total phase glide regime, we might suspect that they do matter. However, it is difficult to describe exactly how the initial conditions affect the system. This is because the initial conditions affect the system in a very unpredictable way. For example, we can state with certainty that the initial conditions affect the initial phase separation when the system is in a total phase glide, this naturally affects the c_1 component, the constant offset movement, and the time the system spends with relative phase glide, but it can also affect the time the system spends in a total phase glide by a small amount. These changes are incredibly hard to map and thus are not presented here, however they are an important part of the system's dynamics, and so we mention them here for completeness.

Finally, While the majority of the behaviour of $|c_1|^2$ in figures 4.3 and 4.4 is smooth there are two notable exceptions to this, the oscillations at t close to zero and when the system moves from total phase glide to relative phase glide. The oscillations at t close to zero are a consequence of the initial conditions used for the simulations, $\Phi(0) = 0$ and $\dot{\Phi}(0) = 0$, which is not a valid steady state solution (or close to a transient solution such as the phase glides). This means that some oscillations would be expected as the system transitions to the total phase glide. The oscillations as the behaviour switches between the total and relative phase glide can be explained in a similar manner, the switch between the two regimes is not smooth leading to a settling down period.

4.5 Phase Glide Reset Dynamics

While the total phase glide regime occurs for a wide range of drives it is not the final behaviour that is shown by the system, showing a new and distinct form of dynamics emerges. That is the phase glide reset dynamic. What we observe is that after a point the system enters a regime that is in many ways similar to the previous one, as the solution begins by undergoing a total phase glide,

however, this phase glide does not end in a relative phase glide, instead the system undergoes a sudden upset in the form of a brief, relative to the timescale of the dynamics, aperiodic evolution. These oscillations, which still exhibit a sawtooth structure, then settle back into a total phase glide again, though this time with a different phase separation. This reset behaviour is not infinitely repeating, it terminates after a given number of resets. When this occurs, the system undergoes the same relative phase glide transition to drive locked oscillation behaviour that was shown in the previous regime.

Fig 4.5 shows a simple example of this behaviour for $\lambda = 6.2$. In this example we see a single reset, occurring at $t/T = 725$, shown in detail in the inset. The oscillations at this time are aperiodic before the system settles back into another total phase glide period. The system then begins the transition dynamics at $t/T = 1450$ and has become drive locked by $t/T = 1800$.

The reset phenomenology that emerges for sufficiently large λ values is extremely complex. For example, one might naively expect that as we begin to increase λ we would see one reset, then two, and so on, however, this is simply not the case. Nevertheless, we can make several generalisations about this regime: as we increase λ, we see more resets, the total time over which total phase glide
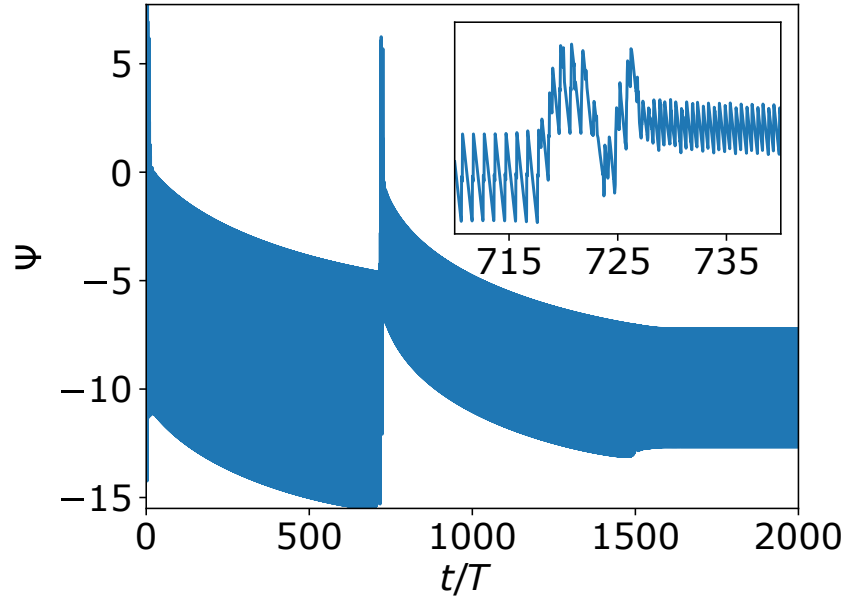

Figure 4.5: An example integration of Ψ with a drive strong enough to exhibit the phase glide reset dynamics, $\lambda = 6.2$. The inset shows aperiodic reset experienced by the system which resets the systems relative phase. For this integration $\gamma = 1/30$, $V = 2$, and $N = 300$.
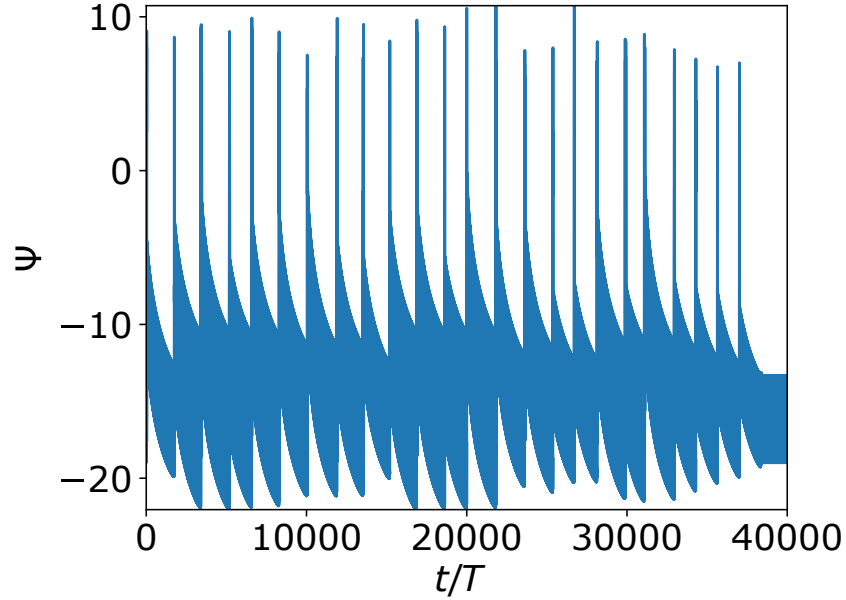
Figure 4.6: Numerical integration of Ψ with a drive strength of $\lambda = 10.0$ which is well into the phase glide reset dynamical regime. This particular example takes a very long time to reach a drive locked steady state, several thousand times the characteristic time periods given by the damping rate of $\gamma = 1/30$, and there are 24 total phase resets. In this integration $N = 300$. and $V = 2$

behaviour is seen increases and the aperiodic windows between resets get larger. However, these are just general trends. For example, it is possible, for a higher drive such as $\lambda = 6.5$, to observe no resets. The number of resets is also not set by λ alone. If the initial conditions of the system change then the number of the resets seen for a given λ will also change, along with the length of the total phase glide and aperiodic resets, again similar to the behaviour in the total phase glide regime.

There is only one thing that is always consistently observed in this regime: The system will always eventually undergo a relative phase glide and in the long time limit become a drive frequency locked oscillation. The time periods over which these dynamics evolve can be very long. Fig 4.6 shows the integration for $\lambda = 10$ which shows 24 resets before becoming drive locked at $t \approx 40,000T$ which is several orders of magnitude longer than a characteristic timescale based on the system's dissipation would suggest $(1/\gamma = 1/30)$.

With such strange, unexpected, results it is reasonable to check their accuracy from a numerical point of view. To verify these results, the same calculation shown in 4.6 was run using all three possible calculation methods; the full set of equations, the Volterra equation and the truncated

Volterra equation. Results for each of these methods were obtained using two different programming languages (MATLAB and Python) and were computed independently by different researchers. In all cases the same result was obtained and a phase glide reset behaviour was confirmed to be present. As such, it seems very unlikely that this behaviour is a result of some numerical or procedural error.

It is clear that the reset regime is incredibly complex and while we can talk in broad generalities about what the system may do, there appears to be no good method for predicting how a specific integration may behave before the inevitable transition to drive locked oscillations. The only two constants appear to be the increasing time scales as we increase λ, and that the system will always become drive locked in the long time limit.

4.6   Beyond phase glide

With the increasing times scales of the reset dynamics, it becomes interesting to ask: Can we move beyond this behaviour into a different regime? Fig 4.7 shows an integration performed with $\lambda = 140$. In case the system still appears to have transitioned into a regime where the dynamics are radically different, still showing a saw tooth like structure, but it is either aperiodic, or exhibiting a very
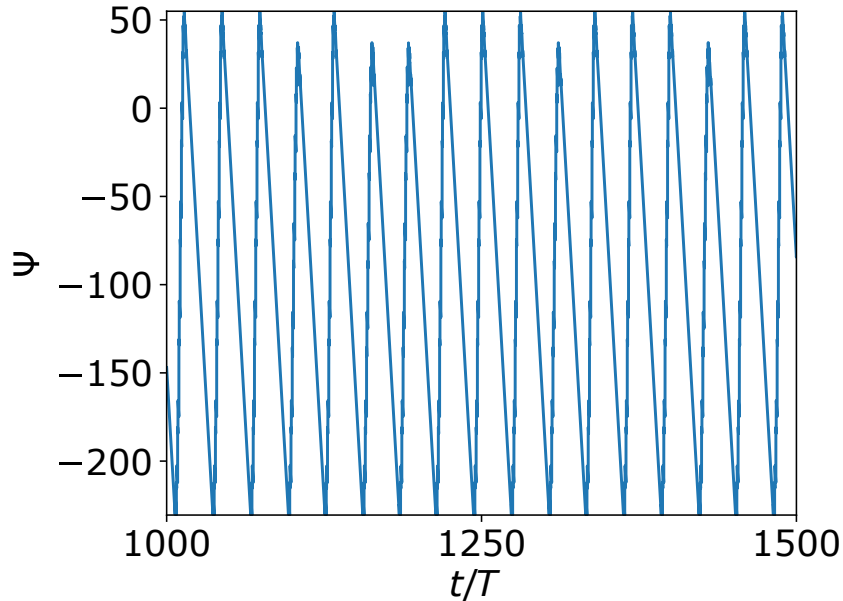

Figure 4.7: An example integration of Ψ with a drive strong enough to have moved past the phase glide reset dynamics into a solution that is either aperiodic, or exhibits a very large periodicity, $\lambda = 140$. For this integration $\gamma = 1/30$, $V = 2$ and $N = 300$.

long periodicity. In the case of $\lambda = 140$, the deviation from earlier forms of periodic behaviour is dominated by the system flicking between the tall waves and slightly shorter ones, but a behaviour similar to this is common in this regime. It is not clear why the system does this.

Just like when even after the system enters the phase glide reset regime, it can still slip back to simply the total phase glide behaviour, aperiodic behaviour can also drop back into phase glide rest dynamics. For example, in Fig. 4.7 we show an integration with $\lambda = 140$, however if we were to move to an integration with $\lambda = 145$, the system would actually demonstrate a very long phase glide reset behaviour. Given the rich verity of complex dynamics that occurs up to λ 150, it is far from clear what might emerge for even larger drive strength.

4.7 Discussion

In contrast to Simon and Cooper[32] who predict the emergence of a stable period T (i.e. the period of the fundamental mode) behaviour in the large N limit, we find a complex range of different regimes none of which settle down to period T. We summarise our findings about how the dynamics evolve with increasing drive below:

1. The analytic regime: For very weak drive, $\Psi \ll 1$, the system has a sinusoidal response with only a few higher modes excited. The system is locked to multiples of the drive frequency and can be approximated using a perturbation based method.

2. The no slip regime: The system has many modes excited and begins to look like a sawtooth, but the period is that of the drive frequency. The analytical methods used to describe the previous regime break down.

3. The total phase glide regime: For the $V = 2\omega_0$ case the solution first settles into a double saw tooth with a non π phase separation (i.e. period T oscillations) that stays constant but moves forward each period giving the illusion of a constant offset decay. This will eventually undergo a relative phase glide, where the sawtooth jumps move each period until the phase separation is π. At this point, the behaviour is stable in the long time limit, oscillating at the drive frequency.

4. The phase glide reset regime: Similar to the total phase glide regime, however, after the system has undergone a total phase glide it undergoes an aperiodic phase reset into another

total phase glide regime. This will repeat until a relative phase glide occurs and the phase separation is π. At this point, the behaviour is stable in the long time limit, again with the period of the drive frequency.

5. At even higher λ the system can become aperiodic, or may develop a periodic behaviour with a very long periodicity, as there is no clear pattern though this behaviour that we could discern.

We note that other regimes may occur for very large λ that we have not acknowledged here.

It is worth taking some time to reflect and contrast our results with the results that were observed and described by Simon and Cooper. As discussed in Chapter 2, Simon and Cooper's main achievement was to show that an analytical solution to the dynamics could be found, which was a period T sawtooth. In this regime, when the system is sufficiently driven by a voltage set to $m\omega_0$, would form a solution with m overlapping sawtooth waves with period T, leading to a periodic solution with m discontinuous phase glides per period.

From this description it is not immediately clear whether or not our results, with the demonstrated phase glide reset dynamics, are actually compatible with Simon and Cooper's description of the system. For example, Simon and Cooper's description of the system is strictly periodic with period T, via the definitions in their derivation, and if this is so this structure should correspond to the long time limit behaviour. What we observe is qualitatively very close to this behaviour, but the quantitative behaviour is very different in some ways. Take the total phase glide behaviour for example, qualitatively this looks to be very similar, with the system experiencing two phase glides per period and otherwise exhibiting a linear downward trend, but the fact that the slips move means we exhibit a non-constant offset signalling that the system has not fully settled down. The same can be said for the relative phase glide regime and the resets as well. But, what we do observe is that the long time stable behaviour that we do observe is locked to the drive frequency, rather than to the natural frequency.

This raises the question of why do we see this discrepancy in the observed behaviour of the JJ laser? The first thing to address is the possibility of numerical error in these systems. This seems unluckily as these effects, the phase glide reset dynamics etc., could all be reproduced using all three methods presented in appendix C which, if there was a numerical inaccuracy in any one of the methods, we would expect to show different results due to the relative volatility of the system

when making small changes. Thus, we conclude that the different behaviours we observe must have a physical interpretation. The only real place where our system can deviate then is if our choice of γ might be too large to be compatible with Simon and Cooper's assumptions. However, it is not quite clear why this would be true, as γT could still be considered small for all the values that we explored. However, if there are small changes in each period (neglected by Simon and Cooper's calculations) this may explain the large scale dynamics that we do see, and it suggests that Simon and Cooper's results are only valid in the $\gamma \to 0$ limit. However, this still fails to explain the reset dynamics and why a solution with equidistant phase glides is stable.

4.8 Conclusions

In this chapter, we discussed analytical approximations and numerical solutions to the equations of motion for the JJ laser system in the many mode limit. We established, through a perturbative method, that for weak drives the system is only capable of responding to a drive with a frequency that matches an integer multiple of the drive frequency, thus when driven with sufficient force the system responded with a sawtooth function like wave.

We then explored the overall behaviour of the system with many modes numerically as the drive strength was increased and introduced the idea of the phase glide behaviour. We showed that as the system was driven past the point where the perturbative approximations broke down, it began to exhibit a long-lasting transient sawtooth behaviour that was locked to the natural frequency of the lowest oscillator. This behaviour was transient as the system exhibited a total phase glide and would eventually undergo a relative phase glide towards a drive locked oscillation, which was the stable long-time regime behaviour. We found that a range of more complex behaviours emerged at stronger drives, but never found long time behaviours that were period T.

Many questions are left unanswered. For example, when the system is forced outside of the phase glide reset dynamics, what are the characteristics of this regime, is this the final behaviour, and does this relate to the dynamics of the just off resonant behaviour described by Simon and Cooper? What are the dynamics of the system when off resonance, and does the system still exhibit a phase glide at all? Is there any analytical description that can predict the existence of the long time drive locked behaviour?

Chapter 5

Dynamics of a Josephson Junction Laser with Few Modes

5.1 Introduction

In Chapter 2 we detailed the theoretical description first put forward by Simon and Cooper[32] to describe the Josephson junction laser realized by M. C. Cassidy et al.[31]. As was detailed in Chapter 4 all the calculations and simulations were done in the limit that the system could have access to many modes, such that the kernel would form a perfect sawtooth function in the limit of weak driving. In this chapter, we use the same model notation, but focus instead on cases where a relatively small number of modes is involved. This provides a good way of describing cavity systems, where the cavity damping may increase with mode number, leading quite naturally to a limit on the number of modes involved in the dynamics. In contrast to the many mode case, we find a discrete time translation symmetry breaking transition which the system undergoes as it moves from a drive frequency locked oscillation to one locked to the fundamental mode frequency. We will study how this symmetry breaking event occurs though the system's parameter space, with the aim of uncovering the general rules for where and when these transitions occur.

The rest of this chapter is organized as follows. In Section 5.2 we will describe in detail the discrete time transitional symmetry breaking transition and detail the two possible forms it can take, discontinuous and continuous. In Section 5.3 we will detail two analytical approximations that

can be applied in the case when there is only one resonantly driven mode in the system of equations. Next, Section 5.4 explores discontinuous transition behaviour in more detail.Then Section 5.5 will investigate the dynamics of the transition for specific voltages as we increase the number of available modes. In Section 5.6 we will detail why this formulation is necessary by implementing a realistic loss structure to the system. In Section 5.7 we will briefly discuss the dynamics of these systems when the drive frequency isn't an integer multiple of the lowest mode frequency. Finally, in Section 5.8 we will give some conclusions about the JJ laser system as a whole and discuss any possible further work that could be done on the system.

Details of the work presented in this chapter have been submitted for publication. [34].

5.2 Definition of the System Transition

The most important feature of the dynamics in the few mode limit is a clear transition in the long time behaviour from oscillations with a period set by the drive at lower couplings to oscillations with period set by the fundamental mode frequency. This transition, which proved so elusive in the many mode limit, constitutes a breaking of the discrete time translational symmetry of the system. In this case, we are defining discrete time translational symmetry breaking as a system for which $\Psi(t) = \Psi(t+T)$ in a given drive range moving to a drive regime where $\Psi(t) \neq \Psi(t+T)$, where T is some well defined time. This behaviour is illustrated in Fig 5.1 where Fig 5.1 (a) shows the stable oscillations for a system with $N = 6$ which are clearly fixed to the drive frequency. However, as the strength of the drive increases, the system begins to exhibit a solution like Fig 5.1 (b), oscillations with period $T = 2\pi/\omega_0$.

A good measure of the period of $\Psi(t)$ can be obtained from the first Fourier component for an integration that has reached the long time limit (and discussed in Chapter 4). We shall call this the $|c_1|^2$ measure. This can be calculated using the standard methods for finding the Fourier component for a single frequency[69]. If the system has a period T then the system has a non-zero $|c_1|^2$ component and if it is locked to the drive frequency then $|c_1|^2 = 0$.

A clear consequence of this change in periodicity is that there must be a transition from one of these behaviours to the other and as we are moving from a regime with periodicity $T/2$ to T, it is clear that this transition will be in the form of a discrete time symmetry breaking event. We will call the position of this symmetry breaking event the critical drive, λ_{crit}. Two examples of the

system undergoing this transitioning are shown in 5.2 for $N = 6$ and $N = 7$ showing two different ways in which the transition can occur.

Fig 5.2 (a) shows how $|c_1|^2$ evolves as a function of λ for $N = 6$. In this case the transition is discontinuous, as when the system reaches a critical value of λ/γ there is a sudden transition from having no $|c_1|^2$ component to having a non-zero $|c_1|^2$. The transition is very abrupt, shown by the fact there are no data points present between the cases where $|c_1|^2 = 0$ and where the system picks up its new trend.

Fig 5.2 (b) shows the corresponding behaviour for $N = 7$. In this case the system will smoothly move from having $|c_1|^2 = 0$ to having a non-zero $|c_1|^2 = 0$, hence a continuous transition[1].

The features of these transitions are universal amongst mode frequencies, reflected in the behaviour of all the Fourier modes. When the system is in a regime that is locked to the drive frequency, all Fourier components of $\Psi(t)$ that aren't at an integer multiple of the drive frequency are unexcited, leading to an alternating exited and unexcited pattern (for $V = 2$) when we plot all

---

[1]Because of the smooth nature of this type of transition, determining the exact position of the transition, λ_{crit}/γ is rather difficult to do precisely. To do this, we fitted a linear trend to the portion of the $|c_1|^2$ that rapidly increases and then see where this line crosses the intercept. This method will be shown later on to agree very well with analytical approximations of the transition

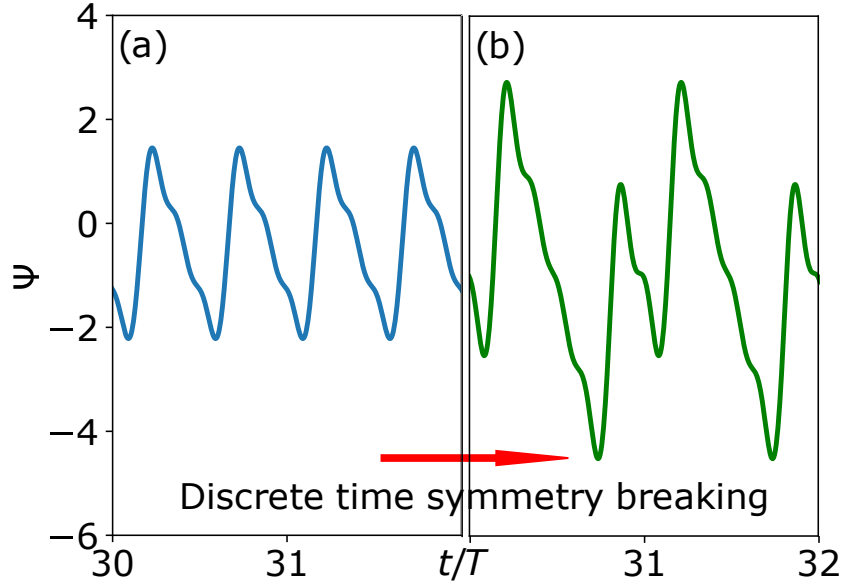Figure 5.1: (a) Numerical integration of Ψ for $\lambda/\gamma = 12$, $\gamma = 1/30$, and $N = 6$ showing a drive locked regime with period π/ω_0 set by the drive frequency $V = 2\omega_0$. (b) The integration of Ψ for $\lambda/\gamma = 24$, $\gamma = 1/30$, and $N = 6$. These oscillations have passed the critical threshold for a discrete time symmetry breaking and have period $T = 2\pi/\omega_0$.

of these frequencies together as shown in Fig 5.3. Once the system is driven past the critical drive, all integer frequencies are present in the system, and they become present at the same critical drive as $|c_1|^2$ and in the same manner. In other words, all unexcited components will become exited in a continuous manner if $|c_1|^2$ changes continuously in a discontinuous manner if $|c_1|^2$ is discontinuous. Additionally, when we examine the modes associated with the integer frequencies, we see similar behaviour in the mode amplitude, A_n, to $|c_n|^2$, i.e. A_n undergoes the same transition to $|c_n|^2$. However, at drives less than λ_{crit} these amplitudes are not fully inactive like $|c_n|^2$ but instead show weak off-resonant oscillations at integer multiples of the drive frequency.

5.3   Calculating the critical coupling analytically

The fact that we are dealing with only a few modes suggests that it may be possible to determine where the transition occurs analytically. In this section, we outline an approach that seeks to identify when the fundamental mode becomes exited. The strategy involves determining when a zero amplitude solution becomes unstable. This can be applied to (some) cases where the transition
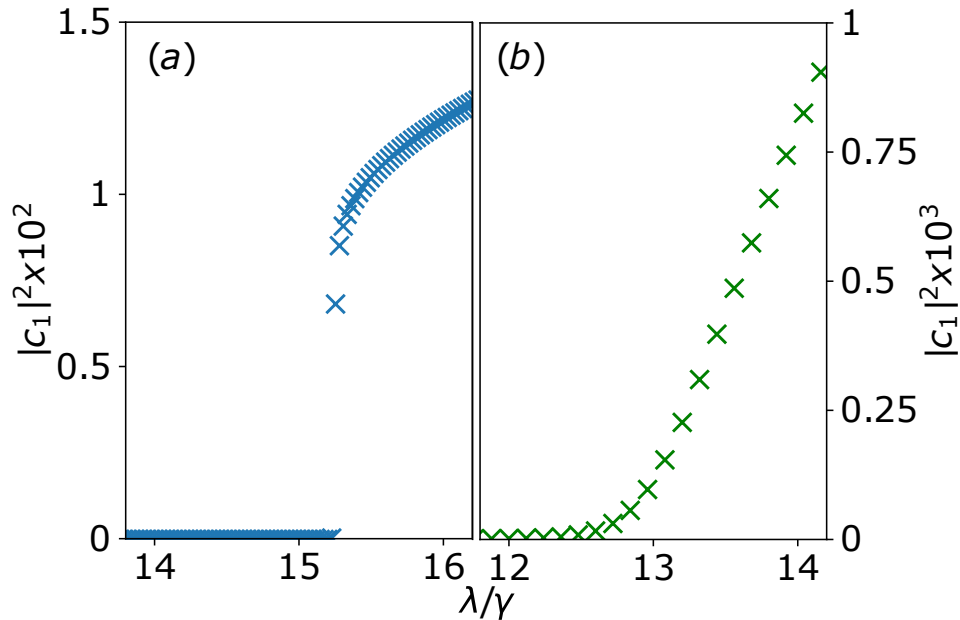

Figure 5.2: The evolution of the Fourier component of $\Phi(t)$ at frequency ω_0 with coupling for a) $N = 6$ and b) $N = 7$ in the limit of large t. For N=6, the value of $|c_1|^2$ jumps to a non-zero value abruptly (discontinuous transition), but for $N = 7$ it grows smoothly (continuous transition). Here $\gamma = 1/30$ and $V = 2$.
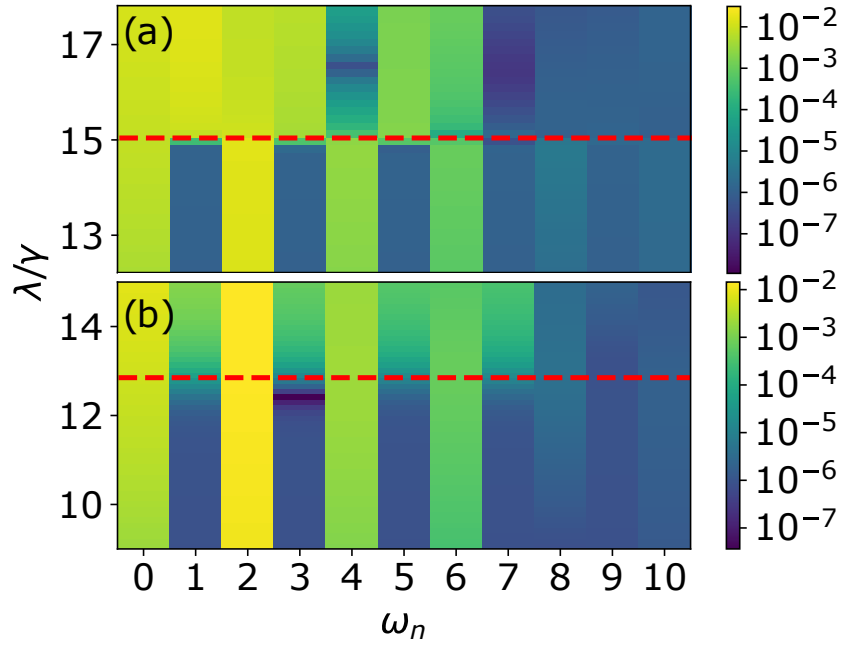
Figure 5.3: Behaviour of Fourier components of $\Psi(t)$, $|c_n|^2$, as a function of λ (plotted on a log scale) for a) $N = 6$ and b) $N = 7$. The red dotted lines indicate the transition. Here $\gamma = 1/30$ and $V = 2$. Note that the column denoted as ω_0 is the absolute value of the constant offset experienced by the system.

is continuous.

5.3.1 Analytical Approach for $V = 2$, $N = 3$

Let's first begin by examining the specific case of $V = 2$ and $N = 3$. The method presented here is based on a similar method for the case of $V = 2$ and $N = 1$ first derived by A. Armour[27]. We choose $V = 2$ and $N = 3$ specifically because only one harmonic, ($\omega_2 = 2\omega_1$), will be resonantly excited for $V = 2$ (recall that V is in units of ω_1). Any higher mode number (e.g. $\omega_4 = 4\omega_1$) will lead to a case where we have more than one resonantly driven mode[2]. This will inevitably lead to a much more complex analytical formulation, which we wish to avoid.

For simplicity, we assume that the cavity modes are such that the Josephson junction is perfectly at a node of the electromagnetic oscillation, $\alpha_{1-3} = 1$, each has a quality factor, Q_{1-3}, that scales linearly with the mode's frequency thus having a uniform loss rate, $\gamma_{1-3} = \gamma$. As in Chapter 4, the frequencies (in units of ω_1) are: $\omega_1 = 1, \omega_2 = 2, \omega_3 = 3$. Thus, it follows from equation (2.12) that

---

[2]Here we use the term resonantly driven very loosely, it is a shorthand for a mode with a frequency which is an integer multiple of the drive

a complete set of dynamical equations takes the form,

$$\ddot{\phi}_1 = -\phi_1 - 2\gamma\dot{\phi}_1 + \lambda\sin(Vt + \phi_1 + \phi_2 + \phi_3) \tag{5.1}$$

$$\ddot{\phi}_2 = -\phi_2 - 4\gamma\dot{\phi}_2 + \lambda\sin(Vt + \phi_1 + \phi_2 + \phi_3) \tag{5.2}$$

$$\ddot{\phi}_3 = -\phi_3 - 9\gamma\dot{\phi}_3 + \lambda\sin(Vt + \phi_1 + \phi_2 + \phi_3), \tag{5.3}$$

which we would have to solve simultaneously if we wanted a full set of solutions. However, in order to locate the transition, we need only determine the stability of oscillations in the ϕ_1 mode, and thus we can simplify things

Firstly, ϕ_2, will be resonantly driven and we can assume that it will be the only one to have a significant amplitude, so $\phi_1, \phi_3 \ll 1$. Consequently, the ϕ_2 equation of motion can be solved by neglecting $\phi_1 + \phi_3$, as the effect of the other two modes on ϕ_2 will be minimal compared to its own value. Secondly, we can drop non-resonant terms in the equations making a rotating wave approximation.

We define the mode's complex amplitude, α_i (with $i = 1, 2, 3$) as,

$$\alpha_i = \phi_i + i\dot{\phi}_i/\omega_i \tag{5.4}$$

and using the generic rotating ansatz for an oscillating system $\phi_i = A_i \cos(\omega_i t + \theta_i)$ we can see that the complex amplitude is given by,

$$\alpha_i = A_i e^{-i\omega_i t} e^{-i\theta_i} \tag{5.5}$$

and thus,

$$\phi_i = \frac{\alpha_i + \alpha_i^*}{2} \tag{5.6}$$

$$\dot{\phi}_i = \frac{\omega_i(\alpha_i - \alpha_i^*)}{2i}. \tag{5.7}$$

Using this substitution the equation for $\dot{\alpha}_1$ takes the form,

$$\dot{\alpha}_1 = -i\alpha_1 - \gamma\alpha_1 + i\lambda\sin(2t + \phi_1 + \phi_2 + \phi_3). \tag{5.8}$$

We know that this mode will only begin to show significant oscillations when it begins to respond

at its natural frequency, ω_1, thus it makes sense to move this mode into a rotating frame at this frequency. To do this we perform the substitution $\tilde{\alpha}_1 = \alpha_1 e^{it}$,

$$\dot{\tilde{\alpha}}_1 = \dot{\alpha}_1 e^{it} + i\alpha_1 e^{it} \tag{5.9}$$

$$\dot{\tilde{\alpha}}_1 = -\gamma\tilde{\alpha}_1 + i\lambda e^{it} \sin(2t + \phi_1 + \phi_2 + \phi_3). \tag{5.10}$$

This has taken the terms that would normally oscillate at the frequency of ω_1 in the α frame and transformed them into stationary terms in the $\tilde{\alpha}$ frame. However, we still have time dependent terms from the sine term in equation (5.10). But we know already that the off resonant terms, terms that aren't stationary in the $\tilde{\alpha}$ frame should be inconsequential, so we can choose to ignore them allowing us to write equation (5.10) as fully time independent. This is the rotating wave approximation (RWA). To do this we must pick out each of the terms in $\sin(2t + \phi_1 + \phi_2 + \phi_3)$ that oscillate with e^{-it} as this will be counteracted by the e^{it} in the final term of (5.10) to give a stationary equation. To do this without approximation would give an infinite number of terms, so we choose to use the fact that $\phi_1, \phi_3 \ll 1$ to simplify this significantly. Expanding the sine term to lowest order in ϕ_1 and ϕ_3 gives,

$$\sin(2t + \phi_1 + \phi_2 + \phi_3) \approx (\phi_1 + \phi_3)\cos(2t + \phi_2) + \sin(2t + \phi_2), \tag{5.11}$$

of which only the first term is actually relevant, as $\sin(2t + \phi_2)$ cannot give terms of order e^{-it}. We write $\phi_2 = A_2 \cos(2t + \theta_2)$ and use the Jacobi-Anger expansion to pick out the time independent terms when ϕ_1 and ϕ_3 are written in terms of $\tilde{\alpha}_1$ and $\tilde{\alpha}_3 = \alpha_3 e^{+i3t}$ (together with its complex conjugate). Performing this task carefully yields,

$$\dot{\tilde{\alpha}}_1 = a_1\tilde{\alpha}_1 + a_2\tilde{\alpha}_1{}^* + a_3\tilde{\alpha}_3 + a_4\tilde{\alpha}_3 \tag{5.12}$$

$$a_1 = -\gamma + \frac{\lambda}{2}J_1(A_2)\sin(\theta_2) \tag{5.13}$$

$$a_2 = \frac{i\lambda}{4}(J_0(A_2) - J_2(A_2)e^{-2i\theta_2}) \tag{5.14}$$

$$a_3 = \frac{i\lambda}{4}(J_0(A_2) - J_2(A_2)e^{2i\theta_2}) \tag{5.15}$$

$$a_4 = \frac{\lambda e^{-2i\theta_2}}{4}(J_1(A_2) - J_3(A_2)), \tag{5.16}$$

where $J_n(A_2)$ is the nth Bessel function of the first kind. This is the RWA equation of motion for

the first mode of the cavity.

The value of the amplitude of the first mode is tied to the amplitude and phase of both other modes. This is not all that surprising but we can make one key assumption here, α_1 depends on A_2 and θ_2 but because $\phi_1 \ll \phi_2$ it is unlikely that A_2 and θ_2 will have a significant dependency on α_1, thus we can calculate A_2 and θ_2 while ignoring ϕ_1 and ϕ_3 and still be able to accurately calculate α_1. However, while we don't need α_2, we do require α_3 to be calculated simultaneously.

To get the equation of motion for α_3 we go through the same procedure, find the new complex amplitude equation of motion,

$$\dot{\alpha_3} = -i3\alpha_3 - \gamma\alpha_3 + \frac{i\lambda}{3}\sin(2t + \phi_1 + \phi_2 + \phi_3) \tag{5.17}$$

perform variable replacement into the rotating frame such that $\tilde{\alpha}_3 = \alpha_3 e^{+3it}$. Carrying out the same steps as for $\tilde{\alpha}_1$, leads to,

$$\dot{\tilde{\alpha}}_3 = b_1\tilde{\alpha}_3 + b_2\tilde{\alpha}_3{}^* + b_3\tilde{\alpha}_1 + b_4\tilde{\alpha}_1 \tag{5.18}$$

$$b_1 = -\gamma + \frac{\lambda}{6}J_1(A_2)\sin(\theta_2) \tag{5.19}$$

$$b_2 = \frac{i\lambda}{12}\Big(J_0(A_2)e^{-2i\theta_2} - J_2(A_2)\Big)e^{-2i\theta_2} \tag{5.20}$$

$$b_3 = \frac{i\lambda}{12}\Big(J_0(A_2) - J_2(A_2)e^{2i\theta_2}\Big) \tag{5.21}$$

$$b_4 = \frac{\lambda}{12}\Big(J_1(A_2)e^{-2i\theta_2} - J_3(A_2)\Big)e^{-2i\theta_2}, \tag{5.22}$$

and we can use complex conjugation to find the equations of motion for $\tilde{\alpha}_1^*$ and $\tilde{\alpha}_3^*$ as well.

To determine when the non-zero amplitude for mode 1 emerges, we can examine the stability of the zero amplitude solution. We write the system as a matrix problem $\dot{\boldsymbol{\alpha}} = M\boldsymbol{\alpha}$ then provided that the transition is continuous then a non-zero solution for A_1 should emerge when M has a real eigenvalue so that the zero amplitude solution is unstable. The matrix equation is given by,

$$\begin{pmatrix} \dot{\tilde{\alpha}}_1 \\ \dot{\tilde{\alpha}}_1^* \\ \dot{\tilde{\alpha}}_3 \\ \dot{\tilde{\alpha}}_3^* \end{pmatrix} = \begin{pmatrix} a_1 & a_2 & a_3 & a_4 \\ a_1^* & a_2^* & a_3^* & a_4^* \\ b_1 & b_2 & b_3 & b_4 \\ b_1^* & b_2^* & b_3^* & b_4^* \end{pmatrix} \begin{pmatrix} \tilde{\alpha}_1 \\ \tilde{\alpha}_1{}^* \\ \tilde{\alpha}_3 \\ \tilde{\alpha}_3{}^* \end{pmatrix} \tag{5.23}$$

but this equation still depends on A_2 and θ_2.

To find A_2 and θ_2 we need to calculate α_2 but this is much simpler. As we can choose to ignore ϕ_1 and ϕ_3 as they should have a inconsequential effect on the resonantly driven mode we can write the equation of motion for ϕ_2 as,

$$\ddot{\phi}_2 = -\phi_2 - 4\gamma\dot{\phi}_2 + \lambda\sin(Vt + \phi_2) \tag{5.24}$$

again moving to a rotating frame and performing a harmonic balance it is fairly easy to show[27] that the RWA equation of motion is,

$$\dot{\tilde{\alpha}}_2 = -\gamma\tilde{\alpha}_2 - \frac{\lambda}{4}(J_0(A_2) + J_2(A_2)e^{-2i\theta_2}). \tag{5.25}$$

Using $\tilde{\alpha}_2 = A_2 e^{-i\theta_2}$ we can show that,

$$\dot{A}_2 = -\gamma A_2 - \frac{\lambda}{4}(J_0(A_2) + J_2(A_2))\cos(\theta_2) \tag{5.26}$$

$$\dot{\theta}_2 = \frac{\lambda}{4A_2}(J_0(A_2) - J_2(A_2))\sin(\theta_2). \tag{5.27}$$

For these to be in a steady state solution we look for the case where $\dot{A}_2 = \dot{\theta}_2 = 0$. For the relevant range of λ values there exists a singe stable fixed point given by $\theta_2 = \pi$ and $A_2 = \frac{\lambda}{4\gamma}(J_0(A_2) + J_2(A_2))$.

Using these values of θ_2 and A_2 we can now numerically find the eigenvalues of $\bar{M}$ and determine the λ_{crit} at which the system begins to have oscillations at ω_0. In this particular case, it is found that this value is $\lambda_{crit}/\gamma = 7.76$.

This method can also be used to calculate λ_{crit} for $V = 2$ and $N = 2$ in a very similar way. However, when we do this we find that M never actually picks up a real eigenvalue. This implies that the solution where $\tilde{\alpha}_1 = 0$ never becomes unstable. This is consistent with the discontinuous transition found in the numerical integration for the $V = 2$, $N = 2$ case.

The same method can also be used for calculating the case of $N = 1$ and $V = 2$[27]. In this case the system is much simpler as we only have to deal with a single equation that always has a small amplitude as it is not resonantly driven. In this case, $\tilde{\alpha}_1$ becomes unstable at $\lambda = 4$.

A comparison of these results are shown in Fig 5.4 for $N = 1$ and $N = 3$. Two things are clear

from this. Firstly, the approximations make good predictions for when these systems undergo the discrete time symmetry breaking event. Secondly, both of these systems undergo what we would characterise as a continuous transition.

5.3.2   Analytical Approximation for $V = 2N - 1$

In the previous section, we analysed the case where $N = 3, V = 2$. We now look at how the method can be generalised to other cases where only one mode is resonantly driven, i.e. any N between $N = V$ and $N = 2V - 1$. In these cases, it is clear that the dynamics of the off resonant modes will depend on the amplitude and the phase of the resonantly driven mode. We will consider the case where $N = 2V - 1$. But the same approach can be applied for fewer modes, down to $N = V$.

Let us consider a system of $N = 2V - 1$ modes which has the same properties as those considered in the previous section. We can write the system as a set of simultaneous differential equations,

$$\ddot{\phi}_n = -\omega_n \phi_n - 2\gamma \dot{\phi}_n - \lambda \sin\left(Vt + \sum_{m=1}^{2V-1} \phi_m\right). \tag{5.28}$$

Again we introduce the complex amplitude for each mode $\alpha_n = \phi_n + i\dot{\phi}_n/\omega_n$ and perform a
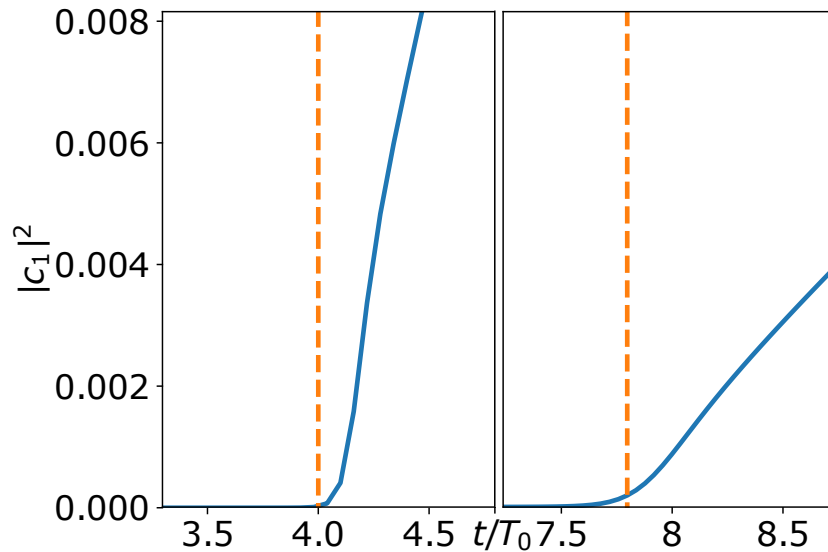

Figure 5.4: First Fourier component, $|c_1|^2$, as a function of λ for a) $N = 1$, $V = 2$ and b) $N = 3$, $V = 2$. The Blue curves are from numerical integration and the red dashed lines are the transitions predicted by the stability analysis. For both cases $\gamma = 1/30$.

transformation into the rotating frame $\tilde{\alpha}_n = \alpha_n e^{-i\omega_n t}$. Doing this and rearranging to make $\dot{\alpha}$ the subject, we find the rotating frame equations of motion to be,

$$\dot{\tilde{\alpha}}_n = -\gamma\tilde{\alpha}_n + \gamma\tilde{\alpha}_n^* e^{2i\omega_n t} + \frac{i\lambda}{\omega_n} e^{i\omega_n t} \sin\left(Vt + \sum_{m=1}^{2V-1} \tilde{\alpha}_n\right). \tag{5.29}$$

Again, at this point we must make two assumptions. Firstly, the resonantly driven mode $(n = V)$ will not depend on all the other mode amplitudes as they are far smaller than it, and thus will have little effect compared to the resonant driving and its own amplitude. Secondly, that the off resonant oscillations in all other modes are inconsequential and therefore can be ignored. This means that we can calculate the resonantly driven mode amplitude as if it were the only mode and solve for it independently, and we can also ignore all non-stationary terms in all the equations, again performing a RWA to simplify the calculation.

The resonantly driven mode's amplitude is calculated in the exact same way as in section 6.4.1 with the phase being locked to $\theta_V = \pi$ and an amplitude A_V, given by,

$$A_V = \frac{\lambda}{2V\gamma}(J_0(A_V) + J_2(A_V)), \tag{5.30}$$

which can be solved numerically. Again because of the small influence of the system's other modes these A_V and θ_V values should be sufficient to calculate the transition points of other modes.

We now must, for a given $\tilde{\alpha}_n$, find all the stationary terms given a small angle approximations for all non resonantly driven modes, $\phi_n \ll 1$ for $n \neq V$. Using this and the fact that we can write $\phi_n = A_n \cos(\omega_n t + \theta_n)$, we can turn the sines and cosines into its exponential components and perform a RWA to extract the time-independent terms. This calculation is fiddly, but if done carefully it yields a generic RWA equation of motion for a non-resonantly driven mode $(n \neq V)$ as,

$$\dot{\tilde{\alpha}}_n = -\gamma\tilde{\alpha}_n + i\frac{\lambda}{4n} \sum_{a=-\infty}^{\infty} \sum_{k\neq V} \left(\delta_0^{n-k+V+aV}\tilde{\alpha}_k F_a^+ \right. \tag{5.31}$$

$$\left. +\delta_0^{n+k+V+aV}\tilde{\alpha}_k^* F_a^+ + \delta_0^{n-k-V+aV}\tilde{\alpha}_k + F_a^- + \delta_0^{n+k-V+aV}\tilde{\alpha}_k^* F_a^-\right)$$

where δ_0^x is the Kronecker delta, the sum over k runs over all modes except the resonant one, and

the F functions are defined by,

$$F_a^\pm = i^a J_a(\pm A_V)e^{ia\theta_V}. \tag{5.32}$$

From this, it is clear that there are two situations that can occur for a given $\tilde{\alpha}_n$. If $n - k = aV$ for a given k, this corresponds to a $\tilde{\alpha}_n$ dependency with the corresponding coefficient that will depend on $F_{a+1}^+ + F_{a-1}^- = G_a$. If $n + k = aV$ then the equation has a $\tilde{\alpha}_k^*$ dependency with the corresponding coefficient will depend on the same factor.

This gives us a full set of equations of motion for this system that can be written in matrix form, $\dot{\vec{\tilde{\alpha}}} = M\vec{\tilde{\alpha}}$ where $\vec{\tilde{\alpha}} = (\tilde{\alpha}_1, \tilde{\alpha}_1^*, ..., \tilde{\alpha}_n, \tilde{\alpha}_n*)$, with $\tilde{\alpha}_V^{(*)}$ omitted. The form of this matrix, M, which turns out to be sparse, is shown in Fig 5.5 for the case of $N = 5$, $V = 3$ and for a generic case. This approach gives a solution for the full $N = 2V - 1$ system, however it can be altered to apply all the way down to $N = V$. For a system of j oscillators below the $N = 2V - 1$ limit we simply eliminate all the terms with a mode above $n = 2V - 1 - j$ and then reconstruct the matrix. In each case, the critical coupling λ_{crit} is obtained by determining when one or more of the eigenvalues of the corresponding matrix M have positive real parts.

The numerical results for the λ_{crit}/γ determined from a matrix for systems with $N = 2V - 1$ are
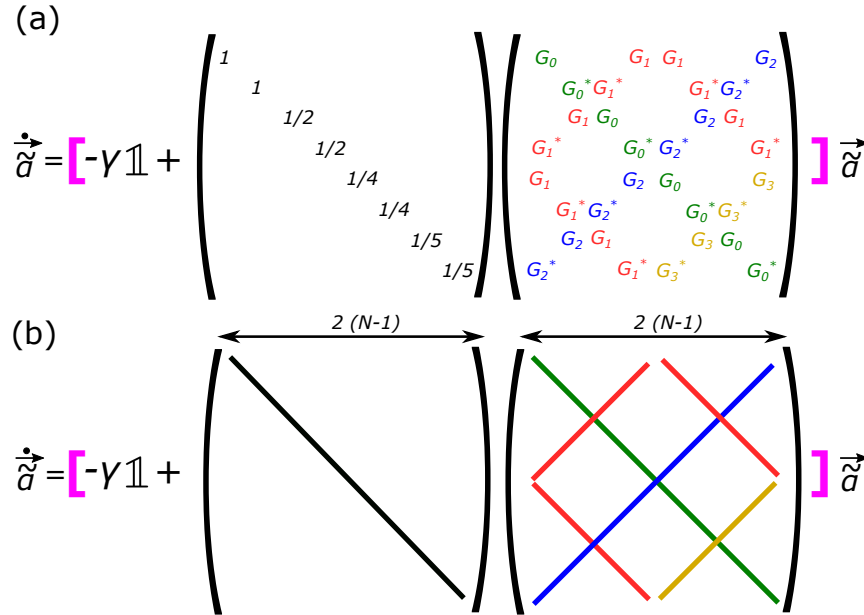

Figure 5.5: (a) The matrix construction for the $N = 5$, $V = 3$ case (only non-zero elements are shown). (b) Schematic representation of the matrix equation for the case of $N = 2V - 1$. The colours indicate the form of the elements following (a).
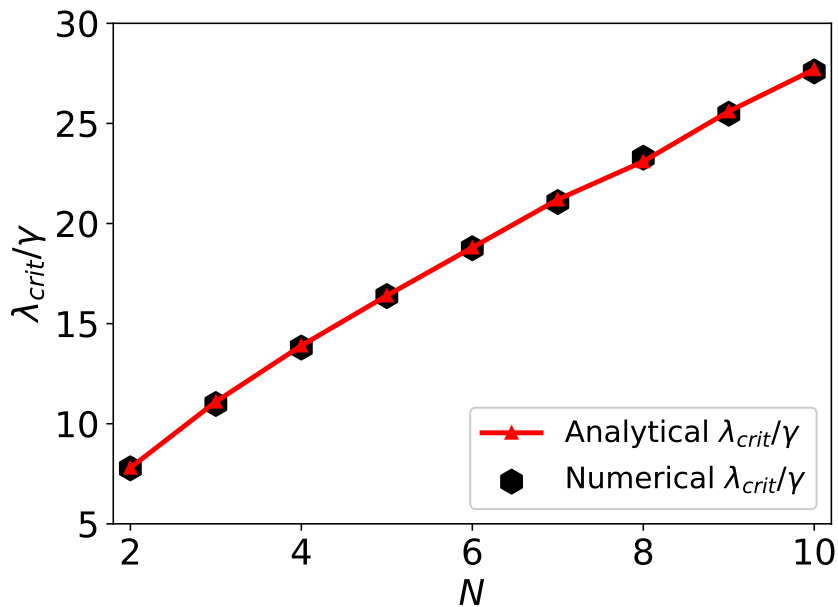
Figure 5.6: A comparison of the theoretical λ_{crit}/γ for a system driven at a voltage that follows the relationship $V = 2N - 1$ (red line) and the numerical calculation of the same value from numerical integration (black hexagons) showing a very close agreement. For these calculations the loss was taken to be $\gamma = 1/30$.

shown in Fig 5.6 along with the numerically calculated λ_{crit}/γ for the corresponding integration. From Fig 5.6 it is clear that analytical approach works very well. It also appears that the critical coupling increases approximately linearly with N.

For values of N Between $N = V$ and $N = 2V - 1$, a transition is not found at all using this approach, or at a coupling much higher than seen thin an integration. This is because the transition that are seen in the integration are not continuous. The case where $N = V$ is an interesting case, and we will now turn to look at it in detail.

5.3.3   The Special Case of $V = N$

In the previous calculation we presented a calculation that could tell us if, and when, the system's off resonant modes become strongly excited, but in the final stage the matrix eigenvalues must be numerically calculated. However, there is a special case of this calculation where the condition for this can be explicitly shown. That is the case of $N = V$.

Before we can discuss $N = V$, however, we must address how analytical equations can be formed for systems in the range of $V = N$ to $2N - 1$. It turns out that this is actually a relatively simple

procedure which involves dropping the bottom rows and right-hand columns from the matrix M. So for example for $V = 2N - 2$ we would simply drop the bottom two rows and the right most two columns, and so on. However, this procedure cannot be repeated ad infinitum and can only take us up to the limit of $V = N$ as beyond there is no resonantly driven mode.

In the case of $N = V$ the matrix reduces to the upper left corner of that presented in Fig 5.5 and simply forms an X structure, the only non-zero terms are on the diagonal and the anti-diagonal. For matrices with this structure the determinant, and thus the product of the eigenvalues, can easily be determined any is given by[3],

$$\text{Det}(M) = \prod_{k=1}^{k=V-1} \left[\left(-\gamma + \frac{G_0}{(V-k)} \right) \left(-\gamma + \frac{G_0^*}{k} \right) - \frac{|G_1|^2}{(V-k)(k)} \right]. \qquad (5.33)$$

When the system loses stability this determinant must pass through zero, showing one of the eigenvalues has switched signs. It can be shown that $G_0 = 0$ for all λ such that the resonantly driven mode does not itself undergo a bifurcation. Hence, we can say that the determinant first becomes zero when the $k = 1$ term is zero. This occurs when,

$$0 = \gamma^2 - \frac{|G_1|^2}{V-1}, \qquad (5.34)$$

and thus the full condition for the transition to occur, is given by.

$$\frac{\lambda}{\gamma} > \frac{2\sqrt{V-1}}{J_1'(A_V)}. \qquad (5.35)$$

This result leads to two interesting features. Firstly, there is no solution to this condition for $N < 6$, thus for $N = 2 - 5$ the zero amplitude solution never displays a destabilisation and will transition discontinuously. However, $N \geq 6$ will display a destabilisation and thus will undergo a continuous transition.

Secondly, it is simple to show that for all cases for $N > 5$ that this system will not just satisfy this condition only once, it will be satisfied by two different values of λ. The logical interpretation of this is that the solution will smoothly move away from the origin, reach some maximum amplitude

---

[3]The structure for equation (5.33) is particularly un-intuitive so let's take a second to unpack how we get to it. For any matrix, if we swap any two rows or columns we change the sign of one of the eigenvalues of the matrix, however, since we are only concerned about when one these is zero we are free to swap rows and columns without consequence. Because of this, we can rearrange X shape matrix to have a block diagonal structure (i.e. the diagonal is composed of 2×2 blocks) whose determinate is just the product of the eigenvalues of these blocks.
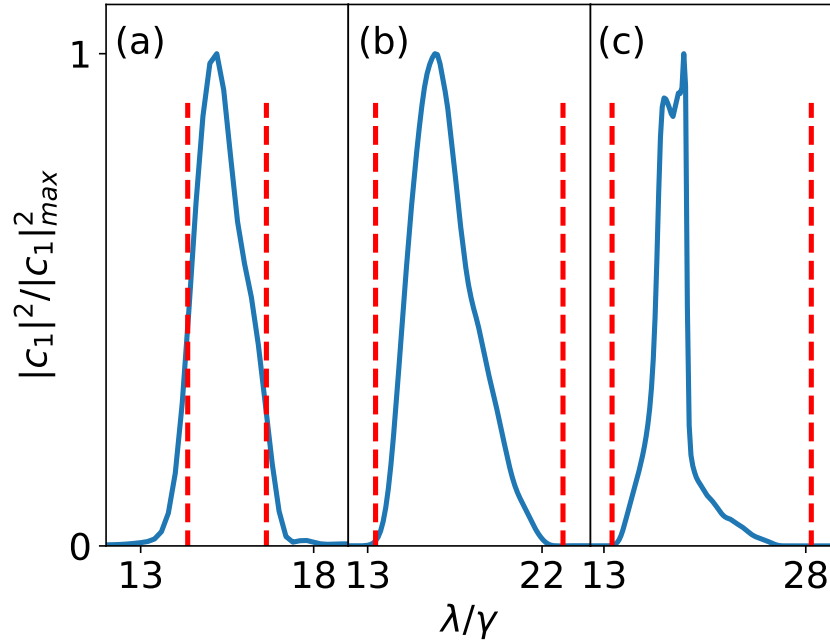
Figure 5.7: $|c_1|^2/|c_1|^2_{max}$ obtained from numerical integration for (a) $N = V = 6$, (b) $N = V = 7$, and (c) $N = V = 8$ (blue) and the predictions for the symmetry breaking events and recombination events (red dashed) obtained from 5.35. Here $\gamma = 1/30$ in each case.

and then be drawn back to zero. Thus, the system will undergo a discreet time symmetry breaking transition and then, at a stronger coupling this will reverse, with the system returning to a drive locked regime. This re-entrant behaviour is shown in detail in Fig 5.7. Note that, while the transitions shown for $N = 7$ and $N = 8$ are very well bounded by the theoretical destabilisation and re-stabilisation values given by equation 5.35, $N = 6$ appears to destabilise well before and re-stabilise well after the prediction. This is simply because the $N = 6$ destabilisation is very weak, with $|c_1|^2_{max}$ being very small compared to the $N = 7$ and $N = 8$ cases. Note that the slightly strange shape of the $N = 8$ curve shown in Fig 5.7 originates from the system having not fully settled down into its steady state oscillations for the chosen integration length at those values of λ/γ. This small numerical error does not affect the destabilisation and re-stabilisation points shown.
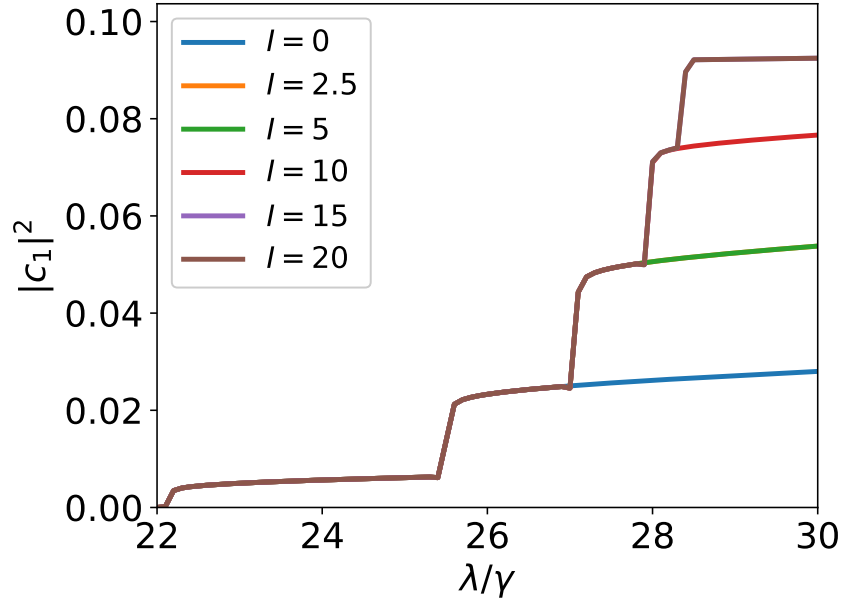
Figure 5.8: A demonstration of the multiple simultaneous stable fixed point solutions that the system can occupy for a given parameter set ($N = 10$, $V = 2$, and $\gamma = 1/30$) depending on the amount of energy that is given to the system at the beginning of the integration. Note that some of the solutions, namely $I = 2.5$ and $I = 15$, are present in this graph but follow the same trajectory as $I = 5$ and $I = 20$ respectively and are thus covered completely by them.

5.4 Discontinuous Transition

So far we have discussed the cases where the analytical calculations have led to solutions where the origin becomes smoothly unstable, and the system displays continuous transitions, $N = 1$ $V = 2$, $N = 3$ $V = 2$, and $V = 2N - 1$. However, this leaves the question of what happens when these solutions are not forth coming, for example in the case of $N = 2$ $V = 2$, or for the regime $V = N$ to $V = 2N - 2$ discussed above? With only a few exceptions[4] when the equations for these are solved it is found that $\alpha_1 = 0$ never destabilises. However, At some point we do know that these systems can undergo symmetry breaking and no longer be drive locked, undergoing a discontinuous transition. This implies the existence of multiple, simultaneous, stable, fixed point solutions existing within the system's parameter space.

The idea of simultaneous stable fixed points existing in the system is not a new one and have been seen extensively in similar JJ cavity systems. In fact, we can easily observe them in this

---

[4]The exception is $V = N$ for $V > 5$ see subsection 5.3.3

system by changing the initial energy that the system is given within the numerical integration[5].
Fig 5.8 shows a system with $N = 10$ which was initiated with multiple different initial conditions
(parameterized by a quantity I), corresponding to giving the system different amounts of starting
energy. This clearly shows that multiple different stable fixed points can coexist in the same
parameter ranges. Thus, it is not unreasonable to extend this to the idea that stable fixed points
will coexist with a stable $\tilde{\alpha}_1 = 0$ solution.

In fact, the idea that stable fixed points can simultaneously exist while $\tilde{\alpha}_1 = 0$ remains stable
actually complicates things when working with this system. To understand this, we must reconsider
the definition of the discrete time symmetry breaking transition in systems with a discontinuous
transition. Previously we have discussed the transition as if it occurred at some set value that is
fixed for a given system, and in the case of continuous transitions this appears to be the case. There
is no analytical value of λ_{crit} that can be determined for discontinuous transitions. Instead, we
find there is a minimum value of λ at which these transitions can take place, a value of λ at which
we are injecting enough energy to overcome the loss and thus have the possibility, but not always
depending on the amount of energy the system starts with, to move the system into a different
fixed point solution.

The practical problem is thus to try and identify when stable fixed points for which the funda-
mental mode amplitude is non-zero first emerges in regimes where the zero amplitude state co-exists
with other stable solutions. To address this in our calculations we introduce two techniques when
dealing with discontinuous transition systems[6]. Firstly we acknowledge that if there are many
simultaneous stable fixed points that the system can sit in then initiating the system near one will
increase the probability of the system remaining in that fixed point. As such, we use a technique
we call integral regression to ensure that the system is initiated close to a non-zero fixed point so-
lution. This technique is simple but powerful and is necessary to see the correct values of the λ_{crit}.
Secondly, the system is initiated with many different initial conditions (in a way that is compatible
with the integral regression), normally at least $5 - 10$ different values, and the lowest value of λ at
which the long time value of $|C - 1|^2$ collapses to zero is taken as the critical one[7]. While these

---

[5]Initial conditions in these systems are somewhat ill-defined as when we set up a system we can implement any
number of initial positions and velocities. For clarity, when we talk about an initial condition in the main text by
a single number, i.e. $I = 5$, for a system with a set number of modes me mean that the system was initiated with
each mode at a position of I/N and with zero velocity.

[6]These techniques can also be used on continuous systems and will yield the same results, but they are just not
necessary.

[7]If an integral regression was used to calculate the dynamics, the first integration would be the only one initiated

methods do require a fair amount of trial and error and begin to become challenging for higher N, however, they were found to be sufficient for the work presented here.

Another question raised by the existence of simultaneous fixed points within the dynamics of the system is if this behaviour is indicative of a road to chaos? The short answer to this is no, at least for the parameter space explored within the scope of this chapter. Chaotic behaviour has been observed within Josephson systems before, however, what we find is a single change in frequency, rather than a sequence of period doubling transitions leading to chaos that has been observed in related oscillators. This is more to do with the dominant process switch that is observed in superharmonically driven systems (see 3). That is not to say that the system cannot become chaotic, only that it is not observed in the parameter range studied in this thesis.

5.5 The General Dynamics of a JJ Laser with Integer Drive

In section 5.3 we discussed several specific cases of the system where we have chosen N and V carefully such that we can apply approximations to the system. However, in doing this, we have only presented a limited subsection of the possible behaviours. In this section, we will move beyond these limited approximations and ask the question: what is the general behaviour of the system when we drive it at an integer V, and can we relate the results to the analysis developed in the previous sections to get a more generalised description?

5.5.1 The Case of $V = 2$

We begin by examining the simplest, non-trivial, case of the system dynamics, $V = 2$. The threshold dynamics of the $V = 2$ driven system is shown in Fig 5.9 where we have plotted $\lambda_{\text{crit}}/\gamma$ against the number of modes in the system N. It is clear that as N is increased the system settles into an alternating pattern of λ_{crit} values, ultimately forming two linear relationships, one for odd values and one for even values.

The odd values require the least couplings to undergo the transition and when they do, it is with a continuous behaviour. This agrees with what we observed in the analytical approximations, as it was shown that both the $N = 1$ and $N = 3$ cases underwent a continuous transition for $n = 2$.

---

with the initial values.
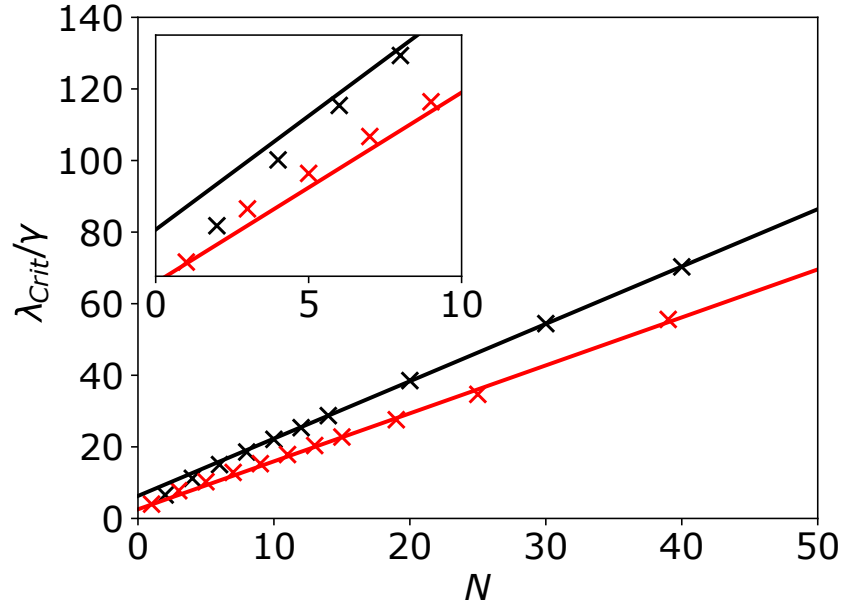
Figure 5.9: The λ/γ critical thresholds for odd N (red crosses) and even N (black crosses) as N increases with $V = 2$. The trend lines are fitted from the 5th point onward to represent the fact that the data tends to a linear relationship. For all these simulations a loss of $\gamma = 1/30$ was used.

The even N values require stronger coupling to undergo the transition, and when they do, they undergo a discontinuous transition.

For both even and odd N, there is a clear trend towards a linear relationship in N, similar to how the $N = 2V - 1$ relationship was very close to linear. However, this is not universal: the inset of 5.9 shows that the even transitions drop off significantly from the linear trend as the values of N tend towards 0.

5.5.2 The Case of $V = 3$

Since the relationship between the N and λ_{crit} in the $V = 2$ case is relatively simple to determine, we may then ask what the more general behaviours are as V is increased. To begin to determine this we first need to map out the $V = 3$ case and compare this to what we have seen for $V = 2$.

Fig 5.10 show the relationships between N and λ_{crit} for the system driven with $V = 3$. Again, similar to the $V = 2$ simulations, the system's responses can be split into three distinct behaviours each of which display a linear relationship. These three categories are split up into modes that fit into the categories of $N = iV - 1$, $N = iV$, and $N = iV + 1$ where i is an integer.

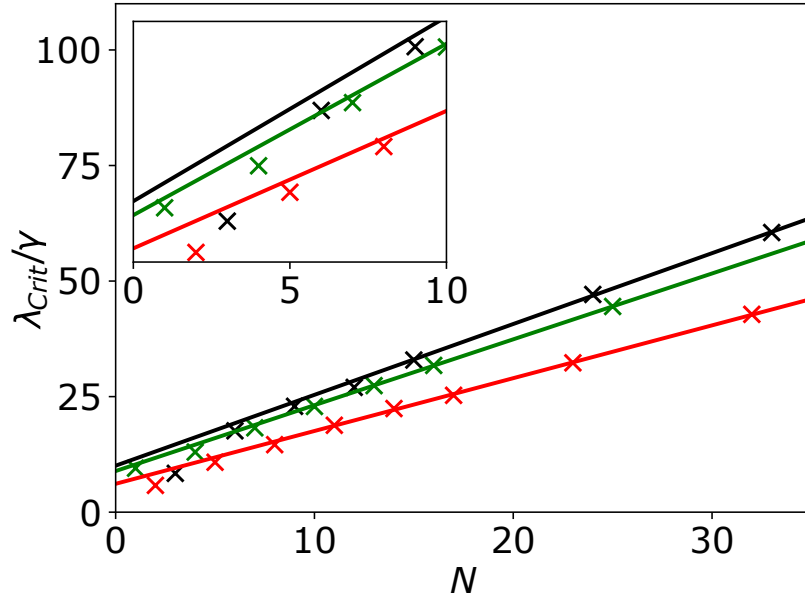Figure 5.10: The λ/γ critical thresholds for $V = 3$, which follow three trends: $N = iV$ (red crosses), $N = iV + 1$ (black crosses), and $N = iV - 1$ (green crosses) as N increases with i being an integer here. The trend lines are fitted from the 4th point onward to represent the fact that the data tends to a linear relationship. For all these simulations a loss of $\gamma = 1/30$ was used.

For the case of $N = iV - 1$, shown as green crosses in Fig 5.10, we observe a continuous transition. This is not all that surprising as again in the previous analytical sections we showed that the case of $V = 3$, $N = 5$ has a smooth transition which is found in this class. The cases of $N = iV$ and $N = iV + 1$ again show distinct linear trends, separate from each other, and also both show discontinuous transitions. Just like in the $V = 2$ case there is a notable drop-off from these linear trends as N approaches zero, see Fig 5.10 inset, though in this case it is quite clear that this only affects two sets of points that display discontinuous transitions ($N = iV$ and $N = iV + 1$).

It would appear then that the $V = 2$ case is not a unique one, and that the different behaviour of the odd and even values of N are in fact a special sub-case of a more generalised behaviour of the system. That behaviour is that for a given integer V, there will be V distinct linear trends of λ_{crit} values produced, depending on how N relates to V.

5.5.3 The General Dynamics under Integer Drive

It is tempting to predict a general trend based on the $V = 2$ and $V = 3$ cases that we have explored in detail. We would anticipate that different N values would follow V different linear trends, though

falling off at low N. For the case where $N = iV - 1$ a continuous transition would be expected, with a discontinuous transition elsewhere. However, we know that not one, but two continuous transitions emerge for $N = V$ when $N > 5$, this suggests that a more complex picture is in fact likely to emerge as V is increased than is initially suggested by simply examining the $V = 2$ and $V = 3$ cases. However, without detailed study of more V values, it is unclear what exactly this behaviour is.

5.6   Realistic Loss Structure

So far we ave discussed the case where the mode's quality factor, Q, scale with the mode frequencies, leading to a simple case where γ is the same for all modes. This is an appealing case for theorists as it can generally make analytic calculations much easier, eliminating the need for summations over mode loss terms in analytical calculations, and making the dynamics in each mode comparable. However, it is naive to assume that this is a model that can accurately represent real systems.

It is not unreasonable to make the judgement that the higher frequency modes should have a higher rate of loss and this has been experimentally confirmed [83] with a relationship that goes as,

$$\gamma_n = n^2 \gamma_1 \tag{5.36}$$

where γ_n is the loss in the nth mode and γ_1 is the loss in the lowest mode. This is the loss experienced specifically in a co-planar waveguide in situations where the loss is dominated by couplings to eternal circuitry, which is what is used to construct the cavities which the Josephson junction is embedded in[31]. However, different device architectures may well yield different relationships.

One consequence of Equation 5.36 is immediately obvious. As we increase the number of modes, the influence the higher modes will have on the dynamics of the system will quickly begin to diminish. This is because as more modes are added to the system there loss increases with n^2 thus the actual time the photons spend in the mode and thus are able to influence the system's dynamics, or from a quantum mechanical point of view the amount of time they are able to provide stimulated emission, is minimised. For sufficiently high indexed modes, this loss will become so fast that they in fact have a negligible influence on the system.

Fig 5.11 shows a $V = 2$ system which has loss rates given by Equation 5.36 for its modes.
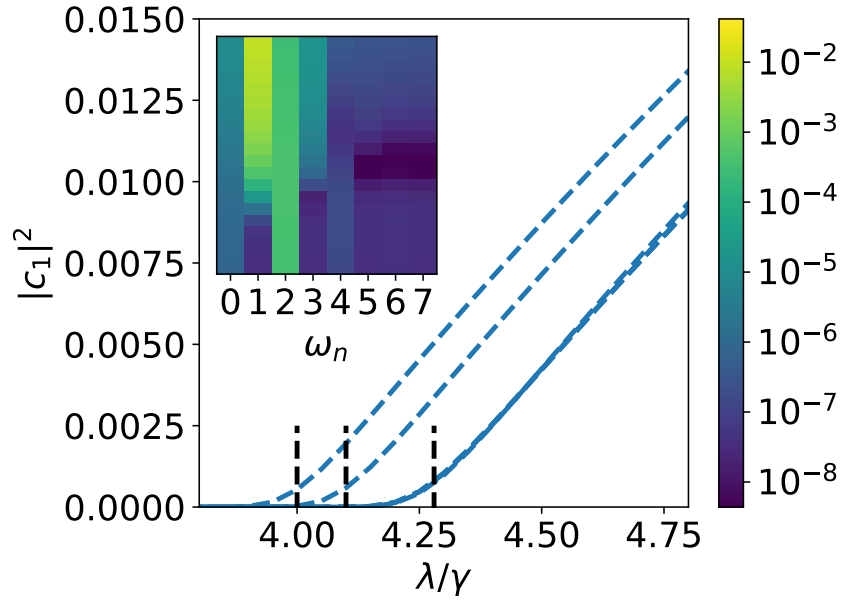
Figure 5.11: $|c_1|^2$ Fourier component for a system with $V = 2$ and a quadratic loss structure given by equation 5.36. The lines move from low mode number $N = 1$ on the left to $N = 6$ on the right. The overlapping solutions show converge for $N \leq 3$. The analytical predictions for each of these cases up to $N = 3$ are shown by the black marks. Inset: The Fourier component on a log scale of each integer mode for a simulation with $N = 6$ over the same range of drives on a log scale. Here $\gamma_1 = 1/30$

For this case, it is clear that the transition point for the $N = 1$ case has not changed, as the fundamental mode loss rate is unaffected. However, for all subsequent N, there is a significant change in behaviour. It quickly becomes apparent that two things are true when dealing with realistic mode loss.

Firstly, that the above assumption about the decreasing mode influence is indeed correct, with each subsequent added mode having less influence on the system. This manifests as a rapid convergence in the location of the transition: modes with $n > 3$ have almost no influence on λ_{crit}. Exactly how many modes are likely to be relevant will of course depend on γ_1, but there will always exist a cut-off beyond which higher modes become irrelevant.

Secondly, It becomes very clear that mode dependent damping destroys the pattern of continuous-discontinuous transitions that occurs as you add modes to the system with a uniform loss in each mode. A mode dependent damping changes the analytic calculations described in Chapter 5.3. Indeed, this approach now yield predictions for the transitions for $V = 2$, $N = 2$ and $N = 3$ which are now both continuous.

5.7 The Symmetry Breaking Characteristics of a Laser Driven at $V = 2.5$

So far we have always assumed that the voltage is an integer multiple of the fundamental mode frequency, but now we will consider the case where this is no longer true. For non-integer V none of the modes is resonantly driven, and the analytic approach developed in section 5.3 no longer applies, but we can of course use numerical integration to explore the behaviour.

To begin to explore the case of the system driven at non integer V, we chose to examine the case when the voltage is chosen such that the system is driven at a half integer value. Specifically, we choose the value of $V = 2.5$. The reasoning behind this is fairly simple, although there is no direct resonance present, we still have rational ratios of frequencies, i.e. $5V = 2\omega_0$, and hence we expect that higher order nonlinear terms will still be able to generate excitation in the system.

When the system is driven at $V = 2.5$, just like in the previous section, we first observe a regime of the dynamics where the system's oscillations are locked to integer multiples of the drive frequency (See the lower half of Fig 5.12). However, as opposed to the cases presented in the previous sections
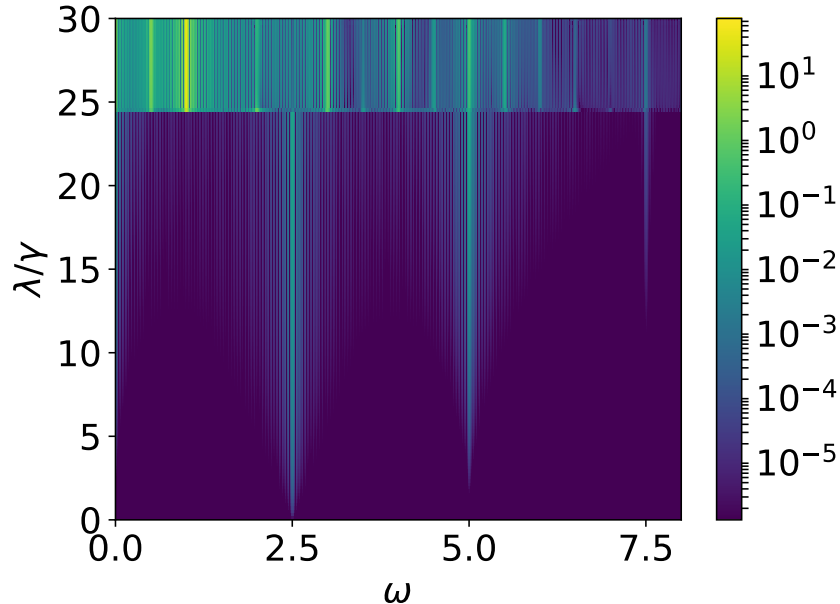

Figure 5.12: The average value of the Fourier component $|c(\omega)|^2$ for a given frequency ω as we vary λ/γ for a system driven at a non-integer drive frequency, $V = 2.5$. Each simulation was completed with a system of equations that have five modes, $N = 5$, and a dissipation of $\gamma = 1/30$

this involves responses at frequencies that aren't a natural frequency of any of the modes, thus we must conclude that these off resonant oscillations will not be contained wholly within one mode but distributed amongst many modes all as a result of off resonant excitation.

Just like the previous sections, the system undergoes a transition, however, in this case the nature of the transition becomes somewhat less well-defined. Previously, we described the transition as when the system moves from a drive locked regime to one where all modes are strongly excited (including, in particular, the fundamental one). However, in the case of non integer drive we must amend this to include a new caveat, that it is not simply just all of the modes that are strongly redexcited, instead we see all combinations of the natural frequencies and the drive frequencies. So for example, in the case of redFig 5.12 it can be observed that, for a sufficiently large λ, all integer and half integer frequencies of the system become excited.

Conceptually, this makes a lot of sense, when we expand the drive term in Equation (2.12). If the drive frequency is a half integer, we can easily see that this will combine with all terms that oscillate at integer frequencies to give a range of half integer frequencies. However, this will only happen if the system is already excited at a range of frequencies, thus it only happens after the system has undergone the transition.

While the case of half integer V does share some features with its integer counterpart, there are some behaviours that don't align. For example, it appears that no matter the number of modes the transition is always discontinuous. Naively, we may have expected that for a half integer voltage we could still apply the idea that $N = iV - 1$ would still show a smooth transition, however this is definitely not the case. For $N = 9$, a value which should show a smooth transition if the $N = iV - 1$ rule holds, instead it shows a discontinuous transition. The reason for this deviation is that this prediction is based on a first order RWA, but in this case we have no directly resonantly driven mode and thus a first order RWA should not apply here. Since the $N = 5$ mode could be driven at twice the drive frequency, it is not unreasonable to think that the system may be able to be described by a higher order RWA similar to the superharmonically driven JJ system presented in Chapter 3[33, 73]. However, since the ratio of frequencies is $5 : 2$ rather than $2 : 1$, as it was for the double Cooper pair tunnelling analysed in Chapter 3, it seems unlikely that a simple extension to the second order RWA will be sufficient to capture the relevant dynamics.

This raises the question, if the system no longer follows the $N = iV - 1$ rule, in what other
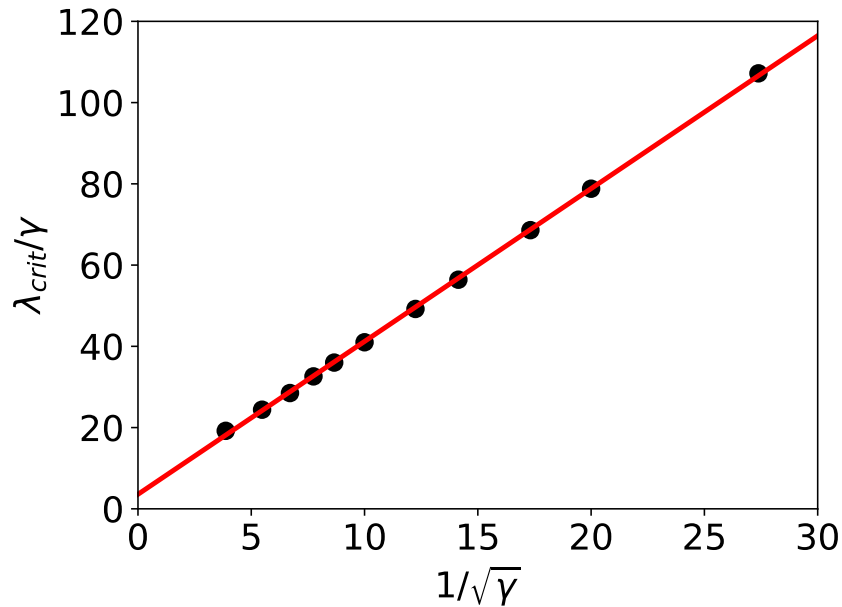
Figure 5.13: The value of λ_{crit}/γ plotted against $\sqrt{\gamma}$ for a system driven at $V = 2.5$ and a range of different γ values (black dots) clearly following a linear fit (red line), as opposed to the integer V case which would lead to a flat line. Each simulation was carried out with $N = 5$.

ways does the half integer driven case differ from the integer V? One of the key observations from the integer drive case is that the critical drive of then transition scales linearly with γ and thus we have chosen to scale the drive by this to eliminate the dependency. This scaling is not followed in the case of half integer drive, as Fig 5.13 clearly shows. The system actually closely obeys a $\lambda_{crit}/\gamma \propto \gamma^{-1/2}$ law.

5.8 Conclusions About the JJ Laser

In this chapter, we chose to examine the case of a JJ laser with only a few accessible modes. We began by showing that, as in the many mode case, for weak driving only modes at multiples of the drive frequency are significantly excited. From this we concluded that the system must undergo a reddiscrete time symmetry breaking event as when we increased the strength of the drive the system was found to lock to the natural frequency of the lowest oscillator.

We showed that this transition could occur in one of two ways, a continuous transition where the system smoothly begins to exhibit oscillations at the natural frequency, and a discontinuous transition where the system very suddenly begins to exhibit oscillations with a substantial natural

frequency component with no connecting behaviour. We developed an approximate analytic model that explained some of the observed features for cases where a single mode is significantly excited below threshold. Expanding around the origin, we were able to predict values for λ_{crit} where continuous transitions took place. The discontinuous transitions were linked to cases where the zero amplitude solution for the fundamental mode never becomes unstable in the approximate treatment. Thus, the discontinuous transition was a result of small-off resonant oscillations in the mode being enough to move the system away from the basin of attraction of the origin to a different stable fixed point that emerges. The continuous transition was a result of the fundamental mode solution with no oscillations becoming unstable and the stable fixed point smoothly moving away from the origin. We also analysed some special case solutions such as when $N = V$, where the system could destabilise and then restabilise.

We explored the evolution of these behaviours systematically as a function of the critical drive for different fixed V. We uncovered linear relationships between λ_{crit} and subsets of N vales. We found discontinuous transitions except for those N that followed the relationship $N = iV - 1$ which show continuous ones, in line with our analytical work.

Next we chose to examine an alteration to the system's loss, where γ was scaled with the square of the mode number, which represented a more realistic representation of experimental conditions. We found that this alteration made the system only ever undergo a continuous transition, and that the critical drive ceased to meaningfully change beyond a given number of modes.

Finally, we examined the case of half integer drive in the low mode regime. We showed that the system still underwent a transition from a drive frequency locked regime, but this time moved to a regime where all integer and half integer frequencies were resonantly excited. In this case, all transitions were discontinuous and did not significantly change when mode modes were added, but the system did display a different dependency on loss compared to the integer V case.

There are lots of ways in which the work in this chapter could be extended. For example, since we have observed two very distinct behaviours of the system at with few modes compared to that seem in chapter 4 for many modes it would be interesting to explore the cross-over dynamics of the system as we move from one extreme to the other: when does the system stop displaying oscillations locked to the natural frequency all together. Additionally, why, in the low N case, is there a very distinct well-defined transition, while in the large N limit this behaviour appears to be transient?

Also, a more detailed exploration of how realistic values of the loss parameters might allow a more detailed understanding of the experimental results obtained by Cassidy et al.[31]. Finally, it would also be interesting to explore the few-mode behaviour in the quantum regime, though modelling would get much more challenging with increasing N.

Chapter 6

Summary and Conclusions

This thesis has explored novel aspects of the quantum dynamics of superconducting circuits, focusing on the coupled dynamics of charges and photons in systems where a voltage biased Josephson junction is coupled to a microwave cavity. Specifically, the work presented here investigated two new features of the behaviour of such systems: the way in which the cavity could completely change the charge transport in the system (giving rise to double Cooper pair tunnelling, chapter 3) and the mechanism by which couplings between multiple modes could give rise to a dynamical transition that breaks a discrete time-translational symmetry (the Josephson laser, chapters 4 and 5). The main results from this thesis have been published[33, 34]. Although the photonic properties of Josephson junction cavity systems have been explored quite extensively in recent experimental and theoretical work (as was reviewed in chapter 2), attention has concentrated on regimes where the behaviour is rather simpler than that described in this thesis. We hope that the ideas presented here will stimulate future theoretical and (especially) experimental work to investigate more of the subtle and complex physics of Josephson junction cavity systems. In the following we review our main findings.

In the opening chapters of this thesis, we reviewed resent work om microwave cavities driven by voltage biased Josephson junctions. Because of the nature of the nonlinear driving elements within these systems, the photonic dynamics observed within the cavity are highly nonlinear when driven with sufficient strength[23–25, 27, 29, 30]. This nonlinear behaviour has been observed by tuning the system to be on resonance: so that the energy from a tunnelling Cooper pair is able

to generate one or more photons in the cavity [7, 27–30]. Analytical descriptions of these systems are challenging to find and limited in scope. In cases of weak driving, perturbation methods such as $P(E)$ theory have been used extensively, as well as semiclassical descriptions of a perturbed cavity[14, 23–26]. For regimes where the system's dynamics are coherent and dominated by a single frequency, RWA descriptions have been used to recover approximations to the full complex dynamics in specific regimes. Despite a significant amount of theoretical and experimental research being carried out to explore behaviour at different resonances, the richness of Josephson junction cavity systems is such that many potentially interesting regimes had not been explored.

In Chapter 3 we introduced the idea of the double Cooper pair resonance, here the novel feature was the complete change in the transport that the cavity gives rise to. The voltage across the Josephson junction is tuned such that the energy of two tunnelling Cooper pairs matches the energy of a single photon in the cavity[33]. It was observed that the system displayed two primary frequency components: the Josephson frequency, and the cavity fundamental mode frequency. The system transitioned from dynamics dominated by the Josephson frequency in the weak drive limit, to dynamics dominated by the natural frequency as the drive was increased. In the case where the cavity frequency dominates, the non-linear equation of motion for the system could be approximated using a second order RWA, unlike previous JJ-cavity systems which only required the use of the first order RWA. This switch from Josephson frequency to natural frequency dynamics was found to be associated with a switch in charge dynamics through the junction, specifically a switch from dynamics dominated by incoherent tunnelling of single Cooper pairs to dynamics dominated by coherent tunnelling of pairs of Cooper pairs, with the coherent dynamics facilitated by back action from the cavity onto the junction. Importantly, it was also found that the system's parameters could be tuned to obtain a photon blockade more easily than had been found previously in this class of systems.

In the rest of the thesis we switch to a second topic: the dynamics of the JJ laser, a device which consists of a voltage biased Josephson junction connected to a cavity that supports a large number of modes (several hundred). Recent experimental [31] and theoretical [32] work suggested that the interplay of nonlinearity and many modes can lead to a transition in the oscillations of the superconducting phase difference in the JJ laser from a periodicity set by the voltage drive (i.e. the Josephson frequency) to one set by the fundamental mode frequency, breaking the discrete

time-translational symmetry of the Hamiltonian. We set out to investigate exactly when and how this transition occurs, an important question left unanswered by previous studies[31, 32].

In chapter 4 we started by exploring the dynamics in cases where the number of cavity modes is very large, using numerical integration to investigate the different types of (classical) dynamics that the system can display. When the voltage was tuned to be an integer multiple of the natural frequency of the lowest mode, the system's collective dynamics formed a sawtooth wave. The frequency of this sawtooth response displayed very complex behaviour, with the system exhibiting four distinct regimes, depending on the strength of the effective drive. The most significant finding was that the system always ended up oscillating at the drive frequency even for very strong drive strengths, set by the Josephson energy, E_J. Regimes in which the system did make a transition to oscillations at the fundamental mode frequency were found, but in each case the behaviour turned out to be a transient with the period always returning to that set by the drive in the limit of sufficiently long times. This was a result that we found somewhat surprising and it is clear that more work will be needed to understand why there is no transition in the period of the long-time oscillations in the system as this drive strength is increased.

In Chapter 5 we then examined the case of the JJ laser in a simpler regime where only a limited number of cavity modes were assumed to be relevant (up to 10, typically). In this case, the system was observed to form an imperfect sawtooth wave, one with a truncated Fourier series, whose frequency depended on the strength of the driving[34]. In the case of low E_J, the system was observed responding primarily at the drive frequency, with only modes with an integer multiple of the drive frequency showing significant excitation, however as E_J was increased all modes begin showing significant excitation and the sawtooth wave underwent a discrete time symmetry breaking transition, oscillating with the period of the fundamental mode. It was shown that this transition could happen in one of two ways, continuous or discontinuous, depending upon the number of modes, N, and the applied voltage, V. It was found that this behaviour could be explained using a RWA which could, in limited situations, predict the Josephson energy required and type of transition a given N and V combination would lead to.

The work in this thesis could be extended in several obvious ways. First of all, the work on double Cooper pair tunnelling in chapter 3 could be extended to consider even higher-order resonances in which three or more Cooper pairs tunnel to generate a single photon. The extremely strong

nonlinearities achievable in devices using current technology are expected to support processes where one Cooper pair generates up to 6 photons at once[30], so working out whether exotic processes involving multiple Cooper pairs tunnel together are observable is a very timely question to ask.

Secondly, the work in Chapters 4 and 5 raises interesting questions even at the level of the classical dynamics of the JJ laser. For example, when and how does the discrete time translational symmetry breaking transition disappear as one increases the number of modes from the few mode regime (studied in chapter 5) to the many mode regime (studied in chapter 4)?

A study of the general quantum description of the JJ laser would be an interesting extension to the work presented here. In particular, the case of the few mode JJ laser. It is currently unclear whether the continuous/discontinuous behaviour would be preserved when quantum effects are considered.

Finally, we comment on the broader potential relevance of our work for future research. The work on double Cooper pair tunnelling could help open up a new area of research, namely the study of charge transport processes and photon production in a range of superconducting devices involving correlated tunneling of Cooper-pairs. We also hope that they will stimulate experimental studies to explore double Cooper-pair tunneling in circuit-QED style devices in the near future.

The work on the Josephson junction laser will hopefully have relevance well beyond this specific system. The study of time translational symmetry breaking effects in many body systems and the time crystalline order that they generate has emerged as an important new focus for research spanning classical and quantum dynamics. Understanding how such transitions can occur within the multiple modes of a superconducting cavity approaches this topic from a fresh direction which we believe is especially timely since experiments on superconducting circuits (circuit QED) are increasingly enabling studies of multi-mode effects.

Appendix A

Low Energy Effective RWA Hamiltonian

In Chapter 3 we quote a low energy approximation of the effective Rotating Wave Approximation Hamiltonian (equation (3.11)) but did not explicitly derive it. In this appendix, we will explicitly derive this equation from the full RWA Hamiltonian, as the method, while not needed for the points made in the main text, is interesting and not particularly obvious.

Consider the full RWA Hamiltonian of the form,

$$H_{\text{eff}} = \hbar \delta a^\dagger a + \frac{\tilde{E}_J^2}{4\hbar \omega_J} \sum_{q=0}^{\infty} \frac{\left[O_q, O_q^\dagger \right]}{(2q+1)}, \tag{A.1}$$

where the operators O_q are defined to have form,

$$O_q =: i^q (a^\dagger)^q e^{-i\varphi} \frac{J_q(2\Delta_0 \sqrt{n})}{n^{q/2}} + (-i)^{q+1} (a^\dagger)^{q+1} e^{i\varphi} \frac{J_{q+1}(2\Delta_0 \sqrt{n})}{n^{(q+1)/2}} : . \tag{A.2}$$

Let's consider the case where $\Delta_0 \ll 1$ and $\Delta_0^2 \langle n \rangle \ll 1$. We can approximate the lowest two O_q operators as,

$$O_0 \approx (1 - \Delta_0^2) e^{-i\varphi} - i\Delta_0 a^\dagger e^{i\varphi}, \tag{A.3}$$

$$O_1 \approx i\Delta_0 a^\dagger e^{-i\varphi} + (-i)^2 \frac{\Delta^2 a^{\dagger 2}}{2} e^{i\varphi}, \tag{A.4}$$

and, using the standard commutation rules for a, $a^\dagger$, and n it is easy to show that,

$$[O_0, O_0^\dagger] = [O_1, O_1^\dagger] = i\Delta_0^3(e^{-2i\varphi}a - a^\dagger e^{2i\varphi}), \tag{A.5}$$

thus giving,

$$H_{\text{eff}}^{(0)} \approx \hbar\delta_0 n + i\frac{\tilde{E}_J^2\Delta_0^3}{3\hbar\omega_J}\left[ae^{-2i\varphi} - a^\dagger e^{2i\varphi}\right]. \tag{A.6}$$

Note that this has not yet shown any correction to the resonant frequency, hence the presence of δ rather then δ'. This is because this is the lowest order approximation required to show the two Cooper pair to one photon relationship.

To derive the frequency shift, we must consider terms up to $\mathcal{O}(\Delta_0^4)$, which meand that we also need to includ terms from O_2. The expressions for each of the operators then become,

$$O_0 \approx (1 - \Delta_0^2)e^{-i\varphi} - i\Delta_0 a^\dagger e^{i\varphi} - i\frac{a^\dagger\Delta_0^3}{2}, \tag{A.7}$$

$$O_1 \approx i\Delta_0 a^\dagger e^{-i\varphi} + (-i)^2\frac{\Delta_0^2 a^{\dagger 2}}{2}e^{i\varphi} + i\frac{a^{\dagger 3}}{6}, \tag{A.8}$$

$$O_2 \approx \frac{-\Delta_0^2 a^{\dagger 2}}{2} + i\frac{a^{\dagger 3}\Delta_0^3}{6} \tag{A.9}$$

and, after working through the relevant commutation relationships and dropping irrelevant terms, i.e. ones whose Δ_0 power is greater then 4, we get the final approximate Hamiltonian ((3.6) in the main text),

$$H_{\text{eff}}^{(0)} \approx \hbar(\delta + 8\tilde{E}_J^2\Delta_0^4/(15\hbar^2\omega_J))n + i\frac{\tilde{E}_J^2\Delta_0^3}{3\hbar\omega_J}\left[ae^{-2i\varphi} - a^\dagger e^{2i\varphi}\right]. \tag{A.10}$$

Appendix B

Example Code Used to Calculate CPT Dynamics

A principal property of the Josephson junction cavity system is the transition from incoherent Cooper pair tunneling to coherent Cooper pair tunneling. Showing this process in the photon distribution is fairly trivial possess as calculation of the photon Fano factor, F_n is as simple as calculating,

$$F_n = \frac{\langle n^2 \rangle - \langle n \rangle^2}{\langle n \rangle},$$ (B.1)

and finding the time average. This is how the inset in figure 3.5 is calculated. However, showing the same anti-bunching effect in the charge current however is a non-trivial task.

In this appendix we will detail first the mathematical definition of the current noise which we want to calculate and then a method which to calculate this numerically with a degree of accuracy along with a set of example code written in Python 3.

B.1   The Definition of F_{CP}

To measure the distribution of the Cooper pairs in the system we must consider the current fano factor which is defined by,

$$F_{CP} = \frac{S_{CP}}{(2e\langle I_{CP} \rangle)},$$ (B.2)

where S_{CP} is the current noise, which we define as,

$$S_{CP} = 2Re \int_0^\infty d\tau \langle I_{CP}(t+\tau)I_{CP}(t)\rangle - \langle I_{CP}(t+\tau)\rangle\langle I_{CP}(t)\rangle. \tag{B.3}$$

The actual interpretation of these correlation functions is not a trivial but can be shown to be defined as,

$$\langle I_{CP}(t+\tau)I_{CP}(t)\rangle = \text{Tr}[I_{CP}(t+\tau)e^{\mathcal{L}\tau}I_{CP}(t)\rho_{ss}(t)], \tag{B.4}$$

where $\rho_{ss}(t)$ steady state density matrix of the system.

B.2 Calculating F_{CP} for a System with No Steady State

In our case the system has no steady state due to its explicit time dependence, therefore, we must consider a alternative method to calculate a time average current noise. Instead we consider a steady state cycle composed of discreet points which evenly span one full period of oscillation, $\rho_n^{(0)}$, these are associated with a set of evenly spaced time points, t_n[1]. We will then take an average over this full period, T, using the expression,

$$\bar{S}_{CP} = \frac{1}{T} \int_{t_0}^{t_0+T} S_{CP}(t)dt \tag{B.5}$$

which should then be a good measure of the time average Fano factor.

The first step is to integrate to find the set of initial density matrices, $\rho_n^{(0)}$. This is done using a integration of the master equation just as if we were calculating any other expectation value, then the final point of the cycle is used to extract a set of $\rho_n^{(0)}$. However, due to the fact that S_{CP} is a lot smaller then most other useful expectation values we find it is a lot more sensitive to the starting matrices accuracy, thus the integration must be very accurate.

Since the integration to find $\rho_n^{(0)}$ can be extremely long for it to be as close to a repeating oscillatory state as possible, it is tempting to define the t vector to simply be the number of oscillations required, say 12,000 for sake of argument, and then chose a number of points per oscillation to get a accurate integration, say 40, and then find the number of point required in this vector, 580000 in this case. This will give accurate answers for many time averaged quantities such

---

[1]This is a important point as often, if not explicitly specified, a numerical integration algorithm may over sample parts of the integration it considers complex, leading to non even t_n.

as $\langle n \rangle$ but is actually not accurate enough for S_{CP}. We find $\rho_1^{(0)}$ is slightly after the start of the cycle so that $\rho_{40}^{(0)}$ is precisely at the end. This is a very small difference, small enough that the averaging in most computational methods will smooth it out particularly if done over many cycles like we have, however, S_{CP} is a very small quantity and, due to computation time of each point in the cycle, we only intend to average over a single cycle it cannot be ignored in the calculation of S_{CP}. Fortunately, the fix is a simple one, we simply perform the initial integration over the required number of points with a additional point at the end, i.e. 580001 points. This allocates zero a specific point and then the average will be done over a 41 point cycle with the first point of the last cycle being shared as the last point of the previous one. This will give a perfect average over a single system cycle with no effective 'drift' in point position.

The first true step in calculating S_{CP} the is to calculate $\langle I_{CP}(t+\tau)I_{CP}(t)\rangle$. We do this by first finding the new initial condition for the integration defined by, $I_{CP}(t_n)\rho_n^{(0)}$, and then integrating the Lindbald equation, starting at t_n, until it has settled back into a steady state. The accuracy of this calculation is paramount and, if set too low can throw off the entire calculation by several orders of magnitude. Increasing the number of points per system cycle, setting the integrator tolerances, and increasing the intermittent steps of the Runge–Kutta methods was found to be effective in this. If, when the pre-integration S_{CP}, is calculated, the oscillation loos like two overlapping, exponentially decaying, oscillations, the integration was not accurate enough and should be reattempted.

It is important to note that Qutip (the Python 3 toolbox used for these calculations[76]) cannot integrate with time arrays that don't start with zero. This is not normally a issue but in the case presented above, with a time dependent Hamiltonian, it is necessary to start the integration in the same step that it ended. As such we found it use full to define a new Hamiltonian for each $\rho_n^{(0)}$ with a phase shift intruded to the time dependent terms, ϕ_n, to shift the Hamiltonian so it can be started at $\tau = 0$. This phase shift can also be a nice way to ensure that $I_{CP}(t_n)$ is correct[2].

Finding $\langle I_{CP}(t+\tau)\rangle\langle I_{CP}(t)\rangle$ is significantly simpler, using the normal definitions, $\langle I_{CP}(t_n)\rangle = I_{CP}(t_n)\rho_n^{(0)}$. $\langle I_{CP}(t+\tau)\rangle$ is simply the expectation at each point of the integration over τ when we have initial condition $\rho_n^{(0)}$. Practically speaking we can consider this in one of who ways; Firstly, by performing a new integration over τ and finding the expectation value at each point or, if the second integration has the same number of points per cycle as the one to find $\rho_n^{(0)}$, simply stitching

---

[2] The specific accuracy checks were as follows. The absolute tolerance of the integrator was set to 10^{-14} while the relative tolerance was set to 10^{-12}. The number of points in the system periods was increase from 40 to 200. Finally, the number of Runge–Kutta intervals was increased from 1000 to 5000.

together $\rho_n^{(0)}$ into a array the same length and then finding the current expectation. We elected for the second method simply because we were increasing the number of points in the second integration.

Evaluating equation B.3 is now just a simple matter of numerically integrating the resulting vector when we find the difference between the two values. For this a simple trapeze method algorithm sufficed, giving a set of points $S_{CP}(n)$. Using the same method equation B.5 can be evaluated to find a time averaged S_{CP} that can accurately predict F_{CP}.

Figure B.1 shows the results of this algorithm when applied to both the non RWA time dependent system and a system which has had a RWA performed on it, though the second used a algorithm with no time averaging. We can separate figure B.1 into a 3 distinct regions; The low E_J failure, unification in the incoherent tunneling, and the coherent tunneling.

In the fist regime the RWA simply predicts that $F_{CP} = 2$, which is indicative of incoherent Double Cooper pair tunneling which is the starting assumption of the RWA calculation. At first glance the non RWA appears to contradict this, however we are quick to remember that the non RWA calculation includes single Cooper pair possesses as well, which means that the drop could be explained as the combination of the F_{CP} for the single and double Cooper pair tunneling processes. Naively, we also might think that, because of the presence of the single Cooper Pair process, in
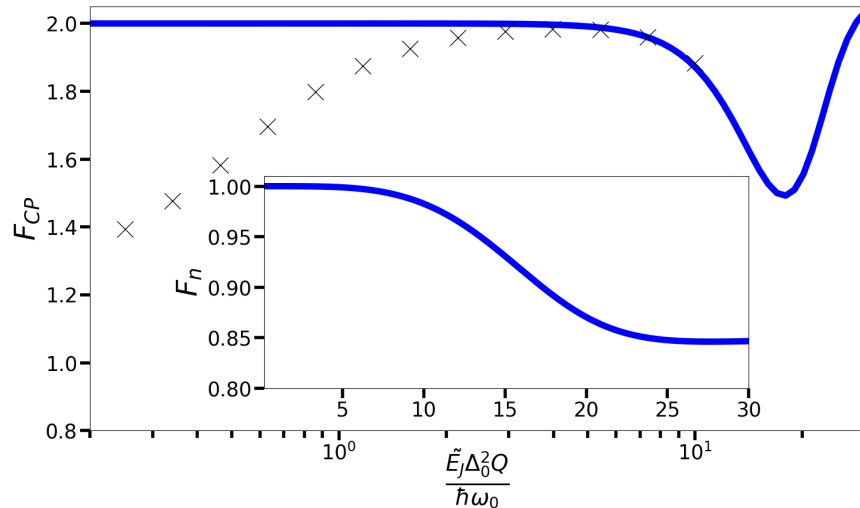

Figure B.1: **Main**: The Cooper pair Fano factor calculated for the RWA Hamiltonian (Blue) and the Time averaged calculation for the full Hamiltonian (Black) against the unified scale drive. **Inset**: The photon Fano factor over a similar scale showing that the prediction of squeezing happens alongside the drop in F_{CP}. The parameters used were $\Delta = 0.15$ and $Q = 1500$.

the limit of $E_J = 0$, $F_{CP} = 1$ however it is notable larger then this due to the presence of the far resonance term, similar to the current ratio.

The second two regimes are much easier to interpret. In the E_J regime when both curves unify at two the two Cooper pair process is dominating and all tunneling is incoherent, i.e. two Cooper pairs tunnel and create one photon. In the final regime, this begins to drop, implying that more photons are produced than pairs of Cooper pairs. This is due to coherent tunneling in the cavity and back action into the junction.

Like all quantities calculated under the RWA we know that the curves should unify under $\tilde{E}_J \Delta^2 Q / \hbar \omega_0$. In fact we see that the RWA calculations do unify under this scaling as shown in Figure B.2. The Non-RWA calculation also initially starts as unified however 2e would expect, as we push further into to the regime where the single Cooper pair process would be more present, there would be subtle deviations dependent on the parameters. This is also visibly present as we approach the limit of $E_J \rightarrow 0$, this is once again the fact that the single Cooper pair process is more dominant here though we would expect to it to tend to the same value at $E_J = 0$.
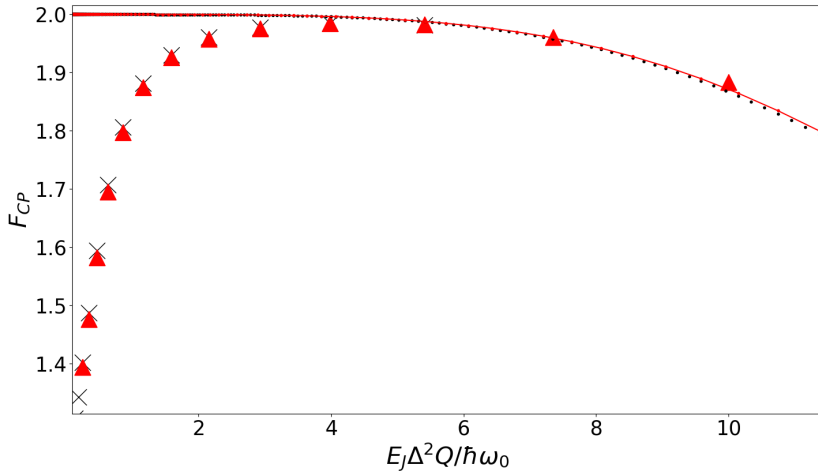
Figure B.2: A comparison of the F_{CP} calculations for $\Delta = 0.15$ and $\Delta = 0.25$ showing the unification under the factor $\tilde{E}_J \Delta^2 Q / \hbar \omega_0$. The RWA curves show very good agreement, $\Delta = 0.15$ (black dots) and $\Delta = 0.25$ (Red dotted line), with slight deviations at higher drives possibly due to different background parameters used such as system size. For the non-RWA calculation, $\Delta = 0.15$ (black crosses) and $\Delta = 0.25$ (Red triangles), we see very good agreement in the regime when two Cooper pairs dominate but as we track back towards $E_J = 0$ we see slight deviations due to the single Cooper pair process not scaling in the same manor.

Figure B.3: F_{CP} for $E_J\Delta^2 Q/\hbar\omega_0 = 3$ showing convergence on a value as the time scaling is increased in the $\tau = 24000$ integration length.

Figure B.4: F_{CP} for $E_J\Delta^2 Q/\hbar\omega_0 = 10$ showing convergence on a value as the time scaling is increased in the $\tau = 24000$ integration length.

B.3 Ensuring the Accuracy of the Calculation.

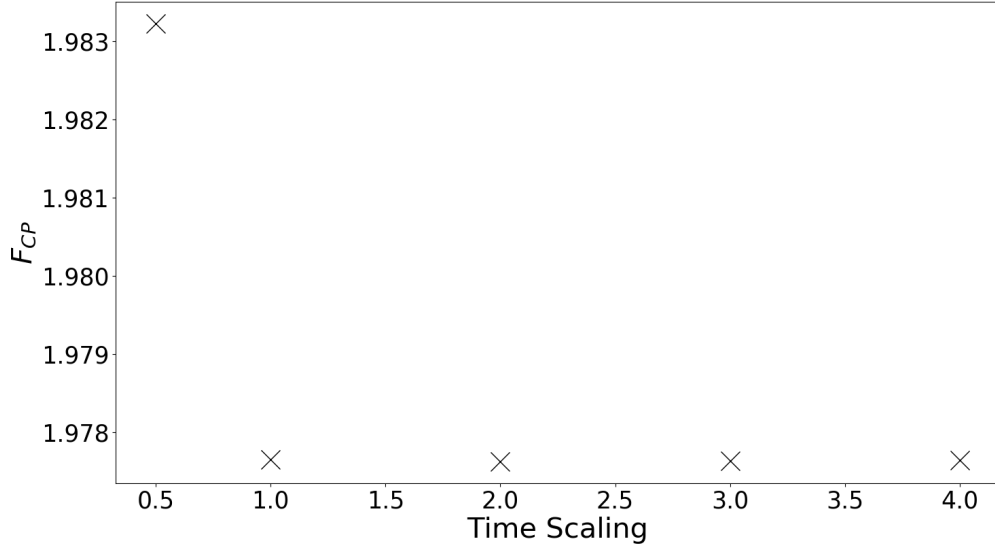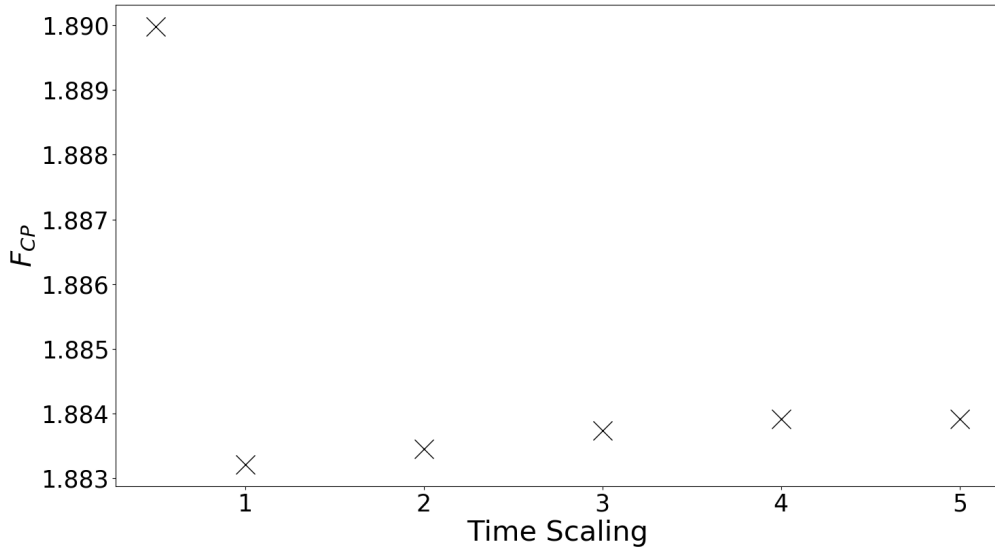A key part of this calculation is ensuring that the numerical calculation is done accurately and showing that this is in fact the case. The lack of analytical expressions for comparison complicates the matter. Because of this we must instead take a iterative approach to checking the accuracy, looking at a spread of different parameters and showing that the set we have chosen are in the region where there is little or no change.

There are two physical parameters that are of interest here, firstly the time of integrating ($\tau = 24000$ in the main text), and the number of Fock states used by qutip (either $N = 4$ or $N = 10$ depending on the drive in the main text). The reason for these two parameters being the primary ones of interest is because of the role that they play in finding the steady state oscillation for the system. We know that the JJ-cavity system is a very slow moving system, so when the numerical simulation is started, the oscillations take a long time settling down into their eventual steady state. Thus, if the integration is too short, it is highly likely that the oscillations will not have reached their final true value. This is particularly important for a ratio such as F_{CP} where even small changes to the $\langle n \rangle$ calculation can cause significant deviations in the F_{CP} value. In the case of system size, N, we wish to try and emulate a harmonic oscillator with an infinite system size. This is impossible, so we need to truncate the state space in such a way to limit the calculation complexity but to have enough states to not interfere with the shape of the Fock state distribution. This distinction is particularly important for F_{CP} as the photon statistics that it is linked to in the main text are ultimately a measure of the photon state distribution shape. This is also closely linked to the photon number expectation value, for the very low drives that we are interested in when studying the cross-over from incoherent to coherent tunnelling, we know that $\langle n \rangle$ should be low ($\langle n \rangle < 1$) so we can afford to use very truncated state spaces. We know from knowledge of $\langle n \rangle$ that as E_J increases we will inherently need more states, and it is because of this that we chose to study two different E_J's, each extremity of the used N. These are $E_J \Delta^2 Q = 3$ and $E_J \Delta^2 Q = 10$.

To assess the impact that these physical quantities have on our calculations when there are no analytical expressions for the true values is quite challenging. Since we have no ground truth, we instead have to look for self-consistency in numerical calculations. The rationale behind this is fairly simple, with both of these quantities we wish to emulate what a F_{CP} value would be for a given $E_J \Delta^2 Q$ value would be like with $\tau = \infty$ and $N = \infty$. To assess this, we choose a starting τ

or N and begin performing simulations and calculating the F_{CP} values with incremental increases to τ or N. If the τ or N is too small, and thus either interfering with the F_{CP} calculation as described above, then the F_{CP} value will be inconsistent with previous simulations. Once we have reached τ or N values that are self-consistent, i.e. the case when increasing τ or N any more give no or little change to F_{CP}, we can then conclude that these quantities are no longer a limitation on the accuracy of the calculation.

Firstly, we consider integration length. We choose to study this as a multiplier of the original integration length, staring at half of it and going all the way up to 4 times the length. We can see from Figure B.3 and Figure B.4 that we are on the crux of what can be considered accurate, particularly with the higher drive. With the smaller drive, we could be considered within the accurate regime however as very little variation happens after a single integration length, this is not true for the higher drive, however for the sake of these notes variation over 1/200th of a percent of our total ratio can be considered negligible.

Next we consider the matter of systems size, which is shown in Figure B.5 and Figure B.6. In the case of higher drive it is clear that we have actually overestimated the number of states required, which is consistent with our knowledge of $\langle n \rangle$ as it is still sub 1 at this point. However, at the lower E_J we see inconsistencies up to 5 states, which seems strange as $\langle n \rangle$ is very small at this point. That is not to say we don't have any intuition about this, we know from calculations at high Δ that even at small $\langle n \rangle$ the $N = 4$ can distort the wave function to the point where sensitive quantities such as F_{CP} and $g^{(2)}(0)$ can be affected. Because of this, even for small calculations where we would expect $\langle n \rangle$ to be small, for sensitive quantities such as F_{CP} and $g^{(2)}(0)$ it is required that we use larger then expected N, such as $N >= 5$, as shown in Figure B.5.

From our studies of F_{CP}, it is clear that simulations with the values τ and N for the given $E_J\Delta^2 Q$ used in the main text do lead to results that are consistent with simulations done with larger τ and N values, implying that they are very close to the true values of F_{CP}, probably showing a less than 0.1% deviation from the correct value for the considered range of $E_J\Delta^2 Q$. It is clear that larger values of τ and N can improve the accuracy of the simulations slightly, however there is always a trade-off between increasing these parameters in a calculation and the time, computing power, and memory used in the process. In future work, use of a High Performance Computing cluster (HPC), use of a more time and memory efficient computation language such as Julia or C++,
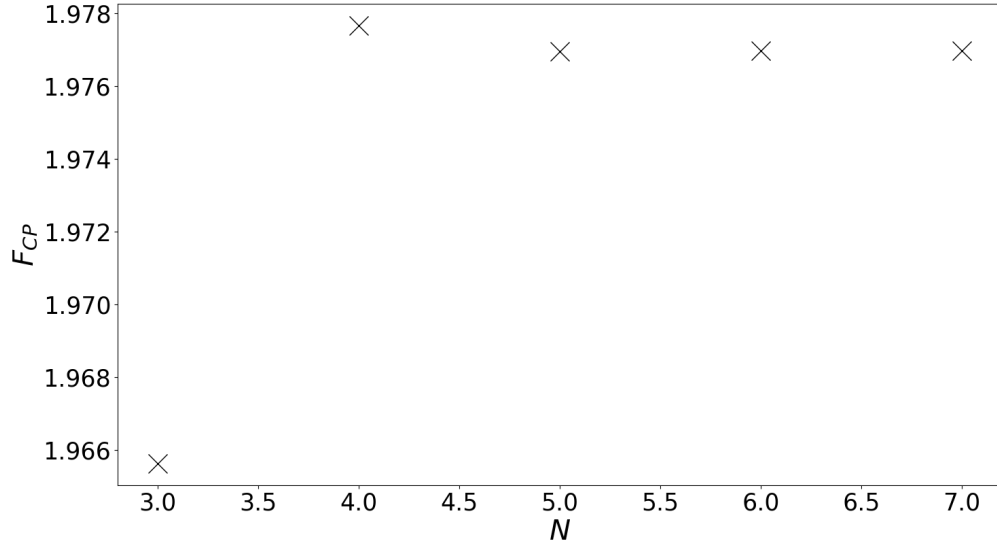
Figure B.5: F_{CP} for $E_J\Delta^2 Q/\hbar\omega_0 = 3$ showing convergence on a value as the number of states is increased in the $\tau = 24000$ integration length.
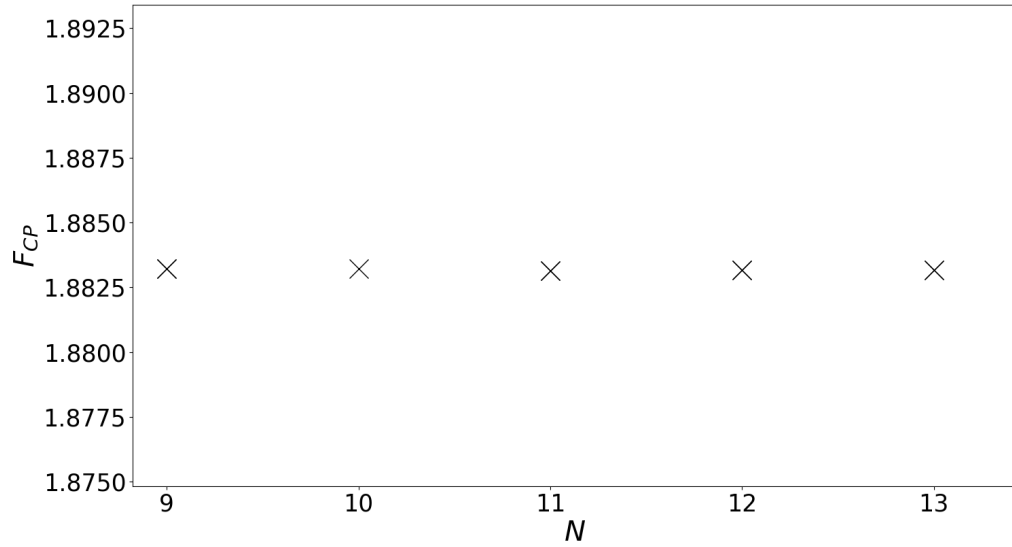
Figure B.6: F_{CP} for $E_J\Delta^2 Q/\hbar\omega_0 = 10$ showing convergence on a value as the number of states is increased in the $\tau = 24000$ integration length.

and/or a change of numerical method could be used to make these calculations more efficient.

B.4   Example python code

In the previous sections we have discussed in detail how to calculate F_{CP}. However, it may be useful to examine how these methods are actually implemented in code. In this section we present the code used for the calculations both in Chapter 3 and in this appendix. The code has been annotated to Python PEP 8 standards in an attempt to aid readability.

```python
# Import all relevant modules
import numpy as np
from qutip import *


"""
Set the generic system parameters that affect the accuracy of the integration
"""
N = 10  # Set the fock system size
options = Options(atol=1e-9, rtol=1e-7)  # Set tolerances for the solver


"""
Set the quantum operators to be used by qutip
"""
a = destroy(N)  # Define the annihilation operator
a_dag = a.dag()
n = num(N)  # Define the size number operator
g2 = a_dag * a_dag * a * a
H0 = n  # The time independent Hamiltonian
# The times for which the equation should be solved(scaled by 2pi to make
# peak selection easier later in the program)


number_of_iterations = 1  # The number of integrations to be performed in a row for
```

```python
# a single perimeter set. Implemented to allow for integrations to be
# continued after the fact


t = np.linspace(0, 1000, 250001) * 2 * np.pi  # The times over which the integration
# will be performed


Drive = np.linspace(0, 50 * 0.2, 51)  # The drive values over which the


Q = 1
o = 0.5



def H1_coeff(t, args):
    """
    Returns the matrix coefficient for the second component of the split
    Hamiltonian.

    Parameters
    ----------
    t : float
        The time of value to be returned.
    args : dict
        The constant values to be used in the function.

    Returns
    -------
    float
        The value of the coefficient for the second component of the split
    Hamiltonian.
    """
```

```python
    omega = args[0]   # Set the first time dependent coefficient
    # for the Hamiltonian
    return np.cos(t * omega)



def H2_coeff(t, args):
    """
    Returns the matrix coefficient for the third component of the split
    Hamiltonian.

    Parameters
    ----------
    t : float
        The time of value to be returned.
    args : dict
        The constant values to be used in the function.

    Returns
    -------
    float
        The value of the coefficient for the second component of the split
    Hamiltonian.
    """
    omega = args[0]   # Set the second time dependent coefficient
    # for the Hamiltonian
    return np.sin(t * omega)



def den_matrix_solver(L, N=5, delta=0.15, omega0=1, omegad=0.5, q=1500):
    """
```

A wrapper function for calculating a master equation solution for a given

parameter set.

Parameters

L : float

> *The drive value*

N : int, optional

> *The number of states available to the system. The default is 5.*

delta : float, optional

> *The strenth of the zero point quantum fluctuation. The default is 0.15.*

omega0 : float, optional

> *The natural frequency of the quantum harmonic oscillator.*

> *The default is 1.*

omegad : float, optional

> *The Josephson frequency. The default is 0.5.*

q : float, optional

> *The Q factor of the cavity. The default is 1500.*

Returns

----

qutip.Qobjt

> *The qutip results object for this integration.*


```
"""
const = {omegad}  # A redundant dictionary as mesolve requires an args
# input but can but can input but can be used to insert the frequencies into
# H1_coeff &  H2_coeff if we're interested in different ratios than 1/2
H1 = -(delta * (a.dag() + a)).cosm()  # The time independent part of H1
```

```python
    H2 = (delta * (a.dag() + a)).sinm()  # The time independent part of H2


    # The Full Hamiltonian where assembled in a nested list form where each
    # sublist contains both the time independent part of the term and the time
    # dependent function
    H = [H0, [(L / delta) * H1, H1_coeff], [(L / delta) * H2, H2_coeff]]


    # The list of collapse operators for use in the Lindbald master equation
    # stated in form sqrt(gamma)*L
    c_ops = [np.sqrt(1 / q) * a]


    s_op = [n, n ** 2]  # The List of operators that mesolve will find the
    # expectation values for at each time step and be stored in the Results
    # object


    # The solver for the density matrix using the options defined and with a
    # text progress bar to be printed to the console
    result = mesolve(H, rho0, t, c_ops, s_op, args=const,
                     progress_bar=True, options=options)
    return result  # return the results object


if __name__ == '__main__':
    """
    The main loop that loops over each value of the drive to calculate the
    solution in this parameter range, can be altered to loop over other
    perimeters
    """
    for L in Drive:
        rho0 = fock_dm(N, 0)  # Define the initial condition of the integration
```

```python
"""
loop over the number of iterations
"""

for i in range(number_of_iterations):
    ev_den_mat = den_matrix_solver(L, N, delta=0.2, omegad=o, q=Q)   # Solve
    # the problem using our custom function
    qsave(ev_den_mat, 'p=1_n_expect_and_n_sqr_L' + str(L))   # Save the
    # density matrix values from this integration
    rho0 = ev_den_mat.states[-1]   # take the last state from this
    # integration to act as the new initial conditions
    del ev_den_mat   # Delete the old solution so it is not held in
    # memory, this is nessecery to not crash the program for larger
    # integration with longer t or larger N
    print(i)


    # This commented out code is to load and plot the data however it
    # could be altered to do any type of possessing required
    """
    data=qload('p=1_n_expect_and_n_sqr_L'+str(L))
    plt.plot(L,np.mean(data.expect[0][-10000:]),'x')
    """
```

Appendix C

Numerically Solving Volterra Equations

C.1 Introduction

As we have stated in the main text there are three passable ways of formulating of the JJ laser model. These are referred to as the 'Brute Force' method which involves an integration of all coupled equations of motion for the modes, the 'Volterra Method', and the 'Truncated Volterrra Method', each each of which involves a reformulation in terms if integral equations. All of these equations originate in the paper by S. Simon's original paper[32]. This appendix explains each of these methods in detail and the specific algorithms used to solve them to a high level of accuracy.

C.2 The Brute Force Method

C.2.1 Method

This is the non-collective formulation where each oscillator is treated as an individual dynamical system with a collective non-linear drive term. The nth oscillator has an equation of motion for its phase ψ_n of form,

$$\ddot{\psi}_n = -\omega_n^2 \psi_n - 2\gamma \dot{\psi}_n + \alpha_n \lambda \sin(Vt + \sum_n \alpha_n \psi_n), \tag{C.1}$$

where γ is the rate of leakage from the cavity to a nearby transmission line, V is the voltage across the junction, λ is the interaction strength between the junction and the mode, and α_n is a parameter who's value can change depending on the positioning of the junction embedding in the cavity [1]. Thus, the behaviour of a many mode system can be described by solving the system of resulting n second order differential equations. The collective dynamics are determined by summing the solutions to give $\Psi = \sum_n \alpha_n \psi_n$. This formulation was first proposed in the supplemental material of [31].

The differential equations are formulated as a set of $2n$ first order differential equations. This gives,

$$\dot{\psi_n} = \nu_n \tag{C.2}$$

$$\dot{\nu_n} = -\omega_n^2 \psi_n - 2\gamma\nu_n + \alpha_n \lambda \sin(Vt + \sum_n \alpha_n \psi_n). \tag{C.3}$$

These can be solved using a Runge-Kutta algorithm with equal weighting on all terms[70]. This was done with standard preset algorithms from the Scipy toolbox[84] with the Runge-Kutta method of order 8(5,3) algorithm being the one used due to our familiarity with the method and the need for equal step size in analysis.

C.2.2 Results and Checks

If we wish to evaluate accuracy and viability of a method then we must first examine the possible parameter combinations and the difficulties that arise from them our in chosen system. We must also consider what we can do to increase the accuracy in the calculation and how this evolves with the various other parameters.

Let's begin by considering what dials we have to control accuracy. Because of the way we have chosen to solve the system of first order equations we have two possible ways of altering the accuracy, the separation of the points in the integration, h, which is measured by the point density per period, n_p, and the numerical integration methods set absolute and relative tolerances. For the most part the absolute and relative tolerances of the integrator were set to 10^{-12} and 10^{-14} as the highest possible values without seriously impacting the systems CPU time. The greater the value

---

[1]Varying α can change how strongly each mode effects the drive, and while how this effects the laser is a interesting question we simply take $\alpha = 1$ in all of the following calculations for simplicity
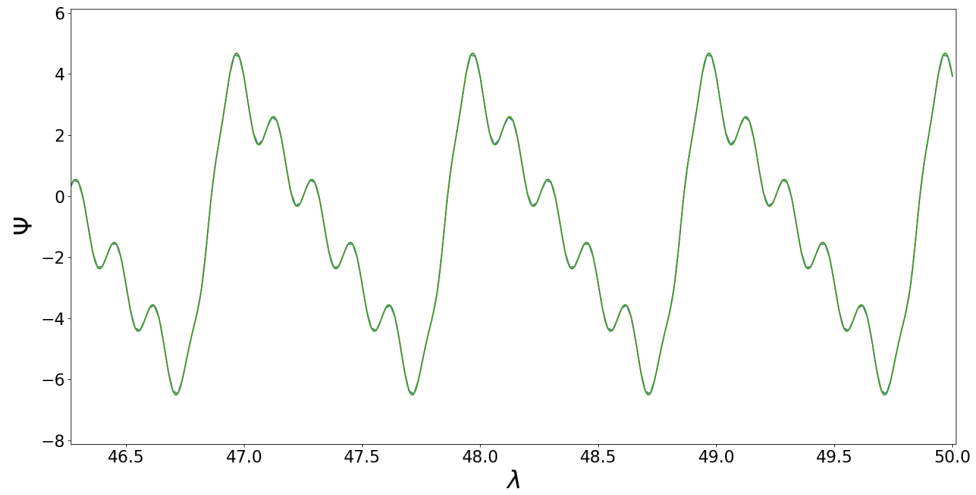
Figure C.1: :Ψ calculated with the brute force method for $n_p = 50-500$ showing uniform consistency at $\lambda = 5$ for $N = 5$
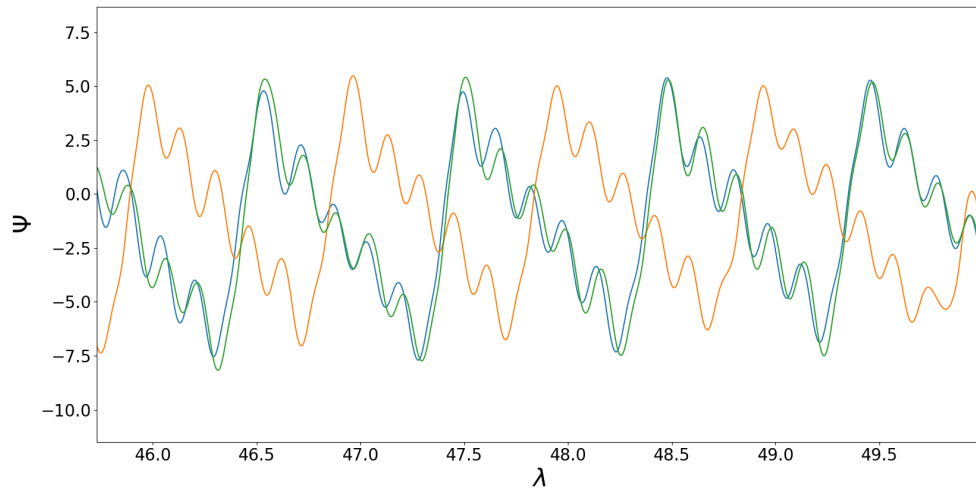

Figure C.2: Ψ calculated with the brute force method for $\lambda = 6$ with $N = 5$ and $n_p = 1000 - 10000$ showing no consistency.
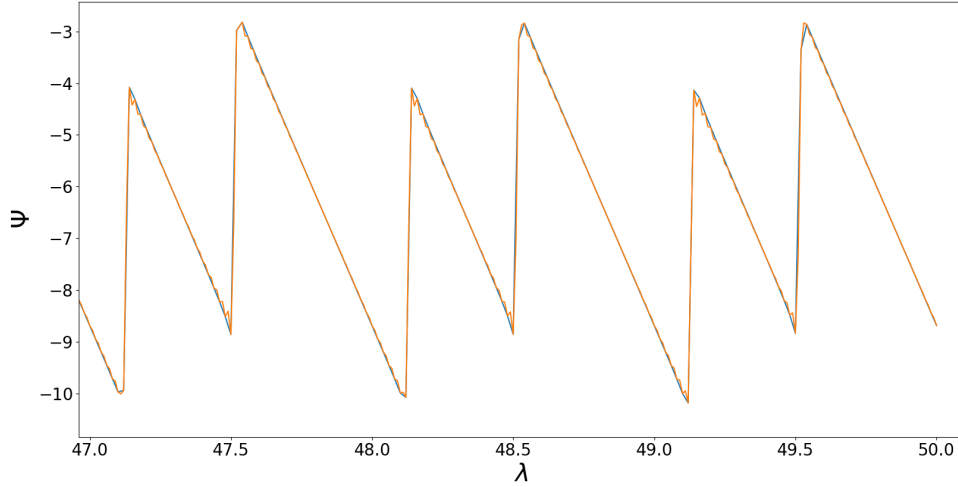
Figure C.3: A comparison of Ψ calculations by the brute force method for $n_p = 50 - 500$ showing uniform consistency with $\lambda = 6$ and $N = 50$

of n_p the less error is intruded per time step taken but the greater the CPU time and memory needed to perform the calculation for a given endpoint, t.

Firstly, consider the coupling constant between the junction and the oscillators, λ. λ represents how strongly the junction influences the oscillators and can be considered the strength of the drive, i.e. the larger λ is the more energy we are inputting into the modes. This quantity is very impotent to accuracy as it can determine how stable the oscillations are. For example, for a given λ if we only had one oscillator of a given frequency it could be in a relatively stable regime with only one periodic solution, a regime with many stable solutions depending on initial conditions, or a chaotic regime. As such, the λ of the given calculation will have a large influence on the required accuracy, with higher λ requiring a greater accuracy. This change can be very dramatic. This is illustrated by Figure C.1. which is calculated at $\lambda = 5$ and shows convergence for as little as $n_p = 50$. In contrast Figure C.2. which is calculated at $\lambda = 6$ and fails to show a convergence even for $n_p = 10000$.

Secondly, consider the number of oscillators, N. It isn't immediately clear how N should effect the stability of the system, however we found that as we increase N less accuracy is needed. Figure C.3 shows $N = 50$ for $\lambda = 6$ which shows good convergence for as $n_p = 50$ in strong contrast to the $N = 5$ case shown in Figure C.2. This is in line with our understanding of how the system's dynamics evolves with N. As N is increase the value of λ needed to move the system from the

drive frequency to the natural frequency of the system increases implying that these effects are somewhat linked.

Given the issues that the system appears to have with consistency, particularly when it comes to the use of point density, n_p, it is reasonable to ask if the equations being studied here are stiff. The honest answer is that it is not clear from the analysis done here, but it does appear to show some of the hallmarks of stiffness in some regimes, such as the high dependency on the n_p value. However, without a much more detailed study of $\dot{\psi}_n$ it is not really possible to conclude one way or the other.

C.3 The Volterra Method

C.3.1 Method

The key innovation of Simon and Cooper's work[32] is their reformulation of equation (C.1) so that, instead of a potentially infinite number of simultaneous differential equations, we can deal with any number of modes in a single equation. This method has clear computational advantages: it can scale with N without increasing any CPU time as N is only used to define the Green's function which can be calculated independently and in an expedient manner. Thus the only CPU time scaling comes from the choice of the number of points used in the integration.

This method comes from considering the collected phase, $\Psi = \sum_n \alpha_n \psi_n$, and then, using the greens function for equation (C.1), the solution for Ψ becomes,

$$\Psi(t) = \lambda \int_{-\infty}^{t} dt' \sum_n \alpha_n^2 G(t-t') \sin\left(Vt' + \Psi(t')\right), \tag{C.4}$$

where $G(t-t') = \frac{\sin(\tilde{\omega}_n t)}{\tilde{\omega}_n} e^{-\gamma t} \Theta(t)$, with $\Theta(t)$ is a step function and $\tilde{\omega}_n = \sqrt{\omega_n^2 - \gamma^2}$ is the standard green's function for a damped driven harmonic oscillator. Equation (C.4) is a Volterra equation and can be solved using a marching method where each time step is solved using a sum of all previous time steps. There are several way of formulating this method however the me most useful was found in the book by W. H. Press et. al.[85]. Using their approach we can show that the ith

time step of the integration of Ψ is given by,

$$\Psi_i - \lambda \frac{1}{2} h K_{ii} \sin\left(Vt_i + \Psi_i\right) = h\lambda \left(\frac{1}{2} K_{i0} \sin\left(Vt_0 + \Psi_0\right) + \sum_{j=1}^{i-1} K_{ij} \sin\left(Vt_j + \Psi_j\right) \right), \qquad \text{(C.5)}$$

where $K_{ij} = \sum_n \alpha_n^2 G(t_i - t_j)$, and h is the separation of each time step.

This method is still reliant on knowing Ψ_i, the term we wish to calculate, which is not known. This method also requires us to know the initial value of psi, ψ_0, at t_0. For the first issue we find that K_{ii} is zero as $\sin\left(0\right) = 0$ thus this term can be disregarded and we don't need to know the final value of the integration. The first value of the integration can also be disregarded as $\Phi_0 = 0$, as per our initial conditions, and $\sin(t_0) = \sin(0) = 0$ thus the term outside of the sum can also be disregarded. Because $\Phi_0 = 0$ we can quickly get our first point, Φ_1 by applying the equation C.5. The sum will disappear as it has nothing to sum over and the first term evaluate to zero hence we can always conclude that $\Phi_1 = 0$ in all cases. This leaves

$$\Psi_i = h\lambda \left(\sum_{j=1}^{i-1} K_{ij} \sin\left(Vt_j + \Psi_j\right) \right), \qquad \text{(C.6)}$$

which using $\Phi_1 = 0$ can be used t_0 calculate all other points in the series. This approach so far has in fact been the lowest order variation of the marching method, and although it is appropriate for much of the parameter space, in regimes where a high accuracy becomes necessary we must use a more sophisticated approach. For this we turn to a Newton-Cotes formulation of this problem. The Newton-Cotes method suggests instead of considering the integration to have equal weighting on every time step we instead must consider,

$$\int_0^{nh} \Psi(t)dt = h \sum_{i=0}^{n} w_{in} \Psi(t_i) \qquad \text{(C.7)}$$

where w_{in} is the given weighting that particular n and i. This simple alteration leads to two complications: Normal Newton-Cotes methods such as Simpson's rule requires an even finishing total number of integrating points and the method requires the first 2 points, Ψ_0 and Ψ_1, to be known to give non-zero values.

This is problematic for two reasons. Firstly, is not possible for a marching method to only have an even number of integration points, we must alternate between an even and odd number, so some

alteration is necessary. The alteration we chose to use is known as the Upper end three-eighths rule and is detailed along with the actual weights used in the book by P. Linz[86]. This method alters the weights of the last 3 points in the integration with an odd number of points in an attempt to smear out the error that would be introduced.

Secondly, it is impossible to apply this method without requiring at least two points, Ψ_0 and Ψ_1, which we call the seed signal. These two points are mandatory and must be calculated using a different method as the weighting brakes down if we try and calculate Ψ_1. This problem is solved by a compromise: We calculate the first few points with an alternate method, normally the brute force Method, and then use this as a seed signal for the Newton-Cotes method. While we only need to calculate the first 2 points of the integration we found that the method tended to work better, with more accurate results, when we calculated more, i.e. we tended to seed using the first 100 points.

C.3.2 Results and Checks

For the Volterra method we still have the same issues to contend with, i.e. accuracy issues that arise from increasing λ and from decreasing N. However, we only have one parameter that we can adjust to determine a accuracy, h or equivalently n_p.
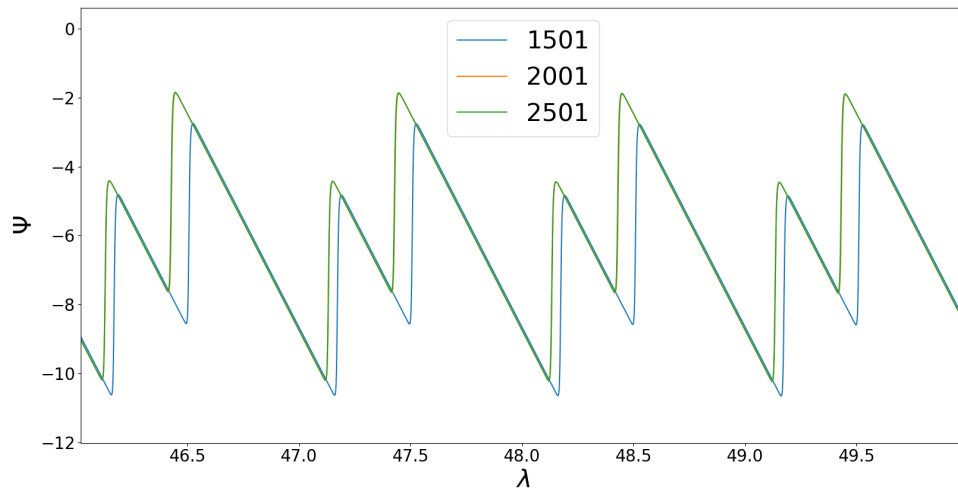

Figure C.4: A calculation of Ψ using the lowest order Volterra method in a regime where the brute force method can be applied, $\lambda = 7.1$ and $N = 300$, showing convergence.
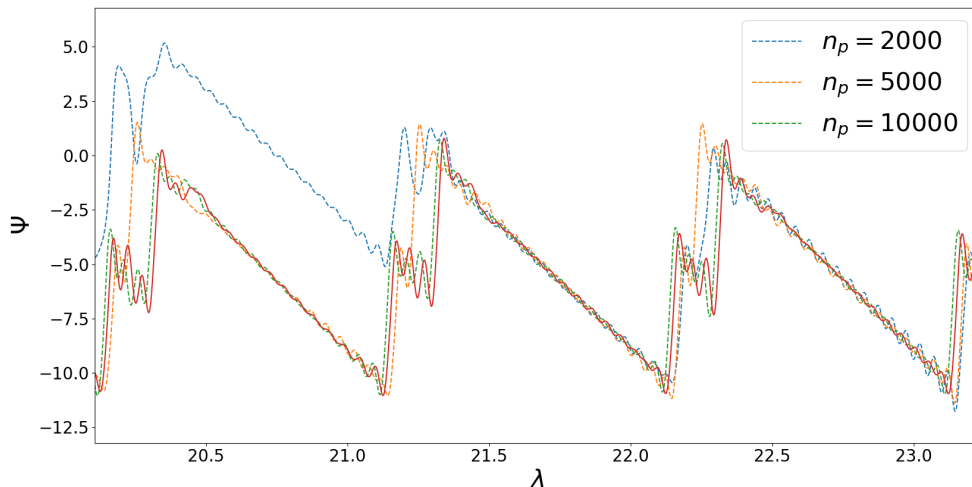
Figure C.5: A calculation of Ψ using the Volterra Newton-Cotes method, dotted, in a regime which is harder to simulate with the brute force method, $\lambda = 7.1$ and $N = 20$, showing convergence to the brute force method, red solid.

In the above section we presented two methods, a lowest order Volterra method and a higher order Newton-Cotes method similar to Simpson's rule. The reason for this is because they have fundamentally different functions despite using the same underlying method, the lowest order method being much faster as weighting calculations do not need to be implemented, but the higher order method has a higher limit of accuracy. However each of these methods still requires a larger number of points per period than the Equation one method, needing around $n_p = 2500$ to get a self consistent answer in the same region of parameter space where the brute force method only requires $n_p = 100$, see Figure C.4. In regimes where the brute force method requires a high accuracy, a Newton-Cotes method with a very large number of points will also show similar results, see Figure C.5.

While the matching method is the simplest possible method for solving Volterra equations it is by no means the only one. A more complex method known as the Block by block method[70, 86, 87] solves them by splitting the solution into blocks of N simultaneous equations based on the Newton-Cotes sums. This is a much more efficient, however, it harbours the unfortunate quirk of requiring kernel to be well defined for $t' < t$. Even more sophisticated methods such as the convolutional Runge-Kutta method[88] exist.

C.4 The Truncated Volterra Method

C.4.1 Method

A serious issue with the Volterra method is its scaling with integration length. To add an additional point to the end of the integration we must sum over all other points that have been previously calculated! When this reaches the tens or hundreds of millions of points this can have a serious increase in required CPU time even with efficient programming in an uncompiled language such as python. As such we turn to the final method proposed in Simon and Cooper's paper[32] which we call the Shortened Volterra method.

The shortened method relies on the fact that the the integral from $t = 0$ to $t = t - T$ is simply the same as $\Psi(t - T)e^{-\gamma T}$ in the weak damping limit where $\tilde{\omega}_n \simeq \omega_n$. Thus we can shorten the summation to over the last period of points and use it as a correction to the previous value a period ago. Using this formulation we find that,

$$\Psi(t) = \Psi(t - T)e^{-\gamma T} + \int_{t-T}^{t} K_{t-t'} \sin\left(Vt' + \Psi(t')\right)dt' \tag{C.8}$$

becomes a valid approximation to the volterra method. Notably the integration is significantly shorter, taking place simply over the previous period of dynamics rather then the entire memory of the system, thus we call this the shortened volterra method.

As before, to computationally solve this equation we must turn again to again to a marching method however this time the marching method moves forward with each time step with a sum of fixed length with the form,

$$\Psi_i = \Psi(t_i - T)e^{-\gamma T} + h \sum_{j=i-n_p+1}^{i-1} K_{ij} \sin\left(Vt_j + \Psi_j\right), \tag{C.9}$$

Where n_p is the number of points in a period, and h is again the separation of the time steps in the integration. As before we have used the fact that $K_{ii} = 0$ to remove the dependency ion the last point and the first point of the sum is encapsulated in the $\Psi(t_i - T)e^{-\gamma T}$ terms and is thus not included in the sum[2].

---

[2]This may appear to be a slightly pedantic point to bring up but the accidental double counting of this first point can lead to huge numerical errors in the strongly nonlinear regime

The shortened Volterra method is substantially quicker then the original method as the code no longer has to access potently millions of entries in an array but only one now. However a new issue arises, the method now requires a of a full period of n_p points before we can begin calculating the solution. This is known as the seed signal or seed period and is calculated using other methods, normally the brute force method, which can cause issues if the sums are not programmed carefully.

C.4.2 Results and Checks

Since the shortened Volterra method is simply the normal Volterra method with a useful mathematical shortcut applied to it we can easily conclude that the method will behave the same with in the same regions. The difference comes in CPU time used for these calculations, the shortened method dose not need to slice and access all elements huge arrays, often in the millions of points, it only needs to access one set of n_p entries the calculation time is much shorter then both previous methods

However, there is a trade off. Firstly, it is an approximation that we would expect to only work in the weak damping limit where $\tilde{\omega}_n \simeq \omega_n$. And secondly, it is unclear how we would begin to alter it such that a Newton-Cotes style method would be applicable and as such caution must be applied in regimes where the system my be sensitive to accuracy problems.

C.5 Example python code

In the previous sections we have discussed in detail how to calculate Ψ using various different methods. However, it may be useful to examine how these methods are actually implemented in, specifically the truncated Volterra method . In this section we present the code used for the calculations both in Chapter 4 and in this appendix. The code has been annotated to Python PEP 8 standards in an attempt to aid readability.

```python
import numpy as np
from matplotlib import pyplot as plt


class volterra_solver:
    """
```

```python
A class to control the marching method for calculating the solution of
Volterra equation.
"""


def __init__(self, t_vec, N, Q, lamda, V, alpha=[], omega_0=[], Inital=0):
    """

    Parameters
    ----------
    t_vec : np.array
        The times over which the integration will be performed.
    N : int
        The number of modes that are being driven in the system.
    Q : float
        The quality factor the cavity.
    lamda : float
        The drive strength the system.
    V : float
        The voltage across the junction.
    alpha : np.array, optional
        The alpha values for the system, if default all set to one.
        The default is list([]).
    omega_0 : np.array, optional
        The natural frequencies of the modes in the cavity, if default they
        will be set to one. The default is list([]).
    Inital : float, optional
        The total initial value of the oscillators. The default is 0.

    Raises
    ------
```

```python
Exception

    EXCEPTIONS are raised if arrays are provided for alpha or omega_0

    who's length doesn't match the number of oscillators N.


Returns

-------

None.


"""


self.time = t_vec * (2 * np.pi)

self.dt = (self.time[1] - self.time[0])

self.mode_number = N

self.mode_mutiplier = np.linspace(1, N, N)

self.gamma = 1 / Q

self.lamda = lamda

self.voltage = V

self.Inital_condition = Inital


# Check if the alpha array needs to be set to the default

if len(alpha) == 0:


    self.alpha = np.ones(int(N))


elif len(alpha) == N:


    self.alpha = alpha


else:
```

```python
        raise Exception('Alpha must be the same length as specified N')


    # Check if the omega array needs to be set to the default
    if len(omega_0) == 0:


        self.omega_0 = self.mode_mutiplier


    elif len(omega_0) == N:


        self.omega_0 = omega_0


    else:


        raise Exception('Frequencies must be the same length as specified N')


def kernal_Value(self, t):
    """
    Calculate the value of the kernel at a given time


    Parameters
    ----------
    t : float
        The time used to calculate the kernel value.


    Returns
    -------
    K : float
        The kernel value at time t.


    Notes
```

```python
        -----

        This is a internal method and not intended to be used by the end user
        """


        K = np.zeros(len(t))


        for n in range(self.mode_number):
            K += self.alpha[n] ** 2 * np.exp(-self.gamma * t) * np.sin(
                self.omega_0[n] * (t)) / (self.omega_0[n])


        return K


    def progress_bar_func(self, t):
        """
        Check and print a progress update depending on how much of the
        intergration is left to be done.


        Parameters
        ----------
        t : flaot
            The time of the current integration point.


        Returns
        -------
        None.


        Notes
        -----
        This is a internal method and not intended to be used by the end user
```

```python
        """

        progress_persentage = t / np.max(self.time) * 100


        if progress_persentage > self.progress_mile_stone:
            print('Integration ' + str(self.progress_mile_stone)
                    + '% complete')
            self.progress_mile_stone += 10


    def solve_equation(self, progress_bar=False):
        """
        Solves the Volterra equation using the marching method.


        Parameters
        ----------
        progress_bar : bool, optional
            Toggle the progress bar on or off. The default is False.


        Returns
        -------
        None.


        """


        if progress_bar:
            self.progress_mile_stone = 0


        self.psi = np.zeros(len(self.time))
        self.psi[0] = self.Inital_condition


        self.kernal = self.kernal_Value(self.time)
```

```python
        for i in range(1, len(self.time)):
            self.psi[i] += sum(self.kernal[(i - 1):1:-1] * np.sin(
                self.voltage * self.time[1:(i - 1)] + self.psi[1:(i - 1)])
                            * self.dt * self.lamda)
            self.psi[i] += 0.5 * self.dt * self.lamda * self.kernal[i] * self.psi[0]


            if progress_bar:
                self.progress_bar_func(self.time[i])


    def plot(self):
        """
        Plot the result of the solve_equation method.


        Returns

        -------

        None.


        """


        plt.plot(self.time / (2 * np.pi), self.psi)


        plt.xlabel('$t/T$')


        plt.ylabel('$\Psi$')
```

Appendix D

First and Second order Approximations to Many Mode Truncated Volterra Equations

D.1 The Dynamics Under Weak Drive

In Chapter 4 we talk about using a perturbative approximation to the many mode JJ laser system to try to obtain analytic solutions in the low energy limit. This method is actually mentioned but not presented by Simon and Cooper[32] as they considered the method trivial. However, when attempting to reproduce their method we found it to be fairly long and involved, with several non trivial steps. As such we though it best to reproduce the method in this appendix as it is too long for the main text.

D.1.1 Full First order perturbation theory

The lowest order approximation to $\Psi(t)$ is first order in λ. In this case we can drop the non-linear element in the right hand side of equation (2.16) and find,

$$\Psi(t) = \lambda \int_{-\infty}^{t} dt' K(t - t') \sin(Vt').$$ (D.1)

This equation is exactly solvable. The process is simplified by performing a change of variables. Defining, $\tau = t - t'$ we find

$$\psi(t) = \lambda \int_0^\infty d\tau K(\tau) \sin(V(t-\tau)). \tag{D.2}$$

This is most easily solved using integration by parts. Defining our two functions we state that,

$$\Psi(t) = \lambda/2 \int_0^\infty d\tau f'(\tau)g(\tau) = \lambda/2[f(\tau)g(\tau)] - \lambda/2 \int_0^\infty d\tau f(\tau)g'(\tau), \tag{D.3}$$

$$g(\tau) = [T/2 - \tau \ (\text{mod } T)], \tag{D.4}$$

$$f'(\tau) = e^{-\gamma\tau} \sin(V(t-\tau)). \tag{D.5}$$

Integrating $f'(\tau)$ and differentiating $g(\tau)$ gives,

$$g'(\tau) = [1 - T\sum_{n=1}^\infty \delta(\tau - nT)], \tag{D.6}$$

$$f(\tau) = -\frac{1}{2i}\left[\frac{e^{iV(t-\tau)}}{(\gamma + iV)} - \frac{e^{-iV(t-\tau)}}{(\gamma - iV)}\right]e^{-\gamma\tau}, \tag{D.7}$$

which allows us to evaluate the integration by parts. The non-integral term becomes,

$$\lambda/2[f(\tau)g(\tau)] = \frac{\lambda T}{4(\gamma^2 + V^2)}(\gamma\sin(Vt) - V\cos(Vt)). \tag{D.8}$$

Evaluating the second term is a more involved process. Consider the integral,

$$-\lambda/2 \int_0^\infty d\tau f(\tau)g'(\tau) = \lambda/4i \int_0^\infty d\tau[1 - T\sum_{n=1}^\infty \delta(\tau - nT)]\left[\frac{e^{iV(t-\tau)}}{(\gamma + iV)} - \frac{e^{-iV(t-\tau)}}{(\gamma - iV)}\right]e^{-\gamma\tau}, \tag{D.9}$$

which can be split up into two different integrals, one with the constant term from $g'(\tau)$ and the other with the delta function from $g'(\tau)$. The first simply becomes the second integral of $f(\tau)$ and has the form,

$$\lambda/4i \int_0^\infty d\tau \left[\frac{e^{iV(t-\tau)}}{(\gamma + iV)} - \frac{e^{-iV(t-\tau)}}{(\gamma - iV)}\right]e^{-\gamma\tau}, = \frac{\lambda}{2(\gamma^2 + V^2)^2 + 8V^2\gamma^2}((\gamma^2+V^2)\sin(Vt)+2\gamma V\cos(Vt)),$$
$$\tag{D.10}$$

which notably has no dependency on the system's periodicity and in most cases can be neglected as being an order of magnitude smaller than all other terms. The second integral only has to be evaluated at integer values nT due to the Dirac delta functions and thus is simply of form,

$$= \frac{\lambda T}{2(\gamma^2 + V^2)}(\gamma \sin(Vt) - V \cos(Vt))\frac{e^{-\gamma T}}{1 - e^{-\gamma T}} \tag{D.11}$$

where we have used $\sum_{n=1}^{\infty} e^{-\gamma nT} = \frac{e^{-\gamma T}}{1-e^{-\gamma T}}$ to simplify the resulting infinite sum. This gives us a final expression for the lowest order approximation as,

$$\Psi(t) = \frac{\lambda T}{4(\gamma^2 + V^2)}(1 + 2\frac{e^{-\gamma T}}{1 - e^{-\gamma T}})(\gamma \sin(Vt) - V \cos(Vt))$$
$$+ \frac{\lambda}{2(\gamma^2 + V^2)^2 + 8V^2\gamma^2}((\gamma^2 + V^2)\sin(Vt) + 2\gamma V \cos(Vt),) \tag{D.12}$$

which has period $2\pi/V$. Not all the terms of this equation are of the same order, in fact some are much smaller than others, specifically to determine the order of each term we use the knowledge that $\gamma \ll V$. When this condition is imposed, we find that only the $-V \cos(Vt)$ term contributes significantly to the dynamics.

D.1.2 Full Second Order Perturbation Theory

To further show the pattern of frequencies that will go on to form a sawtooth like wave we must now calculate the second order approximation. Let us consider the first order solution solution to be the form of,

$$\Psi^{(0)}_{\gamma \ll 1}(t) = -A \cos(Vt) \tag{D.13}$$

where $A = \frac{\lambda T}{4V}(1 + 2\frac{e^{-\gamma T}}{1-e^{-\gamma T}})$ but is still small provided $\frac{\lambda}{\gamma V}$ is small enough. We have dropped the sine term from the original solution as it is more then a order of magnitude smaller then then other terms. We substitute this into (2.16) and find,

$$\Psi(t) = \lambda \int_{-\infty}^{t} dt' K(t - t') \sin(Vt' - A \cos(Vt')). \tag{D.14}$$

We the use the sine addition formulae to split the nonlinear term, and write the equation (D.14) as,

$$\Psi(t) = \lambda \int_{-\infty}^{t} dt' K(t - t') \left[\sin(Vt') \cos(A\cos(Vt')) - \cos(Vt') \sin(A\cos(Vt')) \right]. \qquad \text{(D.15)}$$

This still leaves us with a non-linearity in the integral, however, this can be simplified by using the Jacobi-Anger expansion. Using this we see,

$$\cos(A\cos(Vt')) = J_0(A) + 2 \sum_{n=1}^{\infty} (-1)^n J_{2n})A) \cos(2nVt'), \qquad \text{(D.16)}$$

$$\sin(A\cos(Vt')) = -2 \sum_{n=1}^{\infty} (-1)^n J_{2n-1}(A) \sin((2n-1)Vt'), \qquad \text{(D.17)}$$

and knowing that $A \propto \lambda$ we can use the following lowest order approximations,

$$J_0(A) = 1,$$

$$J_1(A) = A/2,$$

$$J_\kappa(A) = 0, \kappa \geq 2$$

in the case where A is small. We can use this approximation as we have already stated that is this a perturbative approach and any solution will be very small. This allows the integral to be simplified to,

$$\Psi(t) = \lambda \int_{-\infty}^{t} dt' K(t - t') \left[\sin(Vt') - A\cos^2(Vt') \right]. \qquad \text{(D.18)}$$

The first term of this is simply the first order approximation again and can be solved in the same way as before. The second term then becomes our second order approximation,

$$\Psi^{(2)}(t) = -\lambda A \int_{-\infty}^{t} dt' K(t - t') \cos^2(Vt'). \qquad \text{(D.19)}$$

To solve this we can again use the variable replacement of $\tau = t - t'$ to solve this integral. Using this we see,

$$\Psi^{(2)}(t) = \lambda A \int_{0}^{\infty} dt' K(\tau) \cos^2(V(t - \tau)). \qquad \text{(D.20)}$$

Then, using the cosine square formula, we write,

$$\Psi^{(2)}(t) = \lambda A/2 \int_0^\infty d\tau K(\tau)(1 + \cos(2V(t - \tau))). \tag{D.21}$$

To solve (D.21) we must split the integral into two sections: the integral of the decaying kernel and the integral of the oscillation and the decaying kernel. This is because we must treat the kernel differently if it is on its own to end up with physically sensible results. It is not clear why this is the case, and it is beyond the scope of this thesis to truly consider the mechanisms behind these integrations. Consider the integration of the decaying kernel,

$$I_1 = \frac{\lambda A}{2} \int_0^\infty d\tau K(\tau). \tag{D.22}$$

We solve this by using the first definition of the kernel where,

$$K(\tau) = \sum_{n=1}^\infty \frac{\sin(\omega_0 n \tau)}{\omega_0 n} e^{-\gamma \tau}. \tag{D.23}$$

Integrating this expression and applying the limits we find,

$$I_1 = \frac{\lambda A}{2} \sum_{n=1}^\infty \frac{1}{2i\omega_0 n} \left[\frac{1}{i\omega_0 n - \gamma} + \frac{1}{i\omega_0 n + \gamma} \right], \tag{D.24}$$

and in the limit of small γ we apply the approximation $i\omega_0 n \pm \gamma = i\omega_0 n$ which gives,

$$I_1 = \frac{-A\lambda}{2\omega_0^2} \sum_{n=1}^\infty \frac{1}{n^2}. \tag{D.25}$$

The sum of $1/n^2$ is known as the Basel problem and can be shown to be convergent to $\pi^2/6$ in the limit of infinite terms. This gives a final constant negative offset of,

$$I_1 = \frac{-A\lambda \pi^2}{12\omega_0^2} \tag{D.26}$$

which is of the correct order for the solution[32]. This leaves us with the expression,

$$\Psi^{(2)}(t) = -\frac{A\lambda \pi^2}{12\omega_0^2} + \frac{\lambda A}{2} \int_0^\infty d\tau K(\tau) \cos(2V(t - \tau)). \tag{D.27}$$

The second integral can be solved by using integration by parts. Defining our functions we find,

$$I_2 = \frac{\lambda A}{2} \int_0^\infty d\tau f'(\tau)g(\tau) = \frac{\lambda A}{2}[f(\tau)g(\tau)] - \frac{\lambda A}{2} \int_0^\infty d\tau f(\tau)g'(\tau), \tag{D.28}$$

$$g(\tau) = \frac{1}{2}[T/2 - \tau \ (\text{mod } T)], \tag{D.29}$$

$$f'(\tau) = e^{-\gamma\tau}\cos(2V(t-\tau)), \tag{D.30}$$

Integrating $f'(\tau)$ and differentiating $g(\tau)$ while applying the limit of small γ gives,

$$g'(\tau) = \frac{1}{2}[1 - T\sum_{n=1}^\infty \delta(\tau - nT)], \tag{D.31}$$

$$f(\tau) = \frac{-1}{2V}\sin(2V(t-\tau))e^{-\gamma\tau}, \tag{D.32}$$

which can easily be used to evaluate the non-integral terms of the integration by parts. Evaluating this we see our solution becomes,

$$\Psi^{(2)}(t) = -\frac{A\lambda\pi^2}{12\omega_0^2} + \frac{A\lambda T}{16V}\sin(2Vt) - \lambda A \int_0^\infty d\tau f(\tau)g'(\tau). \tag{D.33}$$

Lastly our final integral is split into two separate terms,

$$I_3 = \frac{\lambda A}{8V} \int_0^\infty d\tau \sin(2V(t-\tau))e^{-\gamma\tau}, \tag{D.34}$$

$$I_4 = \frac{\lambda A T}{8V} \sum_{n=1}^\infty \int_0^\infty d\tau \delta(\tau - nT)\sin(2V(t-\tau))e^{-\gamma\tau}, \tag{D.35}$$

of which I_3 is solved in a similar manner to $f(\tau)$. The integral in I_4 is trivially solved due to the Dirac delta function, simply meaning that we evaluate the integral as a sum of terms at $\tau = nT$. This gives,

$$I_4 = \frac{\lambda A T}{8V} \sum_{n=1}^\infty \sin(2V(t-nT))e^{-\gamma nT}, \tag{D.36}$$

which can be simplified by realising that $\sin(2V(t-nT)) = \sin(Vt)$ and again using the geometric series $\sum_{n=1}^\infty e^{-\gamma nT} = \frac{e^{-\gamma nT}}{1-e^{-\gamma nT}}$. This gives a final expression for the second order approximation as,

$$\Psi(t) = \Psi^{(1)}(t) - \frac{A\lambda\pi^2}{12\omega_0^2} + \frac{\lambda A T}{16V}\left(1 - 2\frac{e^{-\gamma nT}}{1 - e^{-\gamma nT}}\right)\sin(2Vt) - \frac{A\lambda}{16V}\cos(2Vt), \tag{D.37}$$

But again the cosine term can be ignored due to the fact that it is an order of magnitude smaller than all other relevant terms (again using the condition of $\gamma \ll V$).

Bibliography

[1] B. D. Josephson, "Possible new effects in superconductive tunnelling," *Physics Letters*, vol. 1, no. 7, pp. 251–253, 1962.

[2] ——, "Supercurrents through barriers," *Advances in Physics*, vol. 14, no. 56, pp. 419–451, 1965.

[3] ——, "The discovery of tunnelling supercurrents," *Reviews of Modern Physics*, vol. 46, no. 2, p. 251, 1974.

[4] A. M. Zagoskin, *Quantum engineering: theory and design of quantum coherent structures.* Cambridge University Press, 2011.

[5] J. You and F. Nori, "Atomic physics and quantum optics using superconducting circuits," *Nature*, vol. 474, no. 7353, pp. 589–597, 2011.

[6] R. Schoelkopf and S. Girvin, "Wiring up quantum systems," *Nature*, vol. 451, no. 7179, pp. 664–669, 2008.

[7] O. Astafiev, K. Inomata, A. Niskanen, T. Yamamoto, Y. A. Pashkin, Y. Nakamura, and J. Tsai, "Single artificial-atom lasing," *Nature*, vol. 449, no. 7162, pp. 588–590, 2007.

[8] J. E. Zimmerman and A. H. Silver, "Macroscopic quantum interference effects through superconducting point contacts," *Phys. Rev.*, vol. 141, pp. 367–375, 1 Jan. 1966. DOI: `10.1103/PhysRev.141.367`. [Online]. Available: `https://link.aps.org/doi/10.1103/PhysRev.141.367`.

[9] E. P. Day, "Detection of nmr using a josephson-junction magnetometer," *Phys. Rev. Lett.*, vol. 29, pp. 540–542, 9 Aug. 1972. DOI: `10.1103/PhysRevLett.29.540`. [Online]. Available: `https://link.aps.org/doi/10.1103/PhysRevLett.29.540`.

[10] J. Clarke and F. K. Wilhelm, "Superconducting quantum bits," *Nature*, vol. 453, no. 7198, pp. 1031–1042, 2008.

[11] H. T. Ng and F. Nori, "Quantum phase measurement and gauss sum factorization of large integers in a superconducting circuit," *Phys. Rev. A*, vol. 82, p. 042 317, 4 Oct. 2010. DOI: 10.1103/PhysRevA.82.042317. [Online]. Available: `https://link.aps.org/doi/10.1103/PhysRevA.82.042317`.

[12] E. Lucero, R. Barends, Y. Chen, J. Kelly, M. Mariantoni, A. Megrant, P. O'Malley, D. Sank, A. Vainsencher, J. Wenner, *et al.*, "Computing prime factors with a josephson phase qubit quantum processor," *Nature Physicfs*, vol. 8, no. 10, pp. 719–723, 2012.

[13] A. Gyenis, P. S. Mundada, A. Di Paolo, T. M. Hazard, X. You, D. I. Schuster, J. Koch, A. Blais, and A. A. Houck, "Experimental realization of a protected superconducting circuit derived from the 0–π qubit," *PRX Quantum*, vol. 2, p. 010 339, 1 Mar. 2021. DOI: 10.1103/PRXQuantum.2.010339. [Online]. Available: `https://link.aps.org/doi/10.1103/PRXQuantum.2.010339`.

[14] M. Hofheinz, F. Portier, Q. Baudouin, P. Joyez, D. Vion, P. Bertet, P. Roche, and D. Esteve, "Bright side of the coulomb blockade," *Physical Review Letters*, vol. 106, no. 21, p. 217 005, 2011.

[15] Y. A. Pashkin, H. Im, J. Leppäkangas, T. Li, O. Astafiev, A. Abdumalikov Jr, E. Thuneberg, and J. Tsai, "Charge transport through ultrasmall single and double josephson junctions coupled to resonant modes of the electromagnetic environment," *Physical Review B*, vol. 83, no. 2, p. 020 502, 2011.

[16] C. Padurariu, F. Hassler, and Y. V. Nazarov, "Statistics of radiation at josephson parametric resonance," *Phys. Rev. B*, vol. 86, p. 054 514, 5 Aug. 2012. DOI: 10.1103/PhysRevB.86.054514. [Online]. Available: `https://link.aps.org/doi/10.1103/PhysRevB.86.054514`.

[17] J. Leppäkangas, G. Johansson, M. Marthaler, and M. Fogelström, "Nonclassical photon pair production in a voltage-biased josephson junction," *Phys. Rev. Lett.*, vol. 110, p. 267 004, 26 Jun. 2013. DOI: 10.1103/PhysRevLett.110.267004. [Online]. Available: `https://link.aps.org/doi/10.1103/PhysRevLett.110.267004`.

[18] M. Marthaler, J. Leppäkangas, and J. H. Cole, "Lasing, trapping states, and multistability in a circuit quantum electrodynamical analog of a single-atom injection maser," *Phys. Rev. B*, vol. 83, p. 180 505, 18 May 2011. DOI: `10.1103/PhysRevB.83.180505`. [Online]. Available: `https://link.aps.org/doi/10.1103/PhysRevB.83.180505`.

[19] F. Chen, J. Li, A. Armour, E. Brahimi, J. Stettenheim, A. Sirois, R. Simmonds, M. Blencowe, and A. Rimberg, "Realization of a single-cooper-pair josephson laser," *Physical Review B*, vol. 90, no. 2, p. 020 506, 2014.

[20] M. Dykman, *Fluctuating nonlinear oscillators: from nanomechanics to quantum superconducting circuits*. Oxford University Press, 2012.

[21] A. Widom, "Quantum electrodynamic circuits at ultralow temperature," *Journal of Low Temperature Physics*, vol. 37, no. 3, pp. 449–460, 1979.

[22] J. You and F. Nori, "Atomic physics and quantum optics using superconducting circuits," *Nature*, vol. 474, no. 7353, pp. 589–597, 2011.

[23] T. Holst, D. Esteve, C. Urbina, and M. Devoret, "Effect of a transmission line resonator on a small capacitance tunnel junction," *Physical Review Letters*, vol. 73, no. 25, p. 3455, 1994.

[24] J. Basset, H. Bouchiat, and R. Deblock, "Emission and absorption quantum noise measurement with an on-chip resonant circuit," *Physical Review Letters*, vol. 105, no. 16, p. 166 801, 2010.

[25] D. Averin, Y. V. Nazarov, and A. Odintsov, "Incoherent tunneling of the cooper pairs and magnetic flux quanta in ultrasmall josephson junctions," *Physica B Condensed Matter*, vol. 165, pp. 945–946, 1990.

[26] G.-L. Ingold and Y. V. Nazarov, "Charge tunneling rates in ultrasmall junctions," in *Single charge tunneling*, Springer, 1992, pp. 21–107.

[27] A. Armour, M. Blencowe, E. Brahimi, and A. Rimberg, "Universal quantum fluctuations of a cavity mode driven by a josephson junction," *Physical Review Letters*, vol. 111, no. 24, p. 247 001, 2013.

[28] A. D. Armour, B. Kubala, and J. Ankerhold, "Noise switching at a dynamical critical point in a cavity-conductor hybrid," *Physical Review B*, vol. 96, no. 21, p. 214 509, 2017.

[29] V. Gramich, B. Kubala, S. Rohrer, and J. Ankerhold, "From coulomb-blockade to nonlinear quantum dynamics in a superconducting circuit with a resonator," *Physical Review Letters*, vol. 111, no. 24, p. 247 002, 2013.

[30] B. Lang and A. D. Armour, "Multi-photon resonances in josephson junction-cavity circuits," *New Journal of Physics*, vol. 23, no. 3, p. 033 021, 2021.

[31] M. Cassidy, A. Bruno, S. Rubbert, M. Irfan, J. Kammhuber, R. Schouten, A. Akhmerov, and L. Kouwenhoven, "Demonstration of an ac josephson junction laser," *Science*, vol. 355, no. 6328, pp. 939–942, 2017.

[32] S. H. Simon and N. R. Cooper, "Theory of the josephson junction laser," *Physical Review Letters*, vol. 121, no. 2, p. 027 004, 2018.

[33] G. F. Morley, A. Di Marco, M. Mantovani, P. Stadler, W. Belzig, G. Rastelli, and A. D. Armour, "Theory of double cooper-pair tunneling and light emission mediated by a resonator," *Physical Review B*, vol. 100, no. 5, p. 054 515, 2019.

[34] B. Lang, G. F. Morley, and A. D. Armour, "Discrete time translation symmetry breaking in a josephson junction laser," *Physical Review B*, vol. 107, no. 14, p. 144 509, 2023.

[35] G. Ménard, A. Peugeot, C. Padurariu, C. Rolland, B. Kubala, Y. Mukharsky, Z. Iftikhar, C. Altimiras, P. Roche, H. l. Sueur, *et al.*, "Emission of photon multiplets by a dc-biased superconducting circuit," *arXiv preprint arXiv:2111.09604*, 2021.

[36] C. Rolland, A. Peugeot, S. Dambach, M. Westig, B. Kubala, Y. Mukharsky, C. Altimiras, H. Le Sueur, P. Joyez, D. Vion, *et al.*, "Antibunched photons emitted by a dc-biased josephson junction," *Physical Review Letters*, vol. 122, no. 18, p. 186 804, 2019.

[37] R. D. Knight, *Physics for scientists and engineers*. Pearson Higher Ed., 2017.

[38] R. Feynman, R. Leighton, and M. Sands, *The Feynman lectures on physics, vol. 2*. Addison-Wesley Pub. Co, 1976.

[39] ——, *The Feynman lectures on physics, vol. 3*. Addison-Wesley Pub. Co, 1976.

[40] J. F. Annett *et al.*, *Superconductivity, superfluids and condensates*. Oxford University Press, 2004.

[41] B. Bransden and C. Joachain, *Quantum Mechanics*. Pearson, 2000.

[42]   K. Jacobs, *Quantum measurement theory and its applications*. Cambridge University Press, 2014.

[43]   A. J. Leggett, "Macroscopic quantum systems and the quantum theory of measurement," *Progress of Theoretical Physics Supplement*, vol. 69, pp. 80–100, 1980.

[44]   A. J. Leggett and A. Garg, "Quantum mechanics versus macroscopic realism: Is the flux there when nobody looks?" *Physical Review Letters*, vol. 54, no. 9, p. 857, 1985.

[45]   R. Prance, A. Long, T. Clark, A. Widom, J. Mutton, J. Sacco, M. Potts, G. Megaloudis, and F. Goodall, "Macroscopic quantum electrodynamic effects in a superconducting ring containing a josephson weak link," *Nature*, vol. 289, no. 5798, pp. 543–549, 1981.

[46]   S. Washburn, R. A. Webb, R. Voss, and S. Faris, "Effects of dissipation and temperature on macroscopic quantum tunneling," *Physical review letters*, vol. 54, no. 25, p. 2712, 1985.

[47]   M. H. Devoret, J. M. Martinis, and J. Clarke, "Measurements of macroscopic quantum tunneling out of the zero-voltage state of a current-biased josephson junction," *Physical review letters*, vol. 55, no. 18, p. 1908, 1985.

[48]   J. M. Martinis, M. H. Devoret, and J. Clarke, "Energy-level quantization in the zero-voltage state of a current-biased josephson junction," *Physical review letters*, vol. 55, no. 15, p. 1543, 1985.

[49]   Y. Nakamura, Y. A. Pashkin, and J. Tsai, "Coherent control of macroscopic quantum states in a single-cooper-pair box," *nature*, vol. 398, no. 6730, pp. 786–788, 1999.

[50]   M. H. Devoret *et al.*, "Quantum fluctuations in electrical circuits," *Les Houches, Session LXIII*, vol. 7, no. 8, pp. 133–135, 1995.

[51]   B. Yurke and J. S. Denker, "Quantum network theory," *Physical Review A*, vol. 29, no. 3, p. 1419, 1984.

[52]   J. M. Martinis, S. Nam, J. Aumentado, and C. Urbina, "Rabi oscillations in a large josephson-junction qubit," *Physical Review Letters*, vol. 89, no. 11, p. 117 901, 2002.

[53]   D. Averin, A. Korotkov, and K. Likharev, "Theory of single-electron charging of quantum wells and dots," *Physical Review B*, vol. 44, no. 12, p. 6199, 1991.

[54] R. Harris, A. Berkley, M. Johnson, P. Bunyk, S. Govorkov, M. Thom, S. Uchaikin, A. Wilson, J. Chung, E. Holtham, *et al.*, "Sign-and magnitude-tunable coupler for superconducting flux qubits," *Physical Review Letters*, vol. 98, no. 17, p. 177 001, 2007.

[55] F. Arute, K. Arya, R. Babbush, D. Bacon, J. C. Bardin, R. Barends, R. Biswas, S. Boixo, F. G. Brandao, D. A. Buell, *et al.*, "Quantum supremacy using a programmable superconducting processor," *Nature*, vol. 574, no. 7779, pp. 505–510, 2019.

[56] A. Wallraff, D. I. Schuster, A. Blais, L. Frunzio, R.-S. Huang, J. Majer, S. Kumar, S. M. Girvin, and R. J. Schoelkopf, "Strong coupling of a single photon to a superconducting qubit using circuit quantum electrodynamics," *Nature*, vol. 431, no. 7005, pp. 162–167, 2004.

[57] P. Forn-Díéaz, L. Lamata, E. Rico, J. Kono, and E. Solano, "Ultrastrong coupling regimes of light-matter interaction," *Reviews of Modern Physics*, vol. 91, no. 2, p. 025 005, 2019.

[58] F. Yoshihara, T. Fuse, S. Ashhab, K. Kakuyanagi, S. Saito, and K. Semba, "Superconducting qubit–oscillator circuit beyond the ultrastrong-coupling regime," *Nature Physics*, vol. 13, no. 1, pp. 44–47, 2017.

[59] A. Blais, R.-S. Huang, A. Wallraff, S. M. Girvin, and R. J. Schoelkopf, "Cavity quantum electrodynamics for superconducting electrical circuits: An architecture for quantum computation," *Physical Review A*, vol. 69, no. 6, p. 062 320, 2004.

[60] S. Meister, M. Mecklenburg, V. Gramich, J. T. Stockburger, J. Ankerhold, and B. Kubala, "Resonators coupled to voltage-biased josephson junctions: From linear response to strongly driven nonlinear oscillations," *Physical Review B*, vol. 92, no. 17, p. 174 532, 2015.

[61] H. J. Carmichael, *Statistical methods in quantum optics 1: master equations and Fokker-Planck equations*. Springer Science & Business Media, 1999, vol. 1.

[62] H.-P. Breuer, F. Petruccione, *et al.*, *The theory of open quantum systems*. Oxford University Press on Demand, 2002.

[63] C. Gerry, P. Knight, and P. L. Knight, *Introductory quantum optics*. Cambridge University Press, 2005.

[64] M. Westig, B. Kubala, O. Parlavecchio, Y. Mukharsky, C. Altimiras, P. Joyez, D. Vion, P. Roche, D. Esteve, M. Hofheinz, M. Trif, P. Simon, J. Ankerhold, and F. Portier, "Emission of nonclassical radiation by inelastic cooper pair tunneling," *Physical Review Letters*, vol. 119, p. 137 001, 13 Sep. 2017. DOI: `10.1103/PhysRevLett.119.137001`. [Online]. Available: `https://link.aps.org/doi/10.1103/PhysRevLett.119.137001`.

[65] A. D. Armour, B. Kubala, and J. Ankerhold, "Josephson photonics with a two-mode super-conducting circuit," *Physical Review B*, vol. 91, no. 18, p. 184 508, 2015.

[66] Y.-Y. Liu, J. Stehlik, C. Eichler, M. Gullans, J. M. Taylor, and J. Petta, "Semiconductor double quantum dot micromaser," *Science*, vol. 347, no. 6219, pp. 285–287, 2015.

[67] F. Chen, A. Sirois, R. Simmonds, and A. Rimberg, "Introduction of a dc bias into a high-q superconducting microwave cavity," *Applied Physics Letters*, vol. 98, no. 13, p. 132 509, 2011.

[68] S. Jebari, F. Blanchet, A. Grimm, D. Hazra, R. Albert, P. Joyez, D. Vion, D. Esteve, F. Portier, and M. Hofheinz, "Near-quantum-limited amplification from inelastic cooper-pair tunnelling," *Nature Electronics*, vol. 1, no. 4, pp. 223–227, 2018.

[69] K. F. Riley, M. P. Hobson, S. J. Bence, and M. Hobson, *Mathematical methods for physics and engineering: a comprehensive guide*. Cambridge University Press, 2002.

[70] P. Linz, *Analytical and numerical methods for Volterra equations*. SIAM, 1985.

[71] K. Wood, A. D. Armour, and B. Lang, "Josephson photonics with simultaneous resonances," *arXiv preprint arXiv:2106.15243*, 2021.

[72] M. J. Everitt, T. Clark, P. Stiffell, J. Ralph, and C. Harland, "Energy downconversion between classical electromagnetic fields via a quantum mechanical squid ring," *Physical Review B*, vol. 72, no. 9, p. 094 509, 2005.

[73] D. James and J. Jerke, "Effective hamiltonian theory and its applications in quantum information," *Canadian Journal of Physics*, vol. 85, no. 6, pp. 625–632, 2007.

[74] J.-R. Souquet and A. Clerk, "Fock-state stabilization and emission in superconducting circuits using dc-biased josephson junctions," *Physical Review A*, vol. 93, no. 6, p. 060 301, 2016.

[75] H. Wang, M. Blencowe, A. Armour, A. Rimberg, *et al.*, "Quantum dynamics of a josephson junction driven cavity mode system in the presence of voltage bias noise," *Physical Review B*, vol. 96, no. 10, p. 104 503, 2017.

[76] J. R. Johansson, P. D. Nation, and F. Nori, "Qutip: An open-source python framework for the dynamics of open quantum systems," *Computer Physics Communications*, vol. 183, no. 8, pp. 1760–1772, 2012.

[77] A. H. Nayfeh and D. T. Mook, *Nonlinear oscillations*. John Wiley & Sons, 2008.

[78] S. O. Mundhada, A. Grimm, S. Touzard, U. Vool, S. Shankar, M. H. Devoret, and M. Mirrahimi, "Generating higher-order quantum dissipation from lower-order parametric processes," *Quantum Science and Technology*, vol. 2, no. 2, p. 024 005, 2017.

[79] S. O. Mundhada, A. Grimm, J. Venkatraman, Z. K. Minev, S. Touzard, N. E. Frattini, V. V. Sivak, K. Sliwa, P. Reinhold, S. Shankar, *et al.*, "Experimental implementation of a raman-assisted eight-wave mixing process," *Physical Review Applied*, vol. 12, no. 5, p. 054 051, 2019.

[80] A. Clerk, "New directions in mesoscopic physics," *NATO ASI*, vol. 125, p. 325, 2003.

[81] D. F. Walls, "Squeezed states of light," *Nature*, vol. 306, no. 5939, pp. 141–146, 1983.

[82] M. J. Everitt, T. Clark, P. Stiffell, H. Prance, R. Prance, A. Vourdas, and J. Ralph, "Quantum statistics and entanglement of two electromagnetic field modes coupled via a mesoscopic squid ring," *Physical Review B*, vol. 64, no. 18, p. 184 517, 2001.

[83] M. Göppl, A. Fragner, M. Baur, R. Bianchetti, S. Filipp, J. M. Fink, P. J. Leek, G. Puebla, L. Steffen, and A. Wallraff, "Coplanar waveguide resonators for circuit quantum electrodynamics," *Journal of Applied Physics*, vol. 104, no. 11, p. 113 904, 2008.

[84] P. Virtanen, R. Gommers, T. E. Oliphant, M. Haberland, T. Reddy, D. Cournapeau, E. Burovski, P. Peterson, W. Weckesser, J. Bright, S. J. van der Walt, M. Brett, J. Wilson, K. J. Millman, N. Mayorov, A. R. J. Nelson, E. Jones, R. Kern, E. Larson, C. J. Carey, İ. Polat, Y. Feng, E. W. Moore, J. VanderPlas, D. Laxalde, J. Perktold, R. Cimrman, I. Henriksen, E. A. Quintero, C. R. Harris, A. M. Archibald, A. H. Ribeiro, F. Pedregosa, P. van Mulbregt, and SciPy 1.0 Contributors, "Scipy 1.0: Fundamental algorithms for scientific computing in python," *Nature Methods*, vol. 17, pp. 261–272, 2020. DOI: 10.1038/s41592-019-0686-2.

[85] W. H. Press, H. William, S. A. Teukolsky, A. Saul, W. T. Vetterling, and B. P. Flannery, *Numerical recipes 3rd edition: The art of scientific computing*. Cambridge University Press, 2007.

[86] P. Linz, "A method for solving nonlinear volterra integral equations of the second kind," *Mathematics of Computation*, vol. 23, no. 107, pp. 595–599, 1969.

[87] R. Katani and S. Shahmorad, "Block by block method for the systems of nonlinear volterra integral equations," *Applied Mathematical Modelling*, vol. 34, no. 2, pp. 400–406, 2010.

[88] E. Hairer, C. Lubich, and M. Schlichte, "Fast numerical solution of nonlinear volterra convolution equations," *SIAM journal on scientific and statistical computing*, vol. 6, no. 3, pp. 532–541, 1985.